Development of sub-50-fs laser oscillator with mega-watt peak power for nonlinear applications

by

Sujith Chacko Manjooran

A Thesis submitted to the Faculty of Graduate Studies of
The University of Manitoba
in partial fulfillment of the requirements of the degree of

DOCTOR OF PHILOSOPHY

Dept. of Electrical and Computer Engineering,
University of Manitoba
Winnipeg, Canada

Abstract

For several biomedical nonlinear applications mega-watt (MW) peak power lasers working in the near-infrared (NIR) wavelength range are desirable. A cost-effective diode-pumped sub-100-fs solid-state laser oscillator with MW peak power in the NIR wavelength range is not readily available on the commercial market. This thesis presents the successful development of several high power continuous wave (CW) and intense short pulse laser designs. Two laser gain media, namely Yb:$KY(WO_4)_2$ (Yb:KYW) and Yb: $CaGdAlO_4$ (Yb:CALGO), were studied in this thesis. These solid-state laser crystals were end-pumped with high power diode laser at ~980 nm.

Initially, the continuous wave operation of Yb:KYW with 9W of output power at 1045 nm was demonstrated. The developed Yb:KYW had the highest slope efficiency of 77.9% when compared to all other diode-pumped Yb:KYW lasers. At the same time the developed Yb:CALGO laser was capable of delivering tunable multi-watt output power in the wavelength range of approximately 1020 nm to 1070 nm.

Based on these results two intense short pulse lasers were designed and developed in this thesis. The first one was a sub-50-fs Kerr-lens and saturable absorber (KLAS) mode-locked Yb:CALGO laser oscillator with a repetition rate of 42.3 MHz. The highest peak power achieved for 45-fs pulses directly from the oscillator was 1.7 MW. The shortest generated pulses were 38-fs with 187 kW of peak power. The second laser was a sub-100-fs Kerr-lens mode-locked (KLM) Yb:CALGO laser with a low repetition rate of 10.2 MHz. The oscillator produced 650 mW of average output power with pulse duration of 66 fs. It also generated 1 W of average power with pulse duration of 72 fs. This corresponds to pulse energy of 64 nJ with a peak power of 0.97 MW and 98 nJ with the peak power of 1.36 MW, respectively.

Some of the nonlinear applications of the high intense laser pulses were studied in the final section. Phase-matching conditions of three periodically poled crystals (PPKTP, MgO:PPcLN and MgO:PPSLT) for use in femtosecond optical parametric oscillators (OPO) to generate wavelength tunability in the NIR range were studied.

The developed intense short pulse lasers in this project have numerous applications not only in biomedical research but also in fundamental science and industry.

Acknowledgement

First of all, I would like to thank Dr. Arkady Major to give me this wonderful opportunity to pursue my dream career of laser technology in Canada. His solid understanding on the subject and attention-to-details guided me throughout the project. Many thanks to my PhD Committee members Dr. Cyrus Shafai and Dr. Can-Ming Hu for sparing their time to review my progress and for their valuable suggestions for the improvement of this project.

Special thanks to the super-hero student advisor Amy Dario for her generous services. The help and encouragement from my lab-mates and colleagues were invaluable, especially the help from Dr. Haitao Zhao, Dr. Reza Akbari and Dr. Tanant Waritanant.

I would like to thankfully remember the name of my friends, Amu Prakash, Sumitha Koshi, Praveen Johnson, Annet Priya, Sudheesh Sudhakaran and Mita Narayanan who helped in various stages of my student life. Their friendship helped me a lot to keep my spirits high and enjoy the beautiful life in Canada.

All this wouldn't come true without the support of my family. Many thanks to my Father Chacko, Mother Pauly, Sisters Suja and Sunitha and my nieces Seba, Sandra, Mary and Anu, and my brothers Ritesh and Nithin. All my days are filled with hope and laughter by my wonderful kids Jacob and George. Special thanks to my wife's parents Germeena and George and my friends Deepak and Chandini for child minding Jacob and George. Finally, sincere thanks and love to my wife Neethu for her immense patience and support. Please extend my thanks to all my friends and well-wishers who were not mentioned here.

I would like to acknowledge funding of this project provided by the Natural Science and Engineering Research Council of Canada (NSERC), Western Economic Diversification Canada, and the University of Manitoba.

Table of Contents

List of symbols and abbreviations

Symbols

η_{p-p}	*Pump-to-peak power efficiency*
c	*Velocity of light*
D	*Optical power of lens*
dn/dT	*Thermo-optic coefficient*
E_p	*Pulse energy*
k	*Wave number*
M	*Sensitivity factor*
M^2	*Beam quality factor*
n	*Refractive index*
n_2	*Nonlinear refractive index*
P_{abs}	*Absorbed pump power*
P_{avg}	*Average power*
P_p	*Peak power*
P_{PE}	*Photoelastic term*
q	*Quantum defect*
S	*Astigmatism*
α_t	*Thermal expansion coefficient*
δ	*SPM coefficient*
δ_{klm}	*KLM sensitivity*
η_L	*Laser extraction efficiency*
η_{o-o}	*Optical-to-optical efficiency*
η_p	*Pump quantum efficiency*
η_r	*Radiative quantum efficiency*
η_{SL}	*Slope efficiency*
κ	*Thermal conductivity*
λ	*Wavelength*
Λ	*Grating period of periodically poled crystal*
ν	*Frequency*
$\sigma_{em}\,\tau$	*Sigma-Tau product*

τ_p	*Pulse duration*
ϕ_B	*Brewster angle*
χ	*Susceptibility*
ω	*Radius*
ω_p	*Pump radius*

Abbreviations

AC	*Autocorrelator*
AR	*anti-reflection*
BiBO	*Bismuth borate*
BRF	*Birefringent filter*
CARS	*Coherent anti-Stokes Raman scattering*
CW	*Continuous wave*
FOM	*Figure of merit*
FSR	*Free spectral range*
FWHM	*Full width half maximum*
GDD	*Group delay dispersion*
GTI	*Gires-Tournois Interferometer*
GVD	*Group velocity dispersion*
HR mirror	*High reflection mirror*
KLAS	*Kerr-lens and saturable absorber*
KLM	*Kerr-lens mode locking*
LASCAD	*Laser cavity analysis and design*
MDT	*Monoclinic double tungstate*
MgO:PPcLN	*Magnesium oxide-doped periodically poled congruent lithium niobate*
MgO:PPSLT	*Magnesium oxide-doped periodically poled stoichiometric lithium tantalate*
NA	*Numerical aperture*
OC	*Output Coupler*
OPO	*Optical parametric oscillator*
PCF	*Photonic crystal fiber*
PPKTP	*Periodically poled potassium titanyle phosphate*
QPM	*Quasi phase-matching*

SESAM	*Semiconductor saturable absorber mirror*
SHG	*Second harmonic generation*
SPM	*Self-phase modulation*
TBP	*Time-bandwidth product*
TDL	*Thin disk laser*
Ti:sapphire	*Titanium-doped sapphire*
TL	*Thermal lens*
TOC	*Thermo-optic coefficient*
TOD	*Third order dispersion*
TPEF	*Two-photon excited fluorescence*
VNIR	*Visible and near infra-red*
Yb:CALGO	*Ytterbium-doped calcium gadolinium aluminum oxide*
Yb:KYW/KGW	*Yb-doped potassium yttrium tungstate / potassium gadolinium tungstate*

List of tables

List of Figures

Chapter 1: Introduction

1.1 Intense short pulse infrared laser: Review and applications

How short? : The state-of-the-art short pulse lasers are moving from *attosecond* (as) (10^{-18} s) [1, 2] towards *zeptosecond* (zs) (10^{-21} s) pulse duration. At this time frame, it is even possible to monitor the real-time movements of electrons in the orbitals. These extreme short *attosecond* pulses were generated in extreme-ultra-violet or XUV ($\lambda \sim 10$ nm). This means that the laser emission wavelength is one of the limiting factors in determining the shortest pulse duration that can be generated. The time taken for one wavelength cycle at 1000 nm (near-infrared, NIR, light) to pass a particular point in space at the velocity of light (*c*) is approximately 3.3 *femtoseconds* (fs) (10^{-15}s). In other words, an infrared laser working at 1000 nm wavelength theoretically cannot generate an *attosecond* pulse. It is worth to mention that the bandwidth of the gain medium is also a limiting factor for the shortest achievable pulse duration (explained in Chapter 4). There are, however, multiple applications of the NIR *femtosecond* pulses. The focus of this thesis is the development of an intense short-pulse (**sub-50-fs**) NIR laser ($\lambda\sim$ 1045 nm) for nonlinear applications such as nonlinear bio-imaging. The pulse duration of the developed lasers was in the vicinity of the shortest achievable pulses for the given gain medium and not too far from the theoretical limits.

Why NIR? Most of the biomedical imaging applications rely on the visible-near-infrared (VNIR) (650 nm – 1450 nm) region of the spectrum [3]. This wavelength range for bio-imaging has to be read in parallel with the absorption spectrum of water. The major content of biological samples is water and therefore absorption spectrum of water plays an important role in selecting the wavelength suitable for bio-imaging. The absorption of water increases with longer

wavelength. The 'VNIR window' has the lowest absorption in tissues. The imaging systems working in the 'VNIR window' will provide more information by penetrating deep into the tissues. In addition, this wavelength range has lower auto-fluorescence when compared to the UV-visible region (200 nm – 650 nm) of the spectrum. For bio-imaging applications wavelength range of 200 nm – 650 nm is generally not preferred because of the high absorbance by melanin, proteins, and hemoglobin and the high background noise created by auto-fluorescence [4]. The optical window most suitable for imaging tissues is between 1000 -1100 nm [5].

In the visible region, there is no doubt that the Ti:sapphire laser (operates around 800 nm wavelength and the possible tuning range is from 650 nm to 1100 nm) dominates the industry because of its unique laser properties. However, for the NIR region, lasers based on the rare-earth-doped (Nd^{3+} or Yb^{3+}) gain materials are widely used for numerous applications. Moreover, with the help of nonlinear mechanisms like second harmonic generation (SHG) and optical parametric oscillator (OPO), it is possible to extend the wavelength range of Yb/Nd-doped lasers to the visible region as well.

High intensity short pulse lasers are required for applications involving nonlinear processes. The induced polarization (**P**) in any optically transparent material is dependent on the intensity of the applied electric field (**E**). i.e. $\mathbf{P} = \chi\ \mathbf{E}$, where χ is the susceptibility. This relationship forms the basis of nonlinear optics. For nonlinear response from a material, high intensity (*Power/Area*) is required. If the excitation source is a pulsed laser, the power of the pulse can be specified as the peak power (P_p) (*Pulse Energy/Pulse duration*). At the same time, if the repetition rate (*Rep. Rate or No. of pulses/second*) is known, it is possible to calculate the average power (P_{avg}=*Rep. Rate* $\times$ *Pulse energy*) of a pulse train.

How intense? This thesis is about generating highly intense sub-100 fs pulses. 'Intense pulse' is a broad terminology. Intense pulses in the ns and ps regimes are several orders of magnitude higher than the pulses presented in this thesis. For example, the current world record for the highest peak power is 2 *petawatt* (PW) (10^{15}) *(Pulse energy, E_p = 2 kJ and pulse duration, τ_p = 1 ps*) at NIR wavelength (λ = 1053 nm). This result was reported by Institute of Laser Engineering, Osaka University in Japan [6]. However, the world record for the highest pulse energy is 1.8 *megajoule* (MJ) (τ_p *= 20 ns, P_p=90 terawatt (*TW*, 10^{12})*) from the Lawrence Livermore National Laboratory (LLNL) in California [7]. These high power levels are generated by several levels of amplification and pulse compression starting from a low energy pulse generated by a seed laser oscillator. These huge laser systems (laser amplifiers occupy hundreds of square feets of space) are used in experiments for laser fusion energy generation.

This thesis explains the development of powerful laser oscillators with peak power of the order of MW, pulse energy of the order of 100 nJ, and pulse duration of less than 100 fs. No laser amplifiers were used in these experiments. Most of the commercially available sub-100-fs laser oscillators are limited by the peak power (~100 kW) and pulse energy (~10 nJ) required for some of the nonlinear applications and therefore external amplifiers will be needed to increase the pulse energy. This will increase the complexity and price of the laser system many folds. A cost-effective diode-pumped sub-100-fs solid-state laser oscillator with MW peak power is currently not available on the commercial market.

Applications: The major applications of such intense sub-100-fs lasers oscillators are precise micromachining with minimal heat affected zone (HAZ) (Fig. 1-1) [8], nonlinear microscopy (two photon excited fluorescence, (TPEF), Coherent anti-Stokes Raman scattering (CARS), etc.) [9], supercontinuum generation [10], frequency comb generation [11], high harmonic generation

[12], etc. One of the applications of low-repetition rate intense short pulse lasers is fluorescent life time imaging (FLIM) of biological samples [13]. In this thesis, preliminary experiments were conducted on a few other applications, namely second harmonic generation (SHG, section 5.4), Raman spectroscopy (section 5.6) and spectral broadening using photonic crystal fiber (section 5.5). A detailed theoretical study on green-pumped OPO can be found in section 5.3.

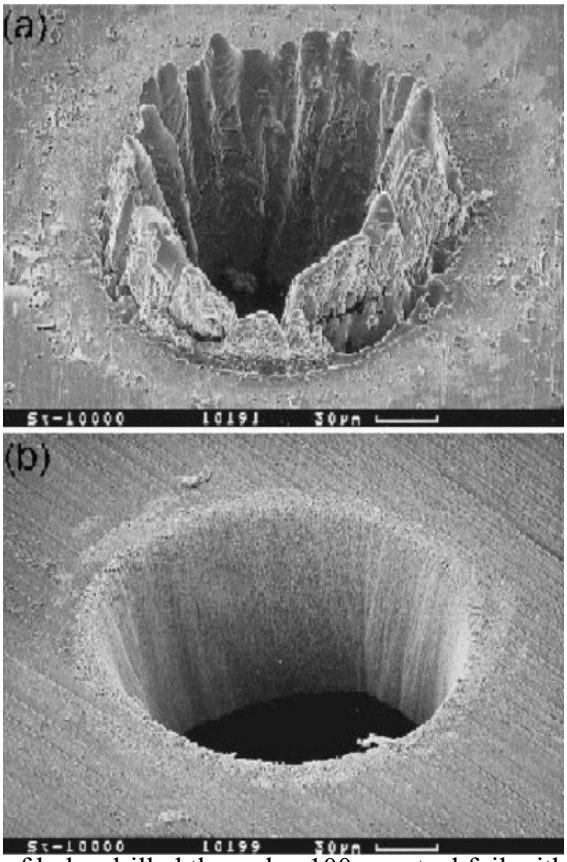

Fig. 1-1 : SEM photographs of holes drilled through a 100 μm steel foil with (a) a pulse duration of τ_p = 3.3 ns and (b) τ_p = 200 fs using Ti:sapphire laser pulses at 780 nm [8] .

1.2 Limitations of the current work-horse - Ti:sapphire laser

The gain bandwidth of a Ti:sapphire laser crystal is ~ 450 nm (from 650 nm to 1100 nm) and is the highest among any solid-state lasers. The thermal conductivity of a Ti: Sapphire is also very high at 33 W/m/K [14]. The shortest pulse duration achievable from a Ti:sapphire laser oscillator is ~ 5 fs [15, 16]. These properties make Ti:sapphire the favourite choice for intense

short pulse applications. However, the main drawback of Ti:sapphire is the large wavelength difference between the peak emission wavelength (at ~ 790 nm) and peak absorption wavelength (at ~ 490 nm). This reduces the efficiency of the laser and the difference in energy is wasted in the form of heat. This effect is called quantum defect. Another major issue is the availability of pump sources around 500 nm. To generate multi-watt output power from a Ti:sapphire laser, the most common pump source is a frequency-doubled Nd/Yb-doped solid-state or fiber laser. This increases the cost of pump source many fold compared to direct diode pumping. Another option in this scenario is direct diode pumping using an indium gallium nitride (InGaN) (λ = 445 nm) diode laser. However, the highest reported output power so far from such a laser was less than 100 mW [17]. The commercially successful Ti:sapphire laser oscillator (Tsunami) from Spectra Physics has a peak power of only 350 kW (τ_p < 100 fs) and pulse energy of less than 35 nJ. For many nonlinear applications of lasers, such as micromachining, the peak power and pulse energy are not high enough.

1.3 **The new era of Yb-doped lasers.**

This thesis deals with Ytterbium ion (Yb^{3+}) gain media. These media are attractive for power-scalable and highly efficient lasers operating around 1 μm. In the context of Yb^{3+}-doped crystals, two host families are of particular interest because of their broad gain bandwidth. They are monoclinic double tungstates (MDTs) and tetragonal rare-earth calcium aluminates. Potassium Yttrium Tungstate (KYW) is an example of MDT and Calcium Gadolinium Aluminate (CALGO) is an example of tetragonal rare-earth calcium aluminate (more details in Chapter 2).

KYW and CALGO crystals have gained considerable attention during the past decade because these crystals can be used to make high power, high repetition rate femtosecond diode-pumped solid-state (DPSS) lasers. These gain media have many advantages over other gain materials

such as high efficiency and broad gain bandwidth. Prior to explaining the reason for high efficiency, it is important to introduce the concepts of quasi-three level system and quantum defect.

Quasi-three level system: Yb:KYW/Yb:CALGO are quasi-three-level lasers. In a basic three-level system, the lower laser level is the ground state itself. This means that the laser transitions end on the ground state. In a four-level laser system the lower laser level is well above the ground state, therefore no appreciable population density in the lower laser level can occur during laser operation. In a quasi-three-level system, the lower laser level is close to the ground state and has some initial population in thermal equilibrium. In most of the Yb-doped lasers, the laser action happens between the electronic levels namely $^2F_{5/2}$ (upper laser level) and $^2F_{7/2}$ (lower laser level) independent of the host material. However, the upper level and the lower level split into several sublevels due to crystal fields (Stark) splitting. These energy-levels are called Stark levels and the bandwidth of the emission spectrum largely depends on the host material. There are four sublevels for the $^2F_{7/2}$ level and three sublevels for the $^2F_{5/2}$ level due to Stark splitting. The energy difference between the lower laser level and the ground state is relatively small for quasi-three level lasers. The only drawback of a quasi-three-level laser is the reabsorption loss at the laser emission wavelength (~ 1040 nm) because of the initial thermal population of the lower laser level. As a result, the emission and absorption spectra of the quasi-three-level laser gain media overlap.

Low quantum defect: In most lasers the energy of the laser photon is smaller than the energy of the pump photons. The photon energy difference is called the quantum defect, denoted by q, and an example calculation of fractional quantum defect is shown in 1.1.

$$q = \left(1 - \frac{\lambda_{pump}}{\lambda_{Laser}}\right) \times 100\% = \left(1 - \frac{980\ nm}{1040\ nm}\right) = 5.8\ \% \quad 1.1$$

Quantum defect and nonradiative relaxations from the pump band to the ground state will generate heat in the host lattice and lead to detrimental thermal effects, for example thermal lensing. In the case of diode-pumped Yb:KYW and Yb:CALGO lasers the standard pumping wavelength is around 980 nm and the laser emission wavelength is around 1040 nm. This means that the difference in energy or the quantum defect is much lower when compared to other solid-state lasers (e.g. Nd:YAG) that are pumped at 808 nm and operate around 1060 nm.

High efficiency: Both Yb-ion crystals mentioned above have high optical-to-optical efficiency and high slope efficiency. In simple words, slope efficiency is obtained by plotting the laser output power against the input pump power. An extremely low quantum defect between the absorption and emission wavelengths leads to high laser slope efficiencies for these lasers. The slope efficiency (η_{slope}) can be evaluated using the equation 1.2

$$\eta_{slope} = \frac{T}{T + L}\left(\frac{\lambda_{pump}}{\lambda_{laser}}\right) \quad 1.2$$

where T is the output coupler transmittance and L is the total "parasitic" loss generated by the mirrors in the resonator.

Broad gain bandwidth: Yb:KYW has a gain bandwidth of ~ 25 nm and Yb:CALGO has a gain bandwidth of ~ 80 nm. Both of these crystals are capable of generating sub-50-fs laser pulses.

Efficient diode pumping at ~ 980 nm: Diode lasers are a compact, efficient and cost effective way of pumping solid-state lasers. The choice of diode lasers is limited by their emission wavelengths. The emission wavelength of the diode laser should match the absorption band of a given solid-state laser. The InGaAs laser diodes in the 930-980 nm range are a suitable choice for pumping of the Yb:KYW and Yb:CALGO gain media.

1.4 **Background and Literature Review**

Yb:KYW : In 1996, the first continuous wave (CW) Yb:KYW laser was demonstrated by N. V. Kuleshov *et al*. [18, 19]. This was a joint research project between the International Laser Center, Belarus and the Institute für Laser-Physik, Germany. The output wavelength was 1025 nm. This was demonstrated using a Ti:sapphire laser and InGaAs diode laser pump sources as reported in 'Conference on Lasers and Electro-Optics Europe, 96'. In 1997, the same research group reported the first pulsed laser operation using these crystals. A gain-switched Ti:sapphire laser with 30 ns pulse duration was used as the pump source [20]. The first pulsed laser operation using these crystals reported a slope efficiency as high as 86.9% [20]. The mode-locked pulses were generated using Yb:KGW/KYW bulk lasers in 1997. In 2002, A. S. Grabtchikov *et al.* [21] presented a diode-pumped Yb:KYW microchip laser operating both in CW and in passively Q-switched regimes. In passive Q-switching a pulse width of 1 ns was achieved at a repetition rate of 49 kHz. The average power was about 26 mW. The first mode-locked Yb:KGW developed by F. Brunner *et al.* [22] in 2000, generated pulses of 176 fs with an average output power of 1.1 W. In 2002, F. Brunner *et al.* [23] presented a passively mode-locked thin disk Yb:KYW laser. The laser produced pulses of 240 fs duration with an average power of 22 W at a center wavelength of 1028 nm.

Yb:CALGO: This laser gain medium was first introduced by J. Petit *et al.* in 2005 [24]. The shortest pulses achieved to date using the Yb:CALGO are 32 fs [25]. A. Greborio *et al.* [26] managed to generate 94 fs pulses with MW peak power using Yb:CALGO crystal and 60 W of pump power. These were the first sub-100-fs pulse with MW peak power produced directly from the oscillator.

1.5 Advantage of bulk laser geometry

To help the understanding of the importance of this work in the current scenario, state-of-the-art laser oscillators are reviewed here. However, the amplifiers combined with external pulse compression can deliver much higher pulse energy than the oscillators studied here. In the current market, four kinds of laser oscillators are mainly competing with each other to dominate the laser industry, namely, bulk crystal lasers, thin disk lasers (TDL), fiber lasers and semiconductor lasers.

For short pulse generation (< 100 fs) passive mode locking (ML) techniques need to be employed. The available options are Kerr-lens mode locking (KLM), semiconductor saturable absorber mirror (SESAM) mode locking and a combination of both (detailed study in Chapter 4).

Fiber lasers: Fiber lasers have the advantage of ease of use and integration. They require low maintenance, are highly versatile and compact. A large number of diode-stack modules can be used in parallel for pumping [27] and in continuous wave regime, up to 10 kW can be achieved using single mode fiber and 100 kW can be achieved using multi-mode fiber [28]. Yb-doped fiber lasers were used to attain short pulses [29] and extremely high intensity using chirped pulse amplification (CPA) [30]. The major drawbacks of short pulse fiber lasers include poor beam shape and high nonlinear effects. The fiber-tip damage can result from high peak intensity of the pulses.

Diode lasers: Diode lasers are the most cost-effective laser available on the market. They can be easily integrated to electronics and consumer products. They do not require optical pumping and therefore they can be considered as comparatively efficient. However, the diode lasers are incapable of generating ultrashort pulses with high peak power.

Thin Disk Lasers (TDL): The TDL oscillators are the first choice for power scaling because the thin disk geometry facilitates better heat removal. This is usually explained in terms of volume density. They can produce 100's of W of average power and MW's of peak power. The pulse energy can go as high as 80 μJ [31]. In TDL the gain medium does not have enough thickness to absorb all the pump power in one pass. Therefore, several passes or reflections are required to absorb the entire pump power and this is generally known as recycling of pump. The recycling of pump that is needed in TDLs is one of their major disadvantages. This multiple-pass pump geometry due to low pump absorption in thin (~200 μm) laser crystals increases the engineering complexity [31].

Another main drawback of TDL lasers is the difficulty associated with generation of short pulses. The thickness of the thin disk gain medium is of the order of few hundred micrometers. It is not long enough to generate any significant nonlinear Kerr effect. Therefore to achieve KLM, an additional intracavity nonlinear crystal (or stack of crystals) has to be employed [32]. The first TDL was developed using an Yb:YAG gain medium [33]. Even now, Yb:YAG dominates amongst the high intensity short pulse TDLs with an average output power of 275 W and pulse energy of 16.9 μJ for a pulse duration of 583 fs [34]. The high pulse energy was achieved by stretching the cavity length to over 9 m. A similar approach was used in this thesis to extract higher pulse energy from the oscillator (see chapter 4). TDLs were already reported for the two crystals that were used in this thesis.

One important result on Yb:KYW TDL was reported by F. Brunner *et al.* [23] in 2002. They reported 240 fs with an average power of 22 W and a peak power of 3.3 MW. A short pulse of 62 fs was reported for Yb:CALGO TDL by A. Diebold *et al.* [35] in 2013. The output peak power was 1.1 MW and the average output power was 5.1 W. Both these papers used SESAM

mode locking technique (see chapter 4) to generate short pulses. The complex pump recycling geometry and the engineering challenges associated with it make it highly expensive to build such a laser.

Advantages of bulk laser geometry

The most important advantages of bulk lasers are their simple design and ability to generate ultrashort pulses using passive mode locking techniques (especially Kerr lens modelocking). In most of the cases, the bulk lasers can generate ultrashort pulses with excellent beam quality. These properties make bulk lasers especially useful in nonlinear applications.

1.6 **Motivation**

To find a laser with short pulse duration (< 100 fs) and multi-watt average output power, the options are very limited and also highly expensive. The motivation of this thesis is to contribute to this technically-challenging regime by developing a high power, short-pulse, good beam quality laser based on simple and inexpensive bulk crystal design using diode pumping.

Traditionally, Ti:Sapphire lasers dominated this regime with its exceptionally good qualities of high thermal tolerance, wide wavelength tunability and short pulse duration. Recently, other competitors like fiber lasers, thin disk lasers and bulk lasers with new laser materials are challenging the predominance of Ti: Sapphire lasers in this regime.

Yb-doped bulk lasers are selected here because of their outstanding efficiency, optical bandwidth and the availability of diode pump sources. The tested laser crystals of Yb:KYW and Yb:CALGO have several advantages over other gain media. It is worth to mention that the availability of high quality pump diodes was a major challenge in this project. Apart from that other challenges like thermal management, detrimental thermal effects and occasional dual wavelength operations were dealt in this project. As a result the study was extended to these

areas as well. These challenges paved the way for very interesting secondary results. The thermal lens study conducted on Yb:KYW will be a valuable asset for future experiments using this crystal. Additionally, the multi-watt dual-wavelength operation of Yb:CALGO is definitely a tool looking for applications in THz imaging.

The primary aim was to develop a DPSS multi-watt short-pulse laser and study its possible nonlinear optical applications. The important nonlinear applications under consideration were second harmonic generation, optical parametric oscillations and supercontinuum generation. The developed lasers in this project can be considered as tools and it is expected that these tools will assist numerous applications not only in biomedical research but also in fundamental science and industry.

1.7 **Novelty and thesis contributions**

The major contributions of this thesis are:

- The efficiency of bulk Yb:KYW laser achieved in this thesis are the highest ever achieved for this laser crystal.
- A detailed study of the thermal properties of Yb:KYW was conducted. The inferences drawn from these studies with the help of collaborators were unique in many aspects. For example, the dependence of thermal lensing effect on light polarization was carefully studied. The conclusions from these studies will help to choose the optimum geometry to reduce the spatial distortions of the laser beam.
- When a birefringent plate was introduced into a laser cavity, the possibility of light amplification at more than one discrete wavelength was predicted long before. In this thesis, the experimental demonstration of this effect was studied with different birefringent plates of various thicknesses. This was demonstrated for the first time for Yb:CALGO crystal with a

multi-watt output power. The dual-wavelength operation was possible mainly because of the wide wavelength tunabilty of Yb:CALGO. In addition, control over the wavelength separation and the multi-watt output powers were obtained.

- For short-pulse generation two mode locking mechanisms were deployed. The first one was a combination of SESAM and KLM and the second one was pure KLM. The outstanding feature of these experiments was to utilize the Kerr effect for mode locking while gain medium is diode-pumped. This was a highly challenging regime, and only a few works were successful in achieving KLM while diode pumping. The highlight of this project was that a bulk sub-50 fs laser was developed for the first time with more than 1 MW of peak power.
- In the final part of the thesis, theoretical studies of optical parametric oscillation in the visible and near-infrared ranges with green pump were carried out. The optical and dispersive characteristics of three nonlinear crystals, namely, PPKTP, MgO:PPcLN and MgO:PPSLT, were analyzed for the first time. The significance of this work is that these nonlinear crystals are well suited for the planned implementation of green-pumped (520 nm) OPO in the future. The theoretical studies conducted based on phase-matching condition showed that the wavelength tuning range of such an OPO will be from 600 nm to 2000 nm. A wide tuning range is highly desirable for biomedical and spectroscopic applications.

1.8 Organization of the thesis and related publications

This thesis goes through a variety of topics starting from CW laser design, Yb-doped materials, Kerr-lens ML, and through various applications of short pulses including supercontinuum and OPO. Fig. 1-2 shows the schematic of thesis structure. A brief summary of relevant works on specific topics that are mentioned in each chapter are listed below.

In chapter 2, data regarding the optical and thermal properties of Yb:KYW and Yb:CALGO crystals were presented. The characteristics of the diode laser used for pumping were also presented. After collecting and analyzing all the data regarding the crystals and the diode pump, a CW laser resonator was designed and implemented. The properties of the developed CW lasers were measured and discussed. A detailed thermal analysis of Yb:KYW crystal was presented at the end of chapter 2. Issues in thermal management resulted in Yb:KYW crystal damage. The remaining part of the project was continued using Yb:CALGO crystal.

Chapter 2 was based on two publications:

1. S. Manjooran and A. Major, "Efficient operation of a diode-pumped multi-watt continuous wave Yb:KYW laser with excellent beam quality," *Laser Physics Letters,* vol. 14, p. 035805, 2017.
2. P. Loiko, S. Manjooran, K. Yumashev, and A. Major, "Polarization anisotropy of thermal lens in Yb:$KY(WO_4)_2$ laser crystal under high-power diode pumping," *Applied Optics,* vol. 56, pp. 2937-2945, 2017.

Chapter 3 was based on simulation and development of a dual-wavelength operation of Yb:CALGO laser. Discrete dual-wavelengths were generated by introducing a birefringent filter plate into the laser cavity. The dependence of discrete dual-wavelength separation on the inserted birefringent filter plate thickness is explained in the chapter.

Chapter 3 was based on the following publication:

1. S. Manjooran, P. Loiko, and A. Major, "A discretely tunable dual-wavelength multi-watt Yb:CALGO laser," *Applied Physics B,* vol. 124, p. 13, 2018.

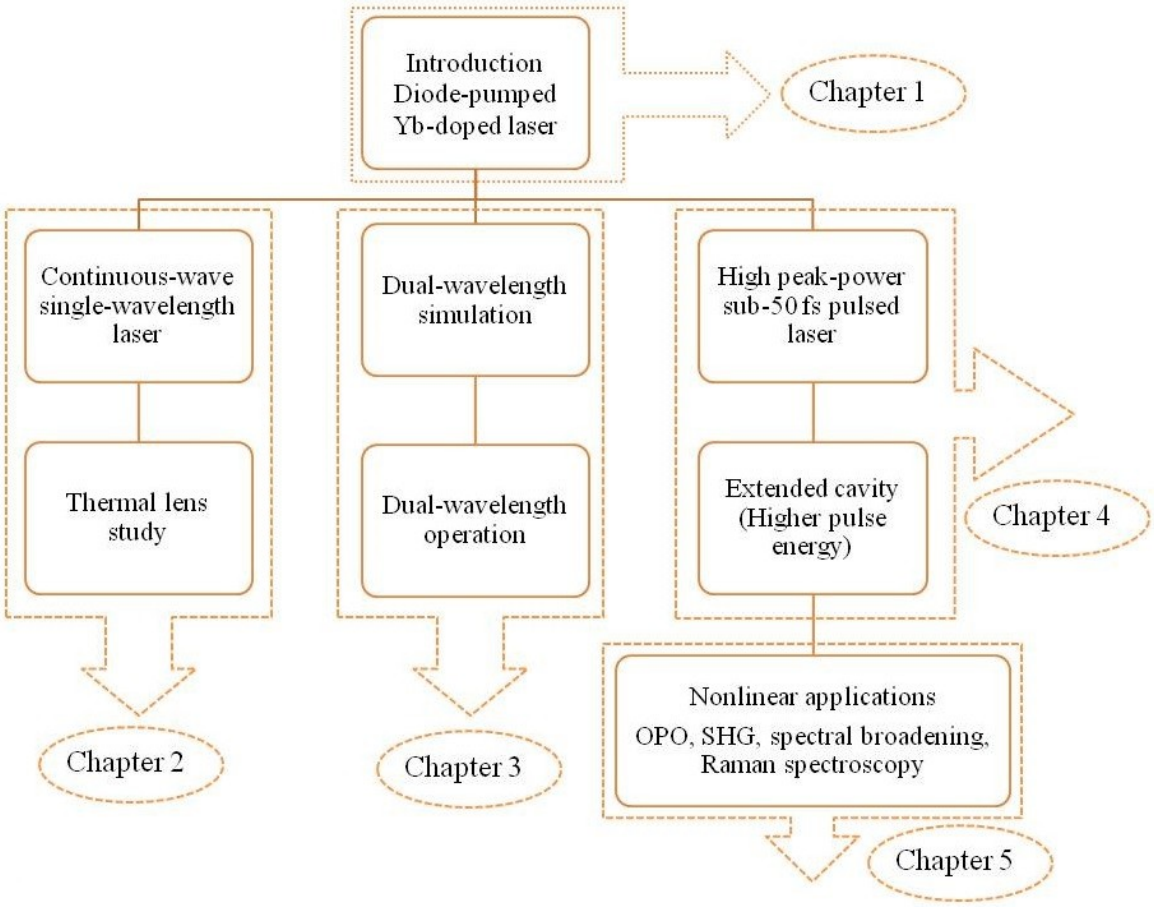

Fig. 1-2. Schematic diagram of thesis organization.

Chapter 4 makes the core part of this thesis. It explains the development of two intense ultrashort pulse lasers. The design and implementation of these two MW peak power lasers with sub-100 fs pulse duration, based on two slightly different technologies, were presented in the chapter. The characteristics of the developed lasers were measured and comparative studies with relevant works were presented.

Chapter 4 was based on two publications:

1. S. Manjooran; and A. Major, "Diode-Pumped 45 fs Yb:CALGO Laser Oscillator With 1.7 MW of Peak Power," *Optics Letters,* vol. 43, p. 2324, 2018.

2. S. Manjooran and A. Major, "Low repetition rate operation of a femtosecond Yb:CALGO laser, *Solid State Lasers XXVII: Technology and Devices, Proc. of SPIE,* vol. 10511, p. 105117, 2018.

Chapter 5 deals with some of the applications of intense ultrashort pulse lasers. A detailed theoretical study on green pumped (frequency-doubled Yb:CALGO) optical parametric oscillator was presented. The capability of the developed high peak power sub-100 fs laser was demonstrated with the help of several proof-of-principle experiments such as second harmonic generation, spectral broadening using photonics crystal fiber and Raman conversion.

Chapter 5 was based on the following publication:

1. S. Manjooran, H. Zhao, I. T. Lima, Jr., and A. Major, "Phase-matching properties of PPKTP, MgO:PPSLT and MgO:PPcLN for ultrafast optical parametric oscillation in the visible and near-infrared ranges with green pump," *Laser Physics,* vol. 22, pp. 1325-1330, 2012.

1.9 References

[1] S. Koke, C. Grebing, H. Frei, A. Anderson, A. Assion, and G. Steinmeyer, "Direct frequency comb synthesis with arbitrary offset and shot-noise-limited phase noise," *Nat Photon,* vol. 4, pp. 462-465, 2010.

[2] K. Zhao, Q. Zhang, M. Chini, Y. Wu, X. Wang, and Z. Chang, "Tailoring a 67 attosecond pulse through advantageous phase-mismatch," *Optics Letters,* vol. 37, pp. 3891-3893, 2012.

[3] V. J. Pansare, S. Hejazi, W. J. Faenza, and R. K. Prud'homme, "Review of Long-Wavelength Optical and NIR Imaging Materials: Contrast Agents, Fluorophores, and Multifunctional Nano Carriers," *Chemistry of Materials,* vol. 24, pp. 812-827, 2012.

[4] M. Monici, "Cell and tissue autofluorescence research and diagnostic applications," *Biotechnology Annual Review,* vol. 11, pp. 227-256, 2005.

[5] Y.-Y. Huang, A. C.-H. Chen, and M. Hamblin, "Low-level laser therapy: an emerging clinical paradigm," *SPIE Newsroom,* vol. 9, pp. 1-3, 2009.

[6] N. M. J. Kawanaka, S. Matsuo, K. Kawabata, Y. Kawakami, Y. Fujimura, K. Sawai, K., Y. S. Tsuji, Y. Matsuda, T. Kawasaki, H. Murakami, M. Ishida, H. Kitamura, H., T. S. Matsuo, T. Sezaki, T. Yanagida, S. Tokita, Y. Nakada, K. Tsubakimoto, H., and T. J. Shiraga, and N. Miyanaga, "LFEX-Laser: A Multi-Kilojoule, Multi-Petawatt Heating

Laser for Fast Ignition," in *26th IAEA Fusion Energy Conference*, Kyoto, Japan, 2016, pp. IFE/1-6.

[7] D. Clery, "Laser Fusion Energy Poised to Ignite," *Science,* vol. 328, pp. 808-809, 2010.

[8] C. Momma, S. Nolte, B. N. Chichkov, F. v. Alvensleben, and A. Tünnermann, "Precise laser ablation with ultrashort pulses," *Applied Surface Science,* vol. 109, pp. 15-19, 1997.

[9] V.-H. Le, S. W. Yoo, Y. Yoon, T. Wang, B. Kim, S. Lee*, et al.*, "Brain tumor delineation enhanced by moxifloxacin-based two-photon/CARS combined microscopy," *Biomedical Optics Express,* vol. 8, pp. 2148-2161, 2017.

[10] G. Genty and J. M. Dudley, "Supercontinuum, solitons, and instabilities," in *SPIE Newsroom*, ed, 2015.

[11] A. Schliesser, N. Picque, and T. W. Hansch, "Mid-infrared frequency combs," *Nat Photon,* vol. 6, pp. 440-449, 2012.

[12] H. J. Wörner, J. B. Bertrand, B. Fabre, J. Higuet, H. Ruf, A. Dubrouil*, et al.*, "Conical Intersection Dynamics in NO_2 Probed by Homodyne High-Harmonic Spectroscopy," *Science,* vol. 334, p. 208, 2011.

[13] A. Major, V. Barzda, P. A. E. Piunno, S. Musikhin, and U. J. Krull, "An extended cavity diode-pumped femtosecond Yb:KGW laser for applications in optical DNA sensor technology based on fluorescence lifetime measurements," *Opt. Express,* vol. 14, pp. 5285-5294, 2006.

[14] P. F. Moulton, "Spectroscopic and laser characteristics of Ti:Al_2O_3," *Journal of the Optical Society of America B,* vol. 3, pp. 125-133, 1986.

[15] D. H. Sutter, G. Steinmeyer, L. Gallmann, N. Matuschek, F. Morier-Genoud, U. Keller*, et al.*, "Semiconductor saturable-absorber mirror–assisted Kerr-lens mode-locked Ti:sapphire laser producing pulses in the two-cycle regime," *Optics Letters,* vol. 24, pp. 631-633, 1999.

[16] U. Morgner, F. X. Kärtner, S. H. Cho, Y. Chen, H. A. Haus, J. G. Fujimoto*, et al.*, "Sub-two-cycle pulses from a Kerr-lens mode-locked Ti:sapphire laser," *Optics Letters,* vol. 24, pp. 411-413, 1999.

[17] C. G. Durfee, T. Storz, J. Garlick, S. Hill, J. A. Squier, M. Kirchner*, et al.*, "Direct diode-pumped Kerr-lens mode-locked Ti:sapphire laser," *Optics Express,* vol. 20, pp. 13677-13683, 2012.

[18] N. V. Kuleshov, A. A. Lagatsky, V. G. Shcherbitsky, V. P. Mikhailov, E. Heumann, T. Jensen*, et al.*, "CW Laser Performance of Yb doped $KY(W0_4)_2$ and $KGd(WO_4)_2$," presented at the Conf. on Lasers and Electro-Optics Europe 96, New York, 1996.

[19] N. V. Kuleshov, A. A. Lagatsky, V. G. Shcherbitsky, V. P. Mikhailov, E. Heumann, T. Jensen*, et al.*, "CW laser performance of Yb and Er,Yb doped tungstates," *Applied Physics B,* vol. 64, p. 5, 1997.

[20] N. V. Kuleshov, A. A. Lagatsky, A. V. Podlipensky, V. P. Mikhailov, and G. Huber, "Pulsed laser operation of Yb-doped $KY(WO_4)_2$ and $KGd(WO_4)_2$," *Optics Letters,* vol. 22, p. 3, 1997.

[21] A.S. Grabtchikov, A. N. Kuzminb, V.A. Lisinetskii, V.A. Orlovic, A.A. Demidovich, M.B. Danailovc*, et al.*, "Laser operation and Raman self-frequency conversion in Yb:KYW microchip laser," *Applied Physics B,* vol. 75, p. 3, 2002.

[22] F. Brunner, G. J. Spühler, J. Aus der Au, L. Krainer, F. Morier-Genoud, and R. Paschotta, "Diode-pumped femtosecond Yb:$KGd(WO_4)_2$ laser with 1.1-W average power," *Optics Letters,* vol. 25, p. 3, 2000.

[23] F. Brunner, N. V. Kuleshov, and U. Keller, "240-fs pulses with 22-W average power from a mode-locked thin-disk Yb:$KY(WO_4)_2$ laser," *Optics Letters,* vol. 27, p. 3, 2002.

[24] J. Petit, P. Goldner, and B. Viana, "Laser emission with low quantum defect in Yb:CaGdAlO4," *Optics Letters,* vol. 30, pp. 1345-1347, 2005.

[25] P. Sévillano, P. Georges, F. Druon, D. Descamps, and E. Cormier, "32-fs Kerr-lens mode-locked Yb:$CaGdAlO_4$ oscillator optically pumped by a bright fiber laser," *Optics Letters,* vol. 39, pp. 6001-6004, 2014.

[26] A. Greborio, A. Guandalini, and J. Aus der Au, "Sub-100 fs pulses with 12.5-W from Yb:CALGO based oscillators," *Proc. SPIE,* vol. 8235, pp. 823511-1, 2012.

[27] Y. Xiao, F. Brunet, M. Kanskar, M. Faucher, A. Wetter, and N. Holehouse, "1-kilowatt CW all-fiber laser oscillator pumped with wavelength-beam-combined diode stacks," *Optics Express,* vol. 20, pp. 3296-3301, 2012.

[28] V. Fomin, V. Gapontsev, E. Shcherbakov, A. Abramov, A. Ferin, and D. Mochalov, "100 kW CW fiber laser for industrial applications," in *2014 International Conference Laser Optics*, 2014, pp. 1-1.

[29] F. Ö. Ilday, J. Buckley, L. Kuznetsova, and F. W. Wise, "Generation of 36-femtosecond pulses from a ytterbium fiber laser," *Optics Express,* vol. 11, pp. 3550-3554, 2003.

[30] J. Rothhardt, S. Demmler, S. Hädrich, J. Limpert, and A. Tünnermann, "Octave-spanning OPCPA system delivering CEP-stable few-cycle pulses and 22 W of average power at 1 MHz repetition rate," *Optics Express,* vol. 20, pp. 10870-10878, 2012.

[31] C. J. Saraceno, F. Emaury, C. Schriber, M. Hoffmann, M. Golling, T. Südmeyer*, et al.*, "Ultrafast thin-disk laser with 80μJ pulse energy and 242 W of average power," *Optics Letters,* vol. 39, pp. 9-12, 2014.

[32] O. Pronin, J. Brons, C. Grasse, V. Pervak, G. Boehm, M. C. Amann*, et al.*, "High-power 200 fs Kerr-lens mode-locked Yb:YAG thin-disk oscillator," *Optics Letters,* vol. 36, pp. 4746-4748, 2011.

[33] A. Giesen, H. Hügel, A. Voss, K. Wittig, U. Brauch, and H. Opower, "Scalable concept for diode-pumped high-power solid-state lasers," *Applied Physics B,* vol. 58, pp. 365-372, 1994.

[34] C. J. Saraceno, F. Emaury, O. H. Heckl, C. R. E. Baer, M. Hoffmann, C. Schriber*, et al.*, "275 W average output power from a femtosecond thin disk oscillator operated in a vacuum environment," *Optics Express,* vol. 20, pp. 23535-23541, 2012.

[35] A. Diebold, F. Emaury, C. Schriber, M. Golling, C. J. Saraceno, T. Südmeyer*, et al.*, "SESAM mode-locked Yb:$CaGdAlO_4$ thin disk laser with 62 fs pulse generation," *Opt. Lett.,* vol. 38, pp. 3842-3845, 2013.

Chapter 2: Continuous Wave Laser Design and Thermal Effects

2.1 Introduction and preview

One of the initial requirements of laser development is to study the absorption and emission properties of the gain medium. The knowledge regarding emission bandwidth will help to determine the reflection/transmission range of the optics to be used and the absorption spectrum helps to select the pump wavelength to be used. The pump laser characterization is an integral part of the laser design because it provides information regarding the pump spot size, central wavelength dependence on temperature and overlap with the laser beam inside the gain medium.

The objective of this chapter was to develop CW lasers based on Yb:KYW and Yb:CALGO crystals and measure their average output power, beam quality and thermal lensing. This chapter will present the increase in output power with respect to the pump power, beam quality and thermal lens measurements. All this information is required for the final goal of development of an intense ultrashort pulse laser.

In general Yb^{3+}-doped crystals are free from several detrimental processes like excited state absorption, cross-relaxation and upconversion which are seen in other solid-state lasers. This results in high efficiency, low laser threshold, broad tuning of laser emission and generation of ultrashort pulses in mode-locked lasers [1]. High Yb^{3+} doping levels are also possible for these laser crystals.

Diode-pumped bulk lasers are cost-effective and efficient tools for various applications in research and industry. The advantages of diode pumping and the specifications of the high power pump laser (~ 980 nm) used in the experiments will be explained in section 2.3.1. Thermal

management and thermal effects studies constitute an integral part of the laser design. These are briefly explained in sections 2.5 and 2.6. The CW results for Yb:CALGO and Yb:KYW lasers were obtained from very similar laser designs. The Gaussian profile of the CW laser beams were studied in the beam quality analysis. The CW results were compared with other prominent results in section 2.5.

2.2 Yb:KYW and Yb:CALGO crystal properties

The spectral and laser properties of the Yb^{3+}-doped gain media strongly depend on the host material. As mentioned in Chapter 1, the Stark-splitting caused by the host material determine the bandwidth of the gain medium. Yb^{3+}-doped $CaGdAlO_4$ (CALGO) crystal is a good candidate for high peak power ultrashort laser pulse generation because of its broad gain bandwidth (~80 nm) and high thermal conductivity (6.9 $Wm^{-1}K^{-1}$). Yb:KYW crystal is another popular gain medium that was first introduced on the market and has lower thermal conductivity and more narrow emission bandwidth.

2.2.1 Crystal properties

In Yb:KYW, the rare-earth (Yb^{3+}) ions are introduced into the $KY(WO_4)_2$ host material. The host materials with functional group $(WO_4)_2$ are commonly called double tungstates. Yb:KYW is a member of the crystal family of monoclinic double tungstates (MDTs) having a chemical formula $KRE(WO_4)_2$ where Rare-Earth (RE) can be Gadolinium (Gd), Yttrium (Y) or Lutetium (Lu). They are shortly known as KREW and members of Yb^{3+}:KREW family are Yb:KYW, Yb:KGW and Yb:KLuW [1]. For KYW host material a high level of doping is possible [2]. The monoclinic crystal structure results in a natural birefringence. Yb:KYW is highly anisotropic due to its large crystal anisotropy with three principal mutually orthogonal dielectric axes, N_m, N_g and N_p, which have refractive indices of n_m, n_g and n_p respectively. For an N_g-cut crystal (i.e.

where laser radiation propagates along the N_g-axis) the two possible principle light polarizations are denoted as E || N_m and E || N_p.

Yb:CALGO is a member of the tetragonal rare-earth calcium aluminate crystal family with a chemical formula Ca*Ln*AlO_4, where *Ln* = Gd or Y. Examples are Yb^{3+}:$CaGdAlO_4$ (shortly CALGO) and Yb^{3+}:$CaYAlO_4$ (shortly CALYO). In Yb:CALGO the optic axis is parallel to the crystallographic ***c***-axis. Thus, there are two principal refractive indices, n_o and n_e, and two principal polarizations, $E \parallel c$ (π) and $E \perp c$ (σ) [3]. In the process of doping CALGO crystal with Yb^{3+}-ions, they can replace either Calcium (Ca^{2+}) or Gadolinium (Gd^{3+}) ions. Both Ca^{2+} and Gd^{3+} occupy similar site in the crystallographic structure. It is more likely to substitute Gd^{3+}-ions because of the same valence number of electrons (i.e. 3+). This inhomogeneous substitution leads to large inhomogeneous broadening in the emission spectrum [4].

In general, this kind of disordered structure will reduce the thermal conductivity. However, for Yb:CALGO, the thermal conductivity is still very high. This makes Yb:CALGO an attractive laser gain medium with broad bandwidth and high thermal conductivity.

Table 2-1 : Optical and thermal properties of studied Yb:KYW and Yb:CALGO crystals

Properties	**Yb:KYW**	**Yb:CALGO**
Manufacturer	*Altechna*	*Castech*
Crystal length	*3 mm*	*5 mm*
Crystal structure	*monoclinic*	*tetragonal* [5]
Doping concentration	*5-at. %*	*2-at. %*
Birefringence	*biaxial*	*uniaxial*
Crystal-cut	*N_g-cut*	*a-cut*
Refractive index	*KYW at λ=1045 nm* n_p*=1.969,* n_m*=2.007,* n_g*=2.05* [6]	*CALGO at λ=1045 nm* n_a *= 1.916* n_c*=1.94* [7]
Fluorescence life time	*300 μs* [8]	*420 μs* [8]

Sigma-Tau product ($\sigma_{em}\tau$)	*1800×10^{-20} μs cm^2*	*336×10^{-20} μs cm^2*
Thermal conductivity (κ)	*(undopped) 2.7 W/m/K* [8]	*(undopped) 6.5 W/m/K* [8] *(2-at. % doped)* [5] *κ_c=6.3 W/m/K, κ_a=6.9 W/m/K*
Thermal expansion coefficient (α_t)	*N_g-cut crystal* *N_m ($\alpha_m=10.8\times10^{-6}$) K^{-1}* *N_p ($\alpha_p=2\times10^{-6}$) K^{-1}*[9]	*($\alpha_a=10.0\times10^{-6}$) K^{-1}* *($\alpha_c=16.0\times10^{-6}$) K^{-1}*[10]
Thermo-optic coefficient (dn/dT)	*N_g-cut crystal* *$dn_p/dT= -14.17\times10^{-6}$ K^{-1}* *$dn_m/dT= -8.64\times10^{-6}$ K^{-1}*[1, 9]	*a-cut crystal* *$dn_o/dT= -7.6\times10^{-6}$ K^{-1}* *$dn_e/dT= -8.6\times10^{-6}$ K^{-1}*[10]
Nonlinear refractive index (n_2)	8.7×10^{-16} cm^2/W [11]	*9×10^{-16} cm^2/W* [4]
Emission bandwidth	*~ 24 nm* [8]	*~ 80 nm* [8]
Minimum theoretical pulse duration	*46 fs*	*14 fs*

The refractive index of any transparent medium can be calculated using the Sellmeier equations. The Sellmeier equations and corresponding constants for the Yb:KYW and Yb:CALGO crystals are given in Table 2-2.

Table 2-2: Sellmeier equations and constants for KYW and CALGO.

Crystal	**Sellmeier equation**	**Constants**		
KYW [6, 12]	$n^2_{g,m,p} = A_{g,m,p} + \frac{B_{g,m,p}\lambda^2}{\lambda^2 - C_{g,m,p}}$	*A_g=1* *B_g=3.1278346* *C_g=0.02608613*	*A_m=1* *B_m=2.9568303* *C_m=0.02534002*	*A_p=1* *B_p=2.8134935* *C_p=0.02338012*
CALGO [7]	$n^2_{a,c} = A_{a,c} + \frac{B_{a,c}}{\lambda^2 - C_{a,c}} - D_{a,c}\lambda^2$	*A_a=3.64774* *B_a=0.03889* *C_a=0.02277* *D_a=0.01109*		*A_c=3.74053* *B_c=0.03861* *C_c=0.02084* *D_c=0.01263*

Another important parameter is the intensity dependent refractive index, also known as the nonlinear refractive index. Intensity dependent refractive index is linked to the third-order nonlinear optical properties. The intensity dependence of the refractive index is described by equation 2.1.

$$n = n_0 + n_2 I \quad (2.1)$$

The n_0 is the refractive index of the medium with no laser beam present, I is the laser intensity and n_2 is the coefficient of the intensity dependent refractive index. The nonlinear refractive index, n_2, is necessary for ultrashort pulse generation using Kerr-lens mode locking (KLM). Generally, values for n_2 are difficult to determine and contain large errors. The measurement of the nonlinear index of refraction is often done with the z-scan technique [13, 14]. Yb:KYW and Yb:CALGO have significantly higher values of the n_2 than Ti:Sapphire. More details are given in Table 2-3.

Table 2-3: Nonlinear refractive indices of Yb:KYW, Yb:KGW, Yb:CALGO and Ti: Sapphire.

Material	Nm axis (cm^2/W)	Np axis (cm^2/W)	Ng axis (cm^2/W)	Reference
Yb:KYW	19×10^{-16}	15×10^{-16}	-----	[15]
Yb:KGW	$(\sim20\text{-}25)\times10^{-16}$	$\sim15x10^{-16}$	-----	[16] [15]
Yb:CALGO	9×10^{-16} cm^2/W (axis not specified)			[4]
Ti:sapphire	$(\sim2.8\text{-}3.3)\times10^{-16}$ cm^2/W (c-axis)			[17]

2.2.2 Absorption cross-section and Emission cross-section

Yb:KYW has different absorption and emission cross-sections for different polarizations and the highest are along the N_m axis as shown in Fig. 2-1. High emission cross section results in high gain and also good stability in mode-locked operation [18]. Another major advantage of Yb:KYW gain medium is that its absorption peak along the N_m axis (981 nm) exactly matches the emission from the commercially available low cost InGaAs laser diodes. Typical values of the absorption and emission cross-sections are shown in Table 2-4.

Table 2-4: Typical values of absorption and emission cross-section of Yb:KYW and Yb:CALGO

Parameter	Typical values	
	Yb:KYW	Yb:CALGO

Peak absorption wavelength	*981.2 nm* [19]	*979.5 nm* [3]
Peak absorption cross-section	$13.3\times 10^{-20}\ cm^2$ [19] (E || N_m)	$2.6\times 10^{-20}\ cm^2$ [3] (π-pol.)
Peak emission cross-section	$3\times 10^{-20}\ cm^2$ *at 1025 nm* [19] (E || N_m)	$0.8\times 10^{-20}\ cm^2$ *at 1050 nm* [8] (σ-pol.)

Yb:CALGO has medium absorption and emission cross-section among the Yb-doped crystals (see Fig. 2-2). Therefore a slightly longer crystal was used in the experiments. The peak absorption and emission cross-sections of Yb:CALGO are shown in Table 2-4. Fig. 2-2 clearly shows that for Yb:CALGO, π-polarization is favorable for absorption at 979.5 nm and σ-polarization is favorable for emission at 1050 nm.

Yb:KYW

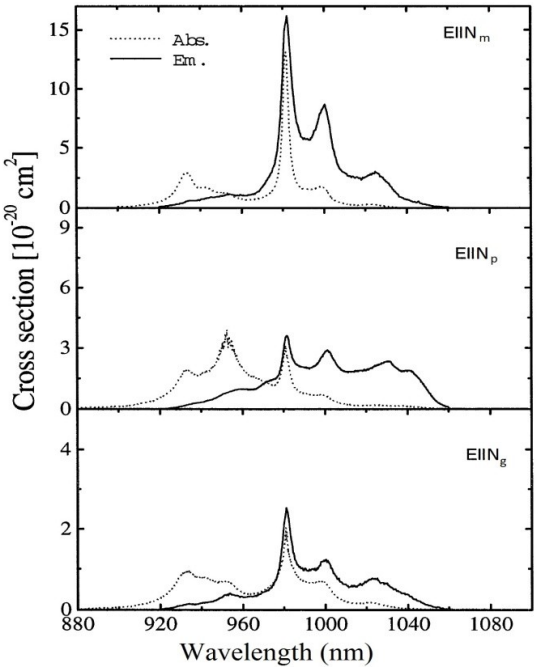

Fig. 2-1: Polarized absorption and emission cross-sections of Yb:KYW at room temperature [19].

Yb:CALGO

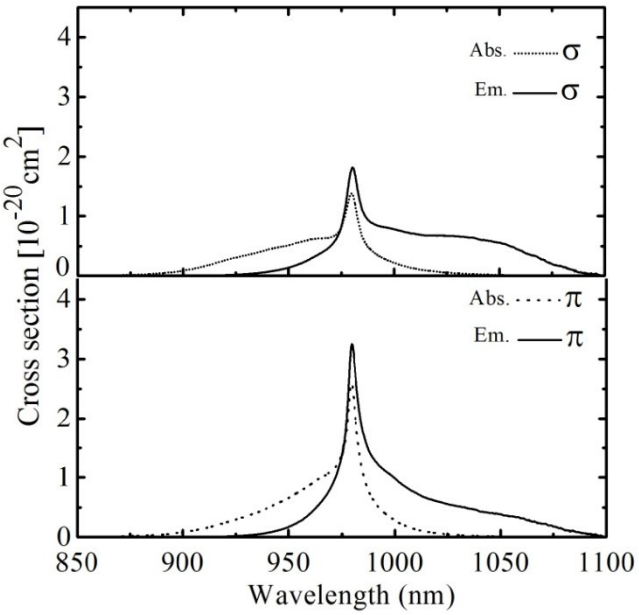

Fig. 2-2: Polarized absorption and emission cross-sections of Yb:CALGO at room temperature [3].

2.2.3 Energy level diagram

The energy levels of laser crystals are determined using spectroscopic analysis and crystal-field calculations [20]. In Yb-doped materials the upper manifold $^2F_{5/2}$ and the lower manifold $^2F_{7/2}$ are split into sub-levels due to Stark-splitting. In the case of Yb:KYW the upper manifold splits into three sublevels and the lower manifold splits into 4 sublevels (see Fig. 2-3). The excited electrons in higher sublevels of $^2F_{5/2}$ will decay into upper laser level through a fast nonradiative decay. The lower laser levels are very close to the ground state (see Fig. 2-4) and are thermally populated. This results in reabsorption loss of the produced laser radiation. This can be seen from the overlap of the emission and absorption spectra shown in Fig. 2-1 and Fig. 2-2.

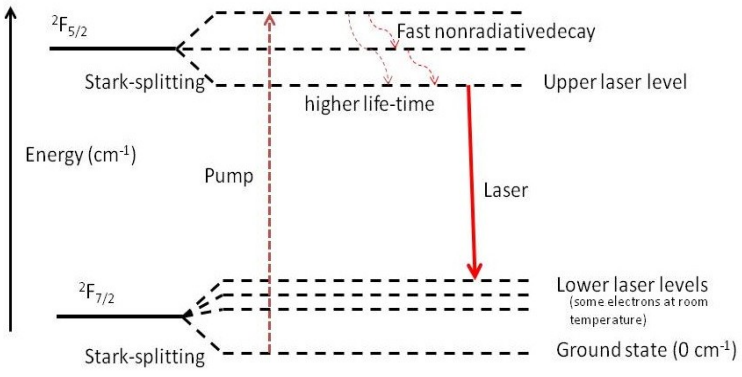

Fig. 2-3: Energy-level diagram of typical Yb-doped gain medium.

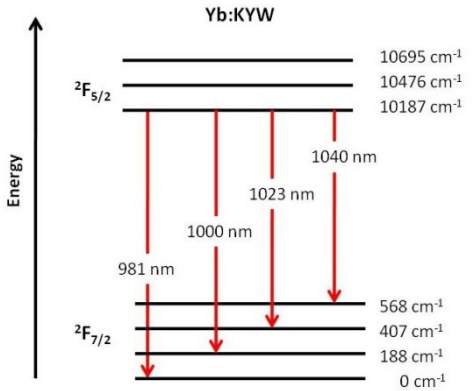

Fig. 2-4: Energy-level diagram of Yb:KYW [19, 21].

2.3 Laser design

The Yb:KYW gain medium was a 3-mm-long Ng-cut KYW crystal with 5% Yb^{3+} doping concentration (Altechna) and 1.2 mm of height (Fig. 2-5). The Yb:CALGO gain medium was a 5 mm-long a-cut Yb^{3+} (2%) doped CALGO crystal (Castech) (Fig. 2-6). The length of the crystals were chosen considering the reabsorption losses due to the quasi-three-level nature of laser transition. The crystals were anti-reflection (AR) coated to reduce the intracavity losses. The crystals were covered in indium foil of thickness 125 μm for better heat removal. Crystal

dimensions are shown in Fig. 2-5 and Fig. 2-6.

Yb:KYW	**Yb:CALGO**
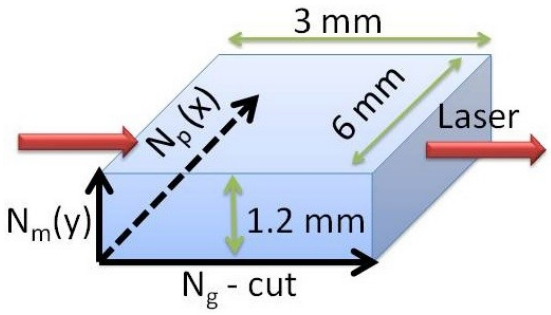	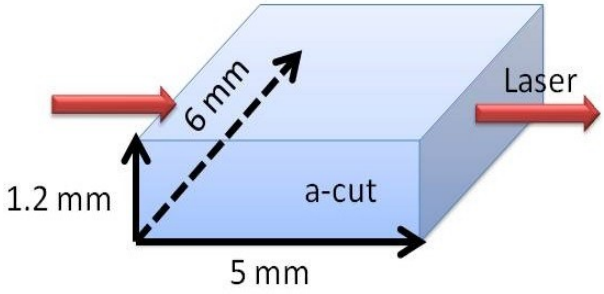
Fig. 2-5: Schematic of 3 mm long Ng-cut Yb:KYW crystal.	Fig. 2-6: Schematic of 5 mm long a-cut Yb:CALGO crystal.

2.3.1 Diode pump laser

Diode lasers are compact, efficient and cost effective way of pumping solid-state lasers. The choice of the diode lasers are limited by the emission wavelengths. The emission wavelength of the diode laser should match the absorption band of a given solid-state laser. InGaAs laser diodes are suitable choice for pumping Yb-doped gain medium. The crystals were pumped at 980 nm with a fiber-coupled diode laser (0.12 NA, 105 µm core diameter, $M^2 \sim 20$, IPG Photonics, PLD-30 Series) (See Fig. 2-7 and Fig. 2-8). This diode laser was capable of producing up to 25 W of output power at 11 A of input current. The pump radiation was unpolarized.

The pump laser was mounted on a water cooled copper heat sink. The water flow rate was 700 ccm per minute. The laser was isolated from the optical table using a Teflon spacer (Fig. 2-8). The photograph of the diode pump laser mounted to the copper water cooling block is shown in Fig. 2-9. The pump power was found to increase approximately linearly with the input current and is shown in Fig. 2-10. The power absorbed by the gain media when increasing the input current is also plotted in Fig. 2-10. The absorbed pump power was measured under non-lasing conditions. As more current (1 - 12 A) was injected into the diode laser, its temperature

increased and the center wavelength of output radiation shifted from 970 nm to 980 nm (Fig. 2-10). The maximum pump absorption was observed around 981 nm as expected.

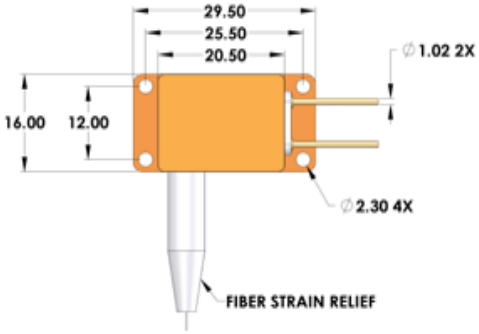

Fig. 2-7: Schematic of a compact diode laser. All the dimensions are in mm. The laser diode is fiber coupled.

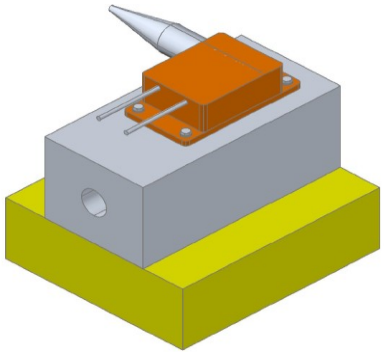

Fig. 2-8: Schematic of a laser diode mounted on a water cooled copper heat sink on the top of Teflon spacer.

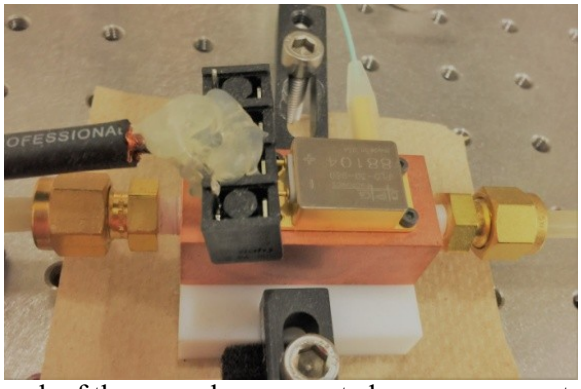

Fig. 2-9: Photograph of the pump laser mounted on a copper water cooling block.

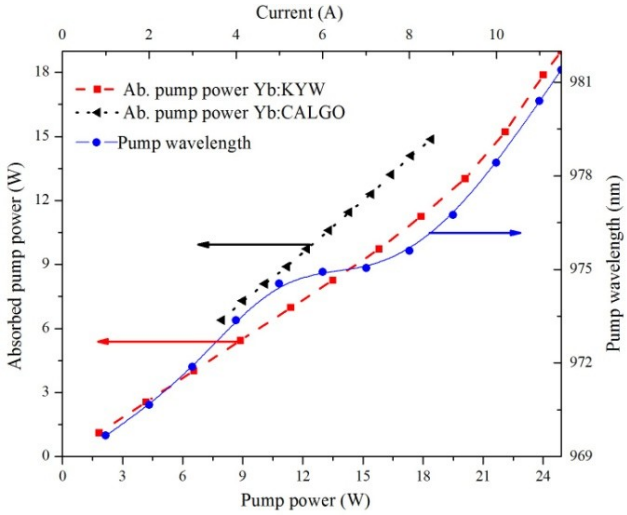

Fig. 2-10: Measured pump power absorption in Yb:KYW and Yb:CALGO crystals (left-axis). Variation of pump wavelength with respect to pump power (right axis).

2.3.2 Thermal management (Cooling system)

The laser crystals were water cooled at a rate of 700 cm^3/min and were wrapped in indium foil of thickness 125 um for better heat removal. The heating of the laser material by the absorbed pump radiation and surface cooling required for heat extraction leads to non-uniform temperature distribution inside the crystal. The temperature will be maximum at the centre and minimum at the cooling surface. The temperature gradient will lead to refractive index gradient and thus will result in lensing effect inside the gain medium. One of the initial challenges was to design a crystal holder that would not hinder the path of the laser beam. Fig. 2-11 shows AutoCAD drawing of the crystal holder design with water connectors attached to it. It was made with aluminium and the white coloured tubes shown in Fig. 2-12 were used to connect that to a chiller set at a temperature of 16°C. They were mounted on the hex-key driven XYZ-stage (Newport MDS-40 series) which has a precision of 1 μm step control.

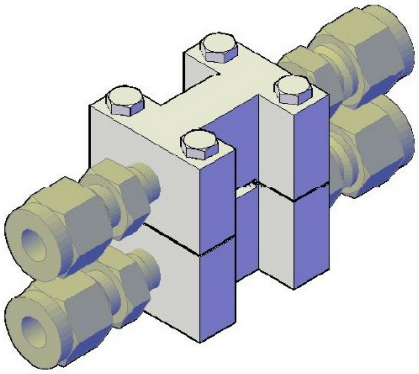

Fig. 2-11: AutoCAD drawing of the custom made laser crystal holder.

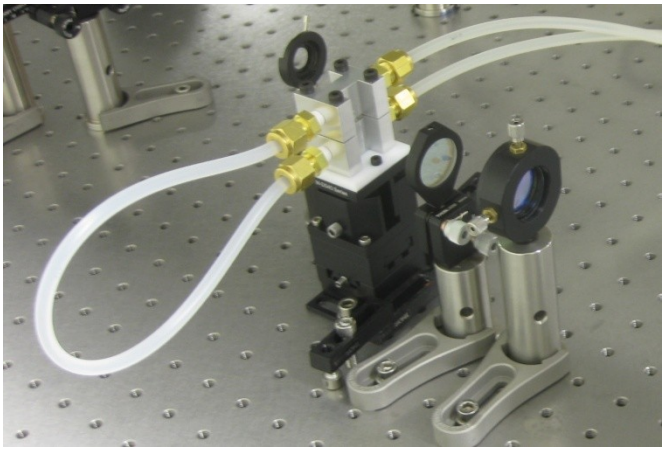

Fig. 2-12: Mounted crystal holder on XYZ micro stage and connected to a water chiller using plastic tubes.

2.3.3 CW laser design

Ray tracing analysis using a matrix method was used for laser cavity design and stability analysis. The laser cavity was designed with the help of two software packages, namely, LASCAD (LASer Cavity Analysis & Design) and reZonator. The cavity mode size in the crystal was approximately 319 μm. The pump beam from the fiber coupled diode laser was focused

(imaged) to the center of the laser crystal with the help of two spherical lenses. The pump spot diameter in the crystal was 350 µm. The pump laser beam entered into the laser cavity through a dichroic mirror. The dichoric mirror is transparent for the pump wavelength (980 nm) but is highly reflective at the lasing wavelength (1040 nm). The standard laser cavity used for CW lasers is shown in Fig. 2-13. The laser cavity had a high reflection mirror (HR mirror) and two concave mirrors with radius of curvature M1 = 500 mm and M2 = 750 mm.

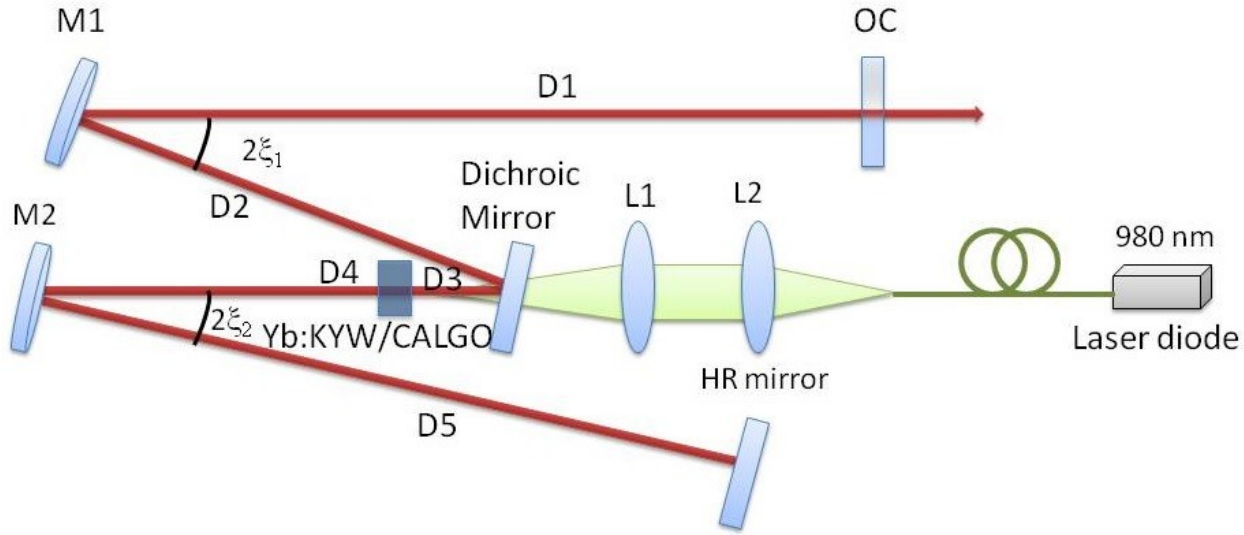

Fig. 2-13: Yb:KYW/CALGO laser cavity. The distances used are: D1= 1000 mm, D2 +D3 = 408 mm, D4= 300 mm, D5= 550 mm. L1 and L2 are spherical mirrors with f = 150 mm and f = 50 mm respectively. The curved mirrors are M1= -750 mm and M2= -500 mm. The angles are $\xi_1 = 4^0$, $\xi_2 = 4.9^0$(KYW), 4^0 (CALGO).

The three important things to consider while designing a laser cavity are 1) mode matching (see appendix A); 2) mode size at various elements; and 3) stability of the resonator. The lasing beam size should match exactly with the pump spot size for efficient energy transfer and for perfect Gaussian mode operation (TEM_{00} mode).

The pump laser has a lower beam quality (see Fig. 2-14) than the lasing beam and as a result the divergence is much higher for the pump beam. The beam quality factor (M^2) of the pump laser was calculated using Equation 2.2 and was estimated to be around 21 (for

comparison, a perfect Gaussian TEM_{00} mode has a beam quality factor of 1). However, the beam quality of lasing beam was typically less than 1.2. More about the beam quality and beam quality factor (M^2) measurement can be found in section 2.6.1 and appendix A.

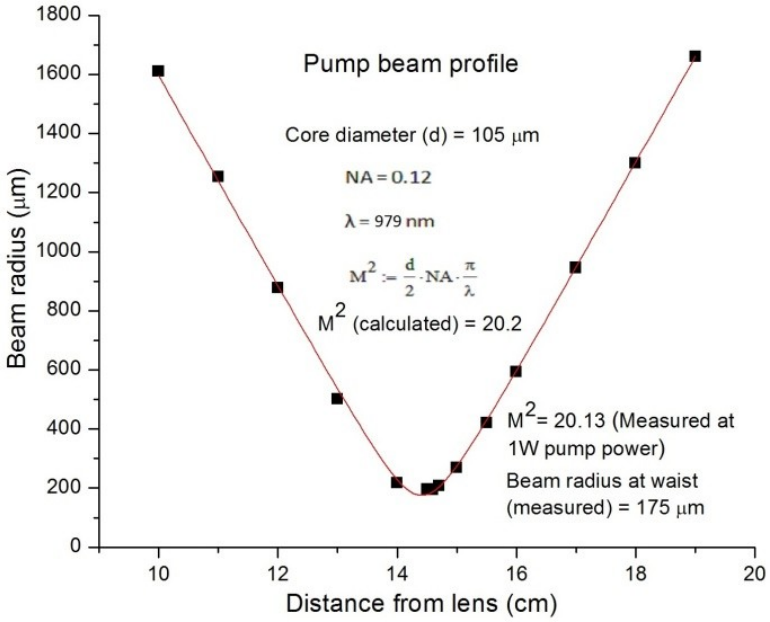

Fig. 2-14: Measured beam quality of pump laser operating at 1 W.

As can be seen the beam quality was about 18 times lower for the pump beam. This leads to a significant difference in mode propagation inside the laser crystal and it is shown in Fig. 2-15.

$$M^2 = \frac{d}{2} NA \frac{\pi}{\lambda} \qquad \text{Equation 2.2}$$

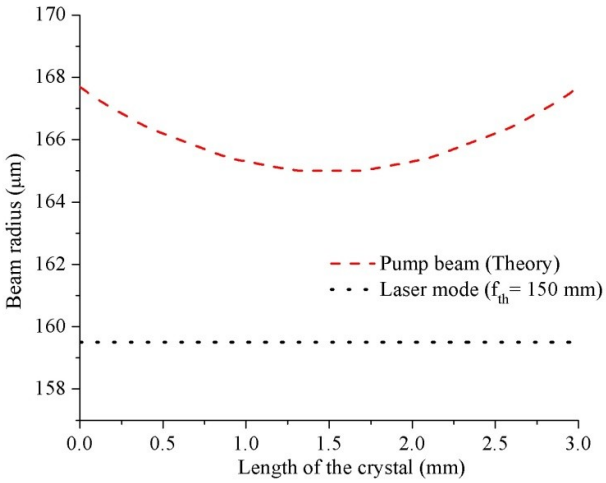

Fig. 2-15: Mode matching diagram for Yb:KYW. Divergence is significantly higher for the pump beam than for the lasing beam.

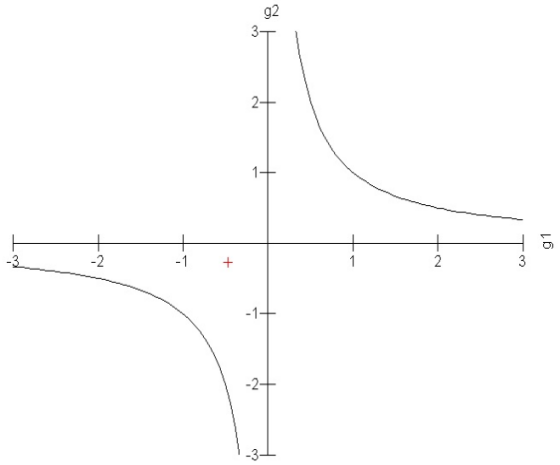

Fig. 2-16 : x-plane stability diagram. The laser operating point is shown as a red-cross mark (see appendix A).

The laser stability was calculated using g1 and g2 parameters (Fig. 2-16) (explained in appendix A). The red-cross mark in the Fig. 2-16 was well inside the stability region which indicates that the designed laser cavity above was stable. An image of one of the developed lasers on an optical bench is shown in Fig 2-17.

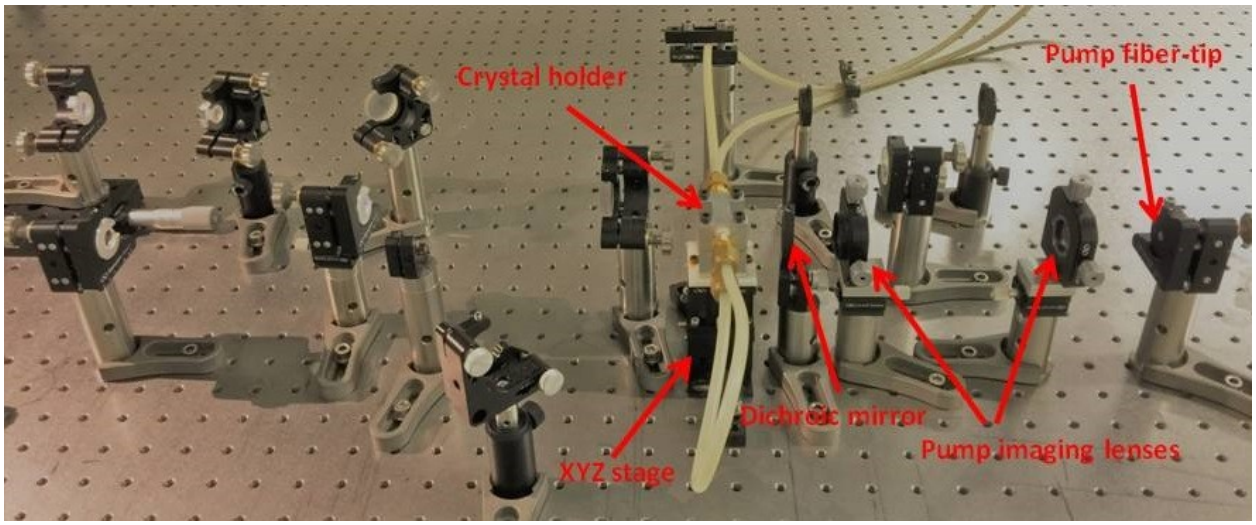

Fig 2-17: The developed laser on an optical table.

2.4 CW results for the Yb:KYW and Yb:CALGO lasers

The pump power was gradually increased while maintaining the temperature and monitoring the output wavelength of the diode to ensure efficient pump absorption (the center wavelength of the

used pump laser diode shifted from 970 nm to 981 nm due to temperature increase). Nearly 19 W of pump power was absorbed by the 3 mm long Yb:KYW crystal under non-lasing conditions for a pump power of 25 W. The maximum pump absorption was observed around 981 nm as expected. The best result for average output power of 9.03 W was obtained using an optimized output coupler transmission of 5%. The laser radiation had the E || N_p polarization.

In the case of the 5 mm long Yb:CALGO crystal, one of the best output powers measured was 8.01 W at a pump power of 24.1 W and the absorbed pump power of 19.2 W. The laser radiation had horizontal σ-polarization. The spectral width of the output radiations were less than 1 nm at full width at half maximum (FWHM). These results indicate high optical-to-optical efficiency and slope efficiency. The slope efficiency was measured with respect to the incident pump power as shown in Fig. 2-18. The output power shows nonlinear behavior which is common for quasi-three-level lasers. In high power regime the slope efficiency was measured to be 77.9% for Yb:KYW and 57.3% for Yb:CALGO.

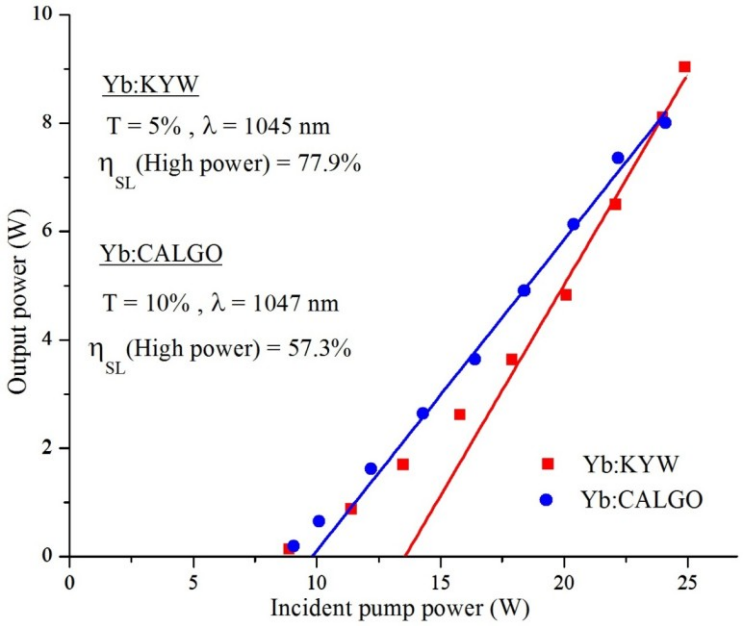

Fig. 2-18. Output power versus incident pump power for both lasers.

Similar method to calculate slope efficiency for high power regime was previously employed for Yb:KGW [22], Yb:KYF_4 [23], Yb:YVO_4 [24], and Yb:KLuW [25] lasers. The major reasons for this nonlinear plot (see Fig. 2-18) was the quasi-three-level nature of the Yb:KYW gain medium and the change in pump wavelength towards higher absorption region with increase in diode temperature at high power. Increased absorption around 981 nm of pump wavelength results in higher slope efficiency in high power regime. Moreover, the thermal lens was intentionally optimized for high power regime and also contributed to a higher slope efficiency. The sudden change in slope mostly happens about 2.5-3 times the threshold pump power [23, 26]. Another possible explanation for this behavior is that the absorption by the thermally populated lower laser level gets saturated at high pump intensity. Therefore, there will be a considerable reduction in re-absorption loss which results in subsequent increase in laser efficiency.

2.5 Efficiency comparison with other Yb-doped crystals

For the purpose of objective comparison, we only compared our results with previous experiments done with a single crystal in the cavity.

2.5.1 Optical-to-optical efficiency comparison

The optical-to-optical efficiecy (η_{o-o}) was calculated with respect to the incident pump power. At the highest output power of 9.03 W this corresponds to an η_{o-o} of 36% for Yb:KYW. At 8.01 W the η_{o-o} of Yb:CALGO was 33%. These results are affected by the incomplete pump absorption. A comparison of previous results in similar Yb-doped gain media with respect to the incident pump power is shown in Fig. 2-19. In addition to Yb:KGW/KLuW, Yb-doped silicate crystals (Yb:SSO and Yb:GSO) have so far led the group with high efficiency in the multi-Watt regime. However, in these cases the beam quality was not measured. On the other hand, the demonstrated optical-to-optical efficiency is the highest for the Yb:KYW lasers.

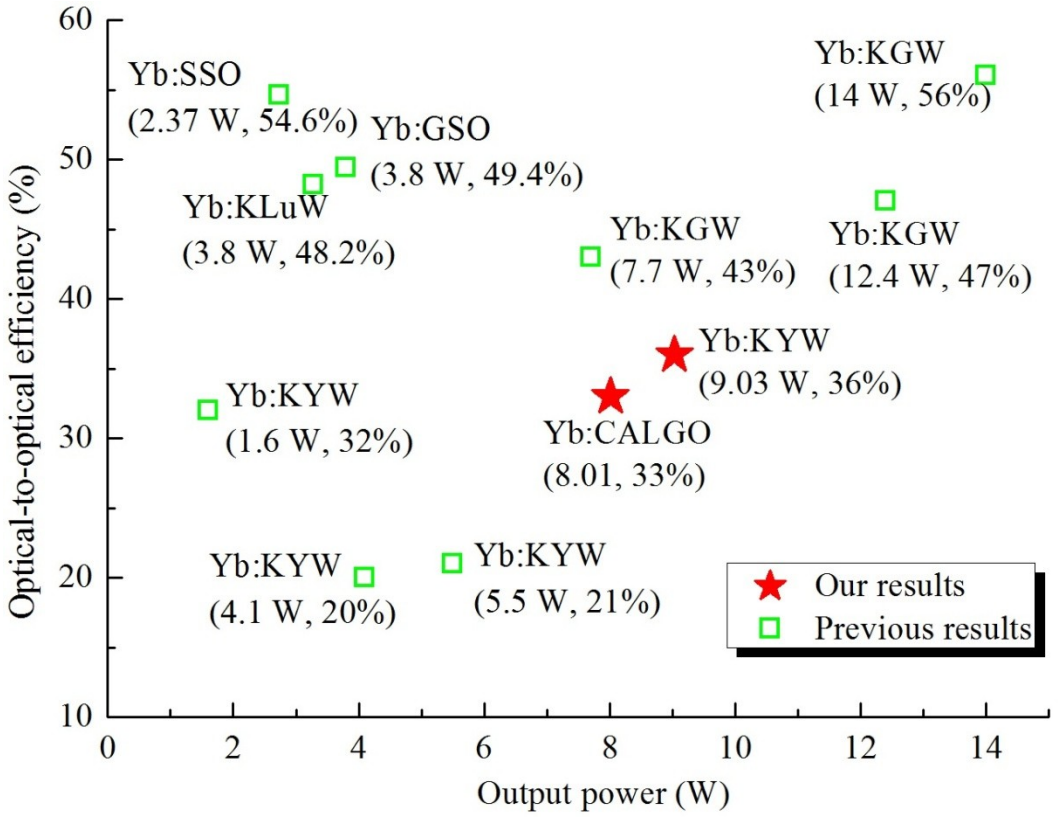

Fig. 2-19. Comparison of optical-to-optical efficiency results. The used data are: Yb:KGW (14 W, 56%) [27], Yb:SSO (2.37 W, 54.6%) [28], Yb:GSO (3.8 W, 49.4%) [29], Yb:KLuW (3.8 W,48.2%) [25], Yb:KYW (4.1 W, 20%) [30], Yb:KGW (7.7 W, 43%) [31], Yb:KGW (12.4 W, 47%) [22], Yb:KYW (5.5 W, 21%) [32].

2.5.2 Slope efficiency comparison

A comparison of slope efficiencies of single crystal Yb-doped lasers in the multi-Watt regime is shown in Fig. 2-20. The slope efficiency in each case was measured with respect to the incident pump power. The figure shows that other Yb-doped tungstate crystals like Yb:KLuW and Yb:KGW achieved high slope efficiency in high power regime. Our experiments also show that it is possible to achieve the same kind of results using Yb:KYW crystal.

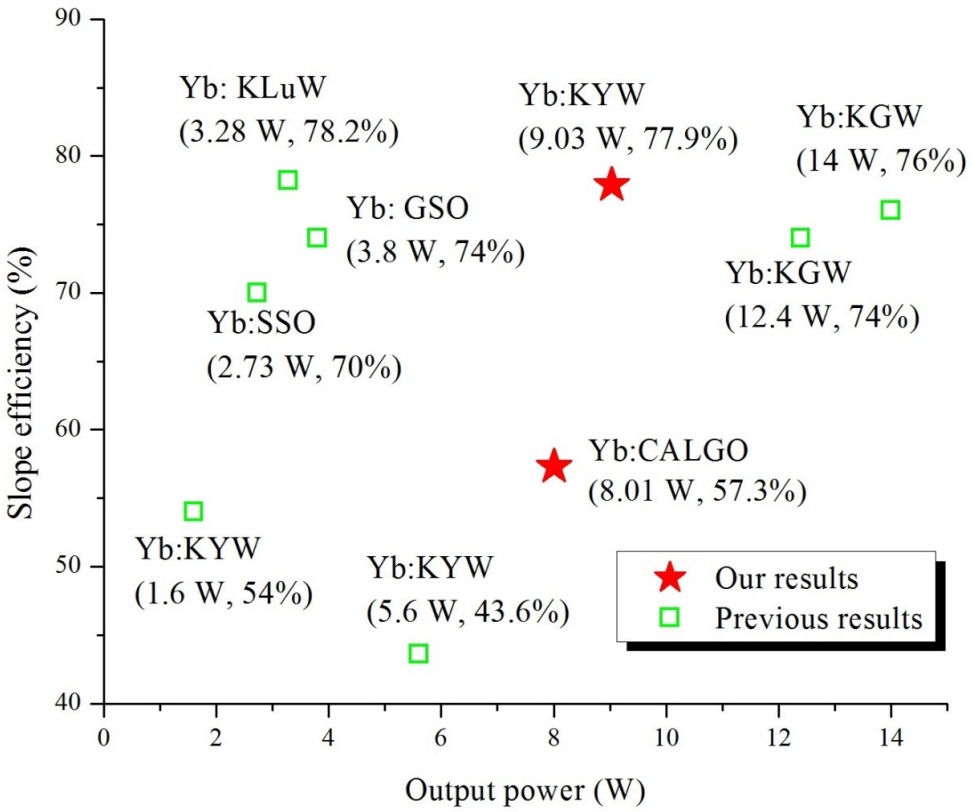

Fig. 2-20. Comparison of slope efficiencies. Data used are: Yb:KGW (14 W, 76%) [27] Yb:GSO (3.8 W, 74%) [29], Yb:KLuW (3.8 W, 78.2%) [25], Yb:KGW (12.4 W, 74%) [22], Yb:SSO (2.73 W, 70%) [28], Yb:KYW (1.6 W, 54%) [30], Yb:KYW (5.6 W, 43.6%) [33].

2.6 **Thermal Effects**

One of the issues that invariably arises during the operation of lasers is thermal lensing [34]. This effect is particularly important in high power regime, as it can lead to significant laser beam quality degradation, depolarization losses, laser ceasing due to the cavity instability, or even fracture of the laser crystal. Therefore, knowledge of thermal lens parameters in the gain medium is important in the design of the efficient high power laser systems. These parameters will strongly depend on the crystal orientation and laser polarization in anisotropic crystals.

2.6.1 Thermal lens and beam quality measurement in Yb:KYW and Yb:CALGO

The thermal lens was measured using a technique developed by H. Mirzaeian *et al*. [35, 36]. This technique was capable of measuring the thermal lens accurately by taking into account the beam quality factor M^2 variations at various pump intensities. This measurement technique has the potential to measure thermal lens values precisely even at low pump intensities. Under high power diode laser pumping, the formation of a positive thermal lens inside the crystal is shown in Fig. 2-21. The focal length of the thermal lens influences the beam divergence and beam diameter inside and outside of the resonator.

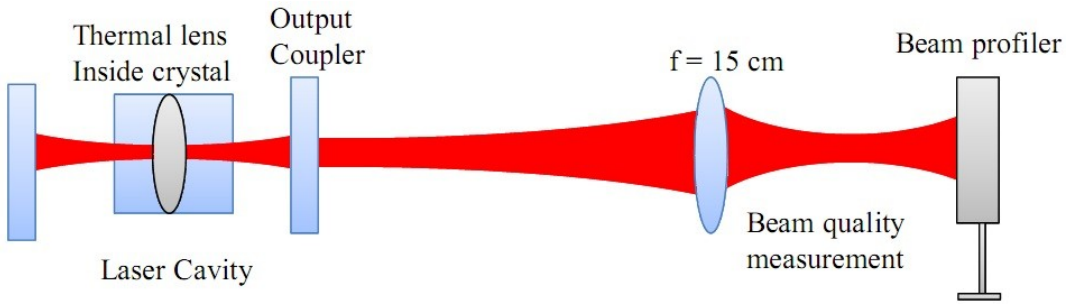

Fig. 2-21. Schematic diagram of thermal lens measuring set up.

Beam propagation matrix analysis was used for interior and exterior beam tracing. A lens was placed at some distance away from the output coupler and the beam size was measured at various points along the propagation direction immediately after the lens and this data was used to calculate the beam quality as shown in Fig. 2-21.

Further beam fitting was done with the help of the LASCAD software. In the process of beam fitting, the thermal lens in the crystal was given a specific value so that the resulting external beam simulated by LASCAD fitted exactly with the beam size experimentally measured after the lens. The measured beam quality factor M^2 was less than 1.2 in most of the cases (see Fig 2-22). The thermal lens was different for the x- and y-axes (horizontal and vertical

directions, respectively) as a result of different physical properties and cooling conditions along these axes. At the highest pump power, for Yb:KYW, the thermal lens (TL) was measured to be 11.1 diopters for the horizontal direction and 6.5 diopters for the vertical direction. The TL variation was very small for Yb:CALGO (4.6 Diopter – 6.9 Diopter) along the vertical direction (see Fig 2-23). Because of the very small variation of the TL along the horizontal axis, the TL analysis was not conducted in detail for Yb:CALGO.

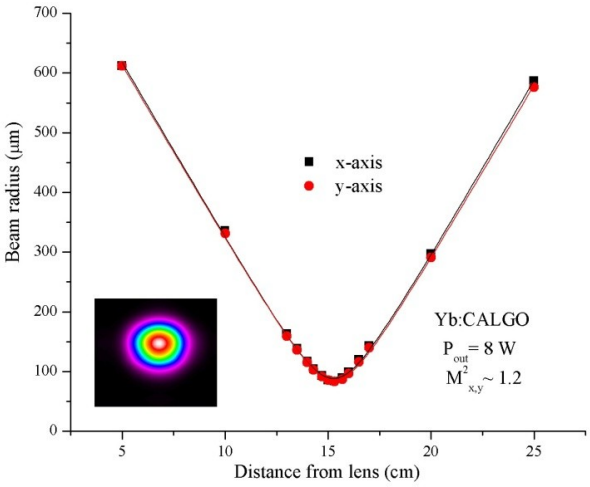

Fig 2-22: Measured beam quality for Yb:CALGO at 8W of output power. *Inset*: Beam profile.

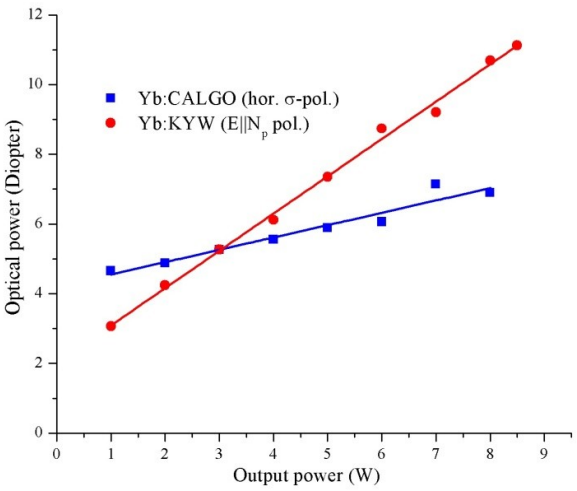

Fig 2-23: Comparison of TL values of Yb:CALGO and Yb:KYW along y-axis (vertical).

2.6.2 Evaluation of thermal parameters in Yb:KYW

The data taken using the above experimental method was used to evaluate the thermal lens parameters of Yb:KYW. The TL parameters were evaluated with the help of P. Loiko, ITMO University, Russia. The method of evaluation and the results can be found in [1] and the formulas used for evaluation are given in Table 2-6.

Thermal lensing was studied for two principal polarizations, E || N_m and E || N_p (see Fig. 2-24). To study the lasing with the E || N_m polarization a glass Brewster plate was introduced into the cavity. The Brewster plate induced some power loss and the maximum output power achieved for the E || N_m polarization was only 3.89 W. At high pump power the thermal lens

pushed the laser towards multimode operation (see Fig. 2-25 and Fig. 2-26). It resulted in beam distortion and therefore deteriorated the performance of the laser. A wavelength shift of about 6 nm was observed for the E || N_m polarization pointing out to the re-shaping of the beam by thermal lens [37] and subsequent change in reabsorption loss [38].

An explanation about the principal meridional planes of the thermal lens is presented in Fig. 2-24(a) and Fig. 2-24(b). Each of these planes contains the light propagation direction (N_g) and one of the N_m or N_p axes, so they can be shortly denoted as the *mg* or *pg* planes. The astigmatism of thermal lensing leads to the elliptical cross-section of the emerging laser beam, and the beam compression is due to the focusing action of the lens as described in Fig. 2-24 (c) and Fig. 2-24 (d).

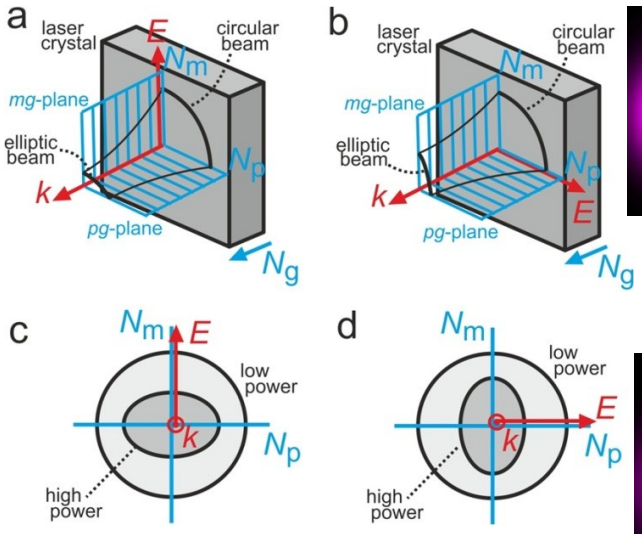

Fig. 2-24: Schematic of the thermal lens in the N_g-cut Yb:KYW crystal and resulting ellipticity of the laser beam: (a, b) position of the principal meridional planes of thermal lens, (c, d) transverse profiles of the laser beam [1].

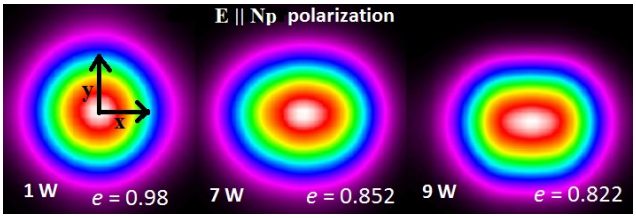

Fig. 2-25: Observed change in beam profile for E||N_p polarization at 1 W, 7 W and 9 W output power. *e* is the ellipticity.

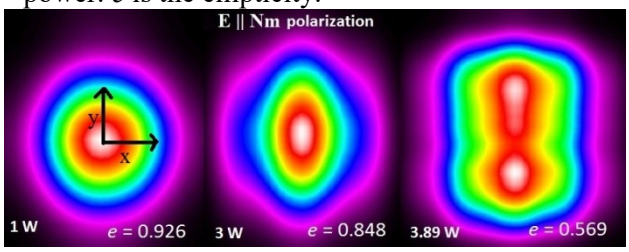

Fig. 2-26: Observed change in beam profile for E||N_m polarization at 1 W, 3 W and 3.89 W output power.

The optical powers of the induced thermal lens were deducted using the technique mentioned in section 2.6.1. The results for both polarizations are shown in Fig. 2-27 (a) and Fig. 2-27 (b). Both polarizations corresponded to a positive thermal lens. An example of the

evaluation of the $M^2_{x,y}$ values of the E||N_p at the maximum studied P_{abs}= 18.4 W is shown in Fig. 2-28.

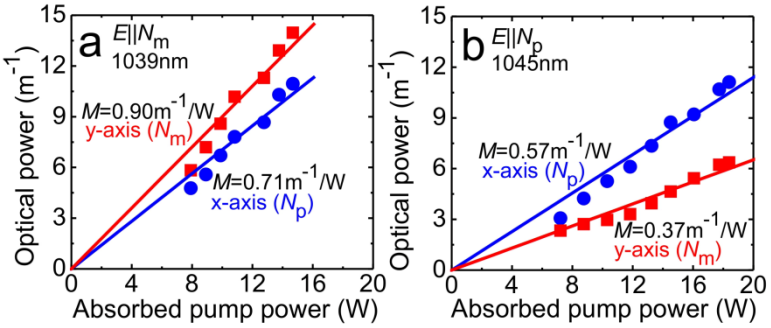

Fig. 2-27: Optical power of the thermal lens versus the absorbed pump power in the N_g-cut cut Yb:KYW crystal for the E||N_m (a) and E||N_p (b) polarizations, *points*: experimental data, *lines*: fitting for the calculation of the sensitivity factors (M), *circles and squares* stand for the direction of the N_p and N_m axes, respectively.

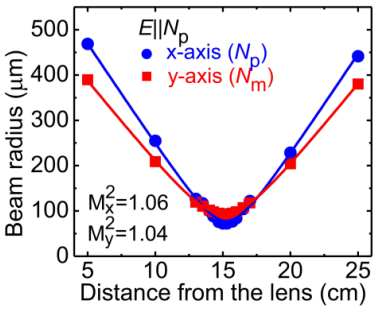

Fig. 2-28: Evaluation of the $M^2_{x,y}$ parameters of an output beam of the Yb:KYW laser (with E||N_p) at the maximum absorbed pump power, P_{abs}=18.4 W. *points*: Measured beam radius after the focusing lens (see Fig. 2-21), *curves:* their parabolic fits.

Parameters of the thermal lens that are critical for laser design in high power regime were also determined (see Table 2-5). At first, the thermo-optic coefficient (TCOP) of Yb:KYW was calculated from the data points. TCOP does not directly express the parameters of the thermal lens; however it can be used for an estimation of its sign and relative magnitude. One can expect a weaker lens for the E || N_p than for the E || N_m according to the lower TCOP. The evaluated photoelastic term (P_{PE}) represents the total variation of the optical path length induced by the thermal strains.

The sensitivity factor (M-factor) was the increase of the thermal lens optical power on absorption of 1 W of pump power. M-factor was evaluated from the data points for the considered meridional plane for 1W variation of the absorbed pump power. The M-factor of the thermal lens is inversely proportional to the square of the pump spot area. Another sensitivity factor (M'-factor) was also evaluated, which was independent of the pump configuration. M'-factor was defined with respect to the intensity of the absorbed pump power. The importance of

the M'-factor is that it can be used for calculation of the thermal lens in Yb:KYW for any pump spot size. Another evaluated parameter was thermal figure-of-merit (FOM). The larger the FOM, the more suitable is a laser material for power scaling. The equations used to calculate the thermal lens parameters are given in Table 2-6.

Table 2-5: Evaluated parameters of the thermal lens for the N_g-cut Yb:KYW crystal

Parameter	**Polarization**[a]	
	E||N_m	**E||N_p**
Laser wavelength	*1039 nm*	*1045 nm*
Fractional heat load	*0.066*	*0.068*
Sensitivity factor M, m^{-1}/W	*0.90 (mg)*	*0.37 (mg)*
	0.71 (pg)	*0.57 (pg)*
Sensitivity factor M', $m^{-1}/[kW/cm^2]$	*0.94 (mg)*	*0.40 (mg)*
	0.74 (pg)	*0.59 (pg)*
Astigmatism S, m^{-1}/W	*0.19*	*0.20*
Astigmatism degree, S/W	*21%*	*35%*
Thermal FOM, 10^{15} W/m	*4.26*	*7.44*
Generalized thermo-optic coefficient (TOC) χ, 10^{-6} K^{-1}	*7.58 (mg)*	*3.11 (mg)*
	5.98 (pg)	*4.66 (pg)*
dn/dT, 10^{-6}, K^{-1} [39]	*-8.64*	*-14.17*
Photoelastic term[b] P_{PE}, 10^{-6}, K^{-1}	*-1.30 (mg)*	*0.43 (mg)*
	-2.90 (pg)	*1.98 (pg)*
End-bulging term[c], 10^{-6}, K^{-1}	*17.82*	*16.85*

[a]*Meridional planes are denoted in brackets, if applicable*
[b]*Estimated as* $P_{PE} = \chi - \frac{dn}{dT} - (n-1)\alpha$. *(see appendix B)*
[c]*Determined solely by the thermal expansion, (n-1)α.*

Table 2-6: List of thermal lens parameters and equations.

Parameter	**Equation**	
Fractional heat load	$\eta_h = 1 - \eta_p \left[(1-\eta_L)\eta_r \frac{\lambda_p}{\lambda_L} + \eta_L \frac{\lambda_p}{\lambda_L} \right]$	2.3
Sensitivity factor, M m^{-1}/W	$M_{mg(pg)} = \frac{d\, D_{mg(pg)}}{d\, P_{abs}}$	2.4
Sensitivity factor, M' $m^{-1}/(kW/cm^2)$	$M'_{mg(pg)} = \frac{d\, D_{mg(pg)}}{d\, (P_{abs}/\pi\omega_p^2)}$	2.5

Astigmatism degree	$S/M = \frac{\left\|M_{mg} - M_{pg}\right\|}{M_{max}}$	2.6
Thermal figure-of-merit W/m	$FOM_{m(p)} = \frac{1}{\langle M \rangle_{m(p)}} \frac{(\eta_h)_{m(p)}}{2\pi\omega_p^2}$	2.7
Generalized thermo-optic coefficient (TOC) χ, 10^{-6} K^{-1}	$\chi_{mg(pg)} = M_{mg(pg)} \frac{2\pi\langle\kappa\rangle\omega_p^2}{(\eta_h)_{m(p)}}$	2.8
Photoelastic term P_{PE}, 10^{-6}, K^{-1}	$(P_{PE})_{mg(pg)} = \chi_{mg(pg)} - \frac{dn_{m(p)}}{dT} - (n_{m(p)} - 1)\alpha_g$	2.9

Symbol	
η_L	*Laser extraction efficiency*
η_p	*Pump quantum efficiency*
η_r	*Radiative quantum efficiency*
D	*Optical power of lens in diopter*
S	*Astigmatism*
κ	*Thermal conductivity*
P_{abs}	*Absorbed pump power*
ω_p	*Pump radius*

2.7 **Conclusion**

In summary, the advantage of Yb:KYW are high emission cross-section and the possibility of high doping concentration. The disadvantages are medium thermal conductivity and medium gain bandwidth. On the other hand, the advantages of Yb:CALGO are broad gain bandwidth and high thermal conductivity. However, the drawback is medium emission cross-section. Thermal lensing was studied in an N_g-cut monoclinic Yb:$KY(WO_4)_2$ (Yb:KYW) laser crystal under high-power diode pumping for the two principal light polarizations, $E \parallel N_m$ and $E \parallel N_p$. For both polarizations, thermal lens (TL) was positive. The unfortunate events of several crystal damages to Yb:KYW forced us to continue the project using Yb:CALGO alone. Yb:CALGO has higher thermal conductivity and therefore a lower chance of damage. As a precautionary measure, further experiments were not conducted at full pump power potential, unless it was necessary.

2.8 References

[1] P. Loiko, S. Manjooran, K. Yumashev, and A. Major, "Polarization anisotropy of thermal lens in Yb:$KY(WO_4)_2$ laser crystal under high-power diode pumping," *Applied Optics,* vol. 56, pp. 2937-2945, 2017.

[2] P. Wasylczyk and C. Radzewicz, "Design and Alignment Criteria for a Simple, Robust, Diode-Pumped Femtosecond Yb:KYW Oscillator," *Laser Physics,* vol. 19, p. 5, 2009.

[3] P. Loiko, J. M. Serres, X. Mateos, X. Xu, J. Xu, V. Jambunathan*, et al.*, "Microchip Yb:CaLnAlO4 lasers with up to 91% slope efficiency," *Optics Letters,* vol. 42, pp. 2431-2434, 2017.

[4] J. Boudeile, F. Druon, M. Hanna, P. Georges, Y. Zaouter, E. Cormier*, et al.*, "Continuous-wave and femtosecond laser operation of Yb:$CaGdAlO_4$ under high-power diode pumping," *Optics Letters,* vol. 32, pp. 1962-1964, 2007.

[5] J. Petit, P. Goldner, and B. Viana, "Laser emission with low quantum defect in Yb:$CaGdAlO_4$," *Optics Letters,* vol. 30, pp. 1345-1347, 2005.

[6] A. A. Kaminskii, A. F. Konstantinova, V. P. Orekhova, A. V. Butashin, R. F. Klevtsova, and A. A. Pavlyuk, "Optical and nonlinear laser properties of the $\chi^{(3)}$-active monoclinic α-$KY(WO_4)_2$ crystals," *Crystallography Reports,* vol. 46, pp. 665-672, 2001.

[7] Q. Hu, Z. Jia, C. Tang, N. Lin, J. Zhang, N. Jia*, et al.*, "The origin of coloration of CaGdAlO4 crystals and its effect on their physical properties," *CrystEngComm,* vol. 19, pp. 537-545, 2017.

[8] F. Druon, F. Balembois, and P. Georges, "New laser crystals for the generation of ultrashort pulses," *Comptes Rendus Physique,* vol. 8, pp. 153-164, 2007.

[9] P. A. Loiko, K. V. Yumashev, N. V. Kuleshov, G. E. Rachkovskaya, and A. A. Pavlyuk, "Detailed characterization of thermal expansion tensor in monoclinic $KRe(WO_4)_2$ (where Re = Gd, Y, Lu, Yb)," *Optical Materials,* vol. 34, pp. 23-26, 2011.

[10] P. Loiko, F. Druon, P. Georges, B. Viana, and K. Yumashev, "Thermo-optic characterization of Yb:$CaGdAlO_4$ laser crystal," *Optical Materials Express,* vol. 4, pp. 2241-2249, 2014.

[11] K. V. Yumashev, N. N. Posnov, P. V. Prokoshin, V. L. Kalashnikov, F. Mejid, I. G. Poloyko*, et al.*, "Z-scan measurements of nonlinear refraction and Kerr-lens mode-locking with Yb^{3+}:$KY(WO_4)_2$," *Optical and Quantum Electronics,* vol. 32, pp. 43-48, 2000.

[12] X. Mateos, R. Solé, J. Gavaldà, M. Aguiló, J. Massons, and F. Díaz, "Crystal growth, optical and spectroscopic characterisation of monoclinic $KY(WO_4)_2$ co-doped with Er^{3+} and Yb^{3+}," *Optical Materials,* vol. 28, pp. 423-431, 2006.

[13] A. Major, J. S. Aitchison, P. W. E. Smith, F. Druon, P. Georges, B. Viana*, et al.*, "Z-scan measurements of the nonlinear refractive indices of novel Yb-doped laser crystal hosts," *Applied Physics B,* vol. 80, pp. 199-201, 2005.

[14] M. Sheik-bahae, A. A. Said, and E. W. Van Stryland, "High-sensitivity, single-beam n_2 measurements," *Optics Letters,* vol. 14, pp. 955-957, 1989.

[15] N. Thilmann, G. Strömqvist, M. C. Pujol, V. Pasiskevicius, V. Petrov, and F. Díaz, "Nonlinear refractive indices in Yb^{3+}-doped and undoped monoclinic double tungstates $KRE(WO4)_2$ " *Applied Physics B,* vol. 96, pp. 385-392, 2009.

[16] A. Major, I. Nikolakakos, J. S. Aitchison, A. I. Ferguson, N. Langford, and P. W. E. Smith, "Characterization of the nonlinear refractive index of the laser crystal Yb:KGd(WO_4)$_2$," *Applied Physics B,* vol. 77, pp. 433-436, 2003.

[17] A. Major, F. Yoshino, I. Nikolakakos, J. S. Aitchison, and P. W. E. Smith, "Dispersion of the nonlinear refractive index in sapphire," *Optics Letters,* vol. 29, pp. 602-604, 2004.

[18] P. Klopp, V. Petrov, U. Griebner, and G. Erbert, "Passively mode-locked Yb:KYWlaser pumped by a tapered diode laser," *Optics Express,* vol. 10, pp. 108-113, 2002.

[19] N. V. Kuleshov, A. A. Lagatsky, A. V. Podlipensky, V. P. Mikhailov, and G. Huber, "Pulsed laser operation of Yb-doped KY(WO_4)$_2$ and KGd(WO_4)$_2$," *Optics Letters,* vol. 22, p. 3, 1997.

[20] L. Zheng, L. Su, and J. Xu, "Growth and Characterization of Ytterbium Doped Silicate Crystals for Ultra-Fast Laser Applications," in *Modern Aspects of Bulk Crystal and Thin Film Preparation*, N. Kolesnikov, Ed., ed: InTech, 2012.

[21] F. Balembois, M. Castaing, P. Georges, and T. Georges, "Line competition in an intracavity diode-pumped Yb:KYW laser operating at 981nm," *Journal of the Optical Society of America B,* vol. 28, pp. 115-122, 2011.

[22] J. E. Hellström, S. Bjurshagen, V. Pasiskevicius, J. Liu, V. Petrov, and U. Griebner, "Efficient Yb:KGW lasers end-pumped by high-power diode bars," *Applied Physics B,* vol. 83, pp. 235-239, 2006.

[23] G. Galzerano, P. Laporta, E. Sani, L. Bonelli, A. Toncelli, M. Tonelli*, et al.*, "Room-temperature diode-pumped Yb:KYF_4 laser," *Optics Letters,* vol. 31, pp. 3291-3293, 2006.

[24] V. E. Kisel, A. E. Troshin, N. A. Tolstik, V. G. Shcherbitsky, N. V. Kuleshov, V. N. Matrosov*, et al.*, "Spectroscopy and continuous-wave diode-pumped laser action of Yb^{3+}:YVO_4," *Optics Letters,* vol. 29, pp. 2491-2493, 2004.

[25] J. Liu, U. Griebner, V. Petrov, H. Zhang, J. Zhang, and J. Wang, "Efficient continuous-wave and Q-switched operation of a diode-pumped Yb:KLu(WO_4)$_2$ laser with self-Raman conversion," *Optics Letters,* vol. 30, pp. 2427-2429, 2005.

[26] T. Fan and R. Byer, "Modeling and CW operation of a quasi-three-level 946 nm Nd: YAG laser," *IEEE Journal of Quantum Electronics,* vol. 23, pp. 605-612, 1987.

[27] P. A. Loiko, V. E. Kisel, N. V. Kondratuk, K. V. Yumashev, N. V. Kuleshov, and A. A. Pavlyuk, "14W high-efficiency diode-pumped cw Yb:KGd(WO_4)$_2$ laser with low thermo-optic aberrations," *Optical Materials,* vol. 35, pp. 582-585, 2013.

[28] W. D. Tan, D. Tang, X. Xu, J. Zhang, C. Xu, F. Xu*, et al.*, "Passive femtosecond mode-locking and cw laser performance of Yb^{3+}: Sc_2SiO_5," *Optics Express,* vol. 18, pp. 16739-16744, 2010.

[29] W. Li, H. Pan, L. Ding, H. Zeng, W. Lu, G. Zhao*, et al.*, "Efficient diode-pumped Yb:Gd_2SiO_5 laser," *Applied Physics Letters,* vol. 88, p. 221117, 2006.

[30] G. H. Kim, G. H. Yang, D. S. Lee, A. V. Kulik, E. G. Sall', S. A. Chizhov*, et al.*, "High-power efficient cw and pulsed lasers based on bulk Yb : KYW crystals with end diode pumping," *Quantum Electronics,* vol. 42, pp. 292-297, 2012.

[31] F. Hoos, S. Li, T. P. Meyrath, B. Braun, and H. Giessen, "Thermal lensing in an end-pumped Yb:KGW slab laser with high powersingle emitter diodes," *Optics Express,* vol. 16, pp. 6041-6049, 2008.

[32] C. G. Leburn, C. Y. Ramírez-Corral, I. J. Thomson, D. R. Hall, H. J. Baker, and D. T. Reid, "Femtosecond pulses at 50-W average power from an Yb:YAG planar waveguide

amplifier seeded by an Yb:KYW oscillator," *Optics Express,* vol. 20, pp. 17367-17373, 2012.

[33] A. A. Kirpichnikova, S. A. Kuznetsov, and V. S. Pivtsov, "Studying a highly efficient Yb:KYW laser with diode pumping," in *Luminescence And Laser Physics*, 2014, pp. 169-172.

[34] S. Chénais, F. Druon, S. Forget, F. Balembois, and P. Georges, "On thermal effects in solid-state lasers: The case of ytterbium-doped materials," *Progress in Quantum Electronics,* vol. 30, pp. 89-153, 2006.

[35] H. Mirzaeian, S. Manjooran, and A. Major, "A simple technique for accuarte characterization of thermal lens in solid state lasers," *Proc. SPIE,* vol. 9288, p. 928802, 2014.

[36] S. Manjooran and A. Major, "Continuous wave multi-watt Yb:KYW laser with highly efficient diode pumping," in *Photonics North* Montreal, 2014, p. 157.

[37] H. Zhao and A. Major, "Orthogonally polarized dual-wavelength Yb:KGW laser induced by thermal lensing," *Applied Physics B,* vol. 122, pp. 163-169, 2016.

[38] H. Zhao and A. Major, "Dynamic characterization of intracavity losses in broadband quasi-three-level lasers," *Opt. Express,* vol. 22, pp. 26651-26658, 2014.

[39] P. A. Loiko, K. V. Yumashev, N. V. Kuleshov, and A. A. Pavlyuk, "Thermo-optical properties of pure and Yb-doped monoclinic $KY(WO_4)_2$ crystals," *Applied Physics B,* vol. 106, pp. 663-668, 2012.

Chapter 3: Dual-wavelength operation of Yb:CALGO laser

3.1 Introduction

This chapter presents the results of CW dual-wavelength operation of Yb:CALGO laser. Dual-wavelength study was not a part of the initial proposal, however, it was found that the developed CW laser could support dual-wavelength operation simply by inserting a birefringent quartz plate into the laser cavity designed in the previous chapter. The results presented in this chapter were a clear proof of the broad emission bandwidth of Yb:CALGO and indicated that the selected gain medium was a good choice for the final goal of intense ultrashort pulse generation. It also could be seen that the wavelength range of dual-wavelength operation presented in this chapter confirmed that the gain bandwidth of Yb:CALGO was broad enough to support sub-100 fs pulses.

Dual-wavelength lasers have been attractive for a wide range of applications such as laser spectroscopy, optical coherence tomography, THz generation and LIDAR instrumentation [1, 2]. Most of the earlier works on dual-wavelength lasers were either in low power (mW) regime or used complex designs. Examples of the complex designs are multi-ethalon configuration [2], Bragg gratings [3], moving mirror technique [4] or two adjacent pump spots in one crystal [5]. However, a dual-wavelength operation can be achieved in a simple way by introducing a single birefringent filter (BRF) plate into a standard laser cavity. BRF plates are wavelength dependent periodic loss elements and their free spectral range is mainly determined by their thickness [6]. Earlier experiments using BRF plates were carried out in the low power regime. A combination

of two BRF plates was tested by C. G. Trevino-Palacios et.al. [7] in a Ti:Sapphire laser. A frequency offset of 1 THz was achieved using BRF plates with thickness of 2.082 mm and 33.315 mm. Unfortunately, the output power was limited to less than 150 mW. Medium power (850 mW) dual-wavelength operation of alexandrite laser using a single BRF plate was demonstrated in Ref. [8]. At the same time, U. Demirbas *et al*. [9] used a tilted-optic axis (45°) BRF plate to generate dual-wavelength in Cr:Nd:GSGG and Cr:LiSAF with <370 mW of output power. The mode-locked operation of dual-wavelength Cr:Nd:GSGG was also demonstrated by the same group with an average output power of 45 mW [10].

Dual-wavelength operation based on rare-earth doped (Yb^{3+}, Nd^{3+}) gain media are of particular interest because of their ability to generate multi-watt output power owing to high emission cross-sections and relatively low heat loading that can be offered by diode laser pumping [11-14]. Nd^{3+}-doped materials are also well suited for multi-color operations [9, 15-17]. However, crystalline Nd^{3+}-doped materials are mostly limited by their available gain bandwidth [18]. In addition to that, the multiple sharp fluorescence peaks arising from transitions between the fixed electronic manifolds or transitions between the sublevels of the same manifold make it difficult to achieve dual-wavelength tunability.

In this context Yb^{3+}-doped materials are favourable because of their substantially broader gain bandwidths. In the past decade this was successfully utilized for efficient generation of ultrashort pulses [19-26] that are needed for a large number of applications [27-30]. At the same time multi-watt dual-wavelength outputs were also realized. Using an Yb:YCOB crystal, 3.14 W at 1084.3 nm and 3.45 W at 1061.3 nm [31] were produced using a custom made optics. However, the major limitations of the design were that it was working only with one specific output coupler mirror and the output wavelengths or their separations were not tunable. Yb^{3+}-

doped monoclinic double tungstates (MDTs), $KY(WO_4)_2$ and $KGd(WO_4)_2$ (shortly KYW and KGW) are also attractive candidates in terms of wavelength tunability, because of their relatively broad gain bandwidth [32]. The research works based on dual-wavelength MDT lasers are the following. Brenier *et al.* [33] generated dual-wavelength radiation using two volume Bragg gratings inside the laser cavity. H. Zhao *et al*. [34] generated a multi-watt dual-wavelength radiation with different polarizations based on anisotropic thermal lensing [35, 36]. Recently, R. Akbari *et al*. [37] demonstrated a multi-watt dual-wavelength output with single polarization using an Yb:KGW crystal and a single BRF plate. In both cases the free spectral range was limited to approximately 20 nm (the gain bandwidth of Yb:KYW and Yb:KGW is 16 nm and 20 nm, respectively [32]) which, therefore, puts constrains on the achievable dual-wavelength frequency offset range. As a result of this limited bandwidth, thin BRF plates (e.g. 2 mm-thick or thinner) could not produce dual-wavelength operation [37]. Another disadvantage of the MDTs is their moderate thermal conductivity (~3.0 $Wm^{-1}K^{-1}$ [38]) which makes these crystals prone to damage in a multi-watt operation regime.

On the other hand, Yb^{3+}-doped tetragonal calcium gadolinium aluminate $CaGdAlO_4$ (CALGO) has several advantages when compared with MDTs as was discussed prevously. High power dual-wavelength operation with Yb:CALGO laser gain medium is an attractive option because of its broad gain bandwidth (~80 nm) and high thermal conductivity (6.9 $Wm^{-1}K^{-1}$) [39]. This crystal is optically uniaxial [40, 41] and it has one of the highest thermal conductivities among other Yb^{3+}-doped crystals, which makes it suitable for high power operation [42-44]. Taking advantage of such unique properties, this chapter reports on a broad range of dual-wavelength operation by adjusting the thickness of a single BRF plate placed in the laser cavity. The demonstrated free spectral range discretely varied between 4.7 nm up to 47.1 nm depending

on the plate thickness and operated in a multi-watt regime.

3.2 Theory and Experiment

For dual-wavelength operation, a BRF plate was inserted into one of the arms of the laser cavity (see Fig. 3-1). The dual-wavelength spectra were recorded for BRF plates of thickness 2 mm, 4 mm and 6 mm using different output couplers. A single wavelength tuning was also tested using a 0.5 mm-thick plate. Each BRF used a quartz plate (Castech), a schematic of which is presented in Fig. 3-2. The BRF plate was placed at the Brewster angle to minimize the insertion loss and to act as a polarization-sensitive loss element. This allowed only the horizontal σ-polarization to oscillate inside the laser cavity. The maximum pump power absorbed under the non-lasing condition was 14.9 W at an incident pump power of 18.4 W. The design of a five mirror laser cavity took into account thermal lensing [45] and is shown in Fig. 3-1.

A simple simulation of transmission windows based on the average wavelength of 1047 nm and a 2 mm-thick BRF plate is shown in Fig. 3-3. As can be seen, if a laser gain medium with a broad spectral bandwidth is used, it is possible to introduce a wavelength-dependent loss such that only two distinct wavelengths benefit from the effective gain. In other words, the net-gain of the two particular wavelengths can be equalized by the combined action of the transmission window of the BRF plate and the gain curve of the crystal. The periodic transmission and the corresponding peak wavelength separation ($\Delta\lambda$) is inversely proportional to the BRF plate thickness (d). Therefore the broad gain bandwidth of Yb:CALGO crystal can accommodate two (or more) transmission windows of a BRF [37].

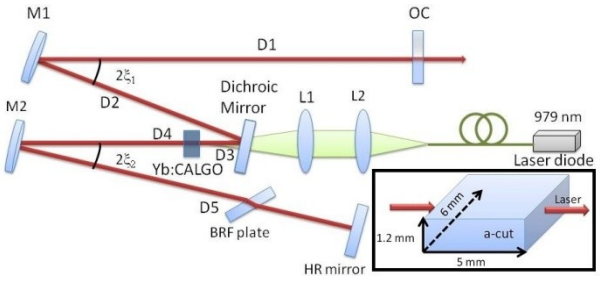

Fig. 3-1: Schematic of a laser cavity. The distances used were: D1= 1000 mm, D2 +D3 = 408 mm, D4= 300 mm, D5= 550 mm. Radii of curvature of the curved mirrors: M1 – -750 mm, M2 – -500 mm. The angles were $\xi_1 = \xi_2 = 4°$. OC, output coupler. *Inset* shows the crystal dimensions and orientation.

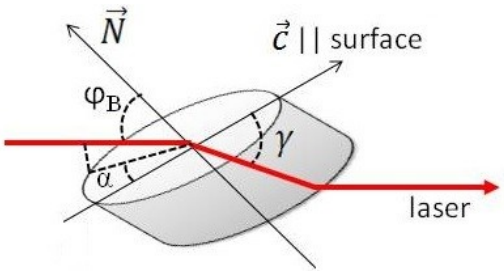

Fig. 3-2: Schematic of a quartz BRF plate. The optic axis ($\vec{c}$) was on the surface of the BRF plate. The angle between the projection of the incident beam on the surface of the BRF plate and the optic axis ($\vec{c}$) is called the tuning angle (α). The angle of incidence is the Brewster angle (ϕ_B). The BRF plate was rotated around its surface normal ($\vec{N}$). γ is the angle between the optic axis ($\vec{c}$) and the direction of the internal (refracted) ray.

Details of the working principle of a BRF plate were thoroughly explained and modeled by Naganuma et al. [6]. More details and simulations can be seen in Refs. [46, 47]. The angle notation used for simulations in this work is similar to Ref. [6]. Quartz is a positive uniaxial crystal with two principal refractive indices, namely ordinary (n_o) and extraordinary (n_e), and has a trigonal structure (α-SiO_2). The n_o and n_e refractive indices of the quartz plate were calculated using the Sellmeier equation [48]. Average refractive index $(n_o(\lambda)+n_e(\lambda))/2$ was used for Brewster angle $\phi_B(\lambda)$ calculation. The transmission of power can be adjusted by rotating the BRF plate around its surface normal ($\vec{N}$) by changing the tuning (or rotation) angle α defined in Fig. 3-2.

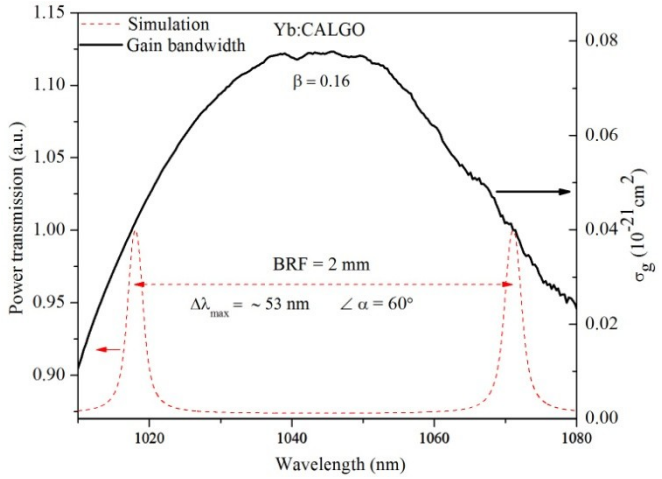

Fig. 3-3: Calculated power transmission of a 2 mm-thick BRF (left y-axis). Also shown is the gain cross-section (σ_g) spectrum of Yb:CALGO for σ-polarization [49] and population inversion ratio β of 0.16.

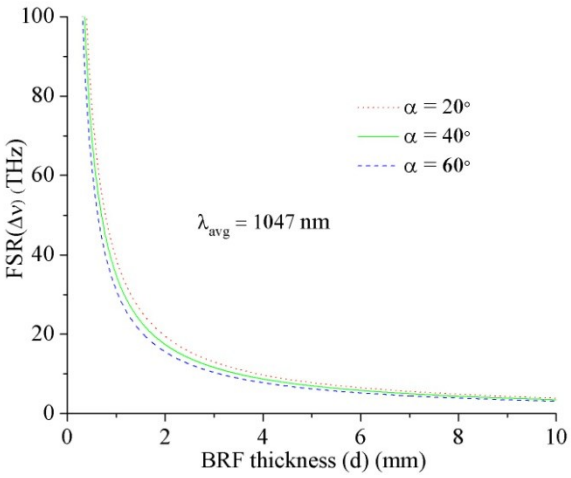

Fig. 3-4: Variation of FSR with respect to BRF thickness for different tuning angles (α = 20°, 40° and 60°)

The separation of the transmitted wavelengths can be determined using the equation 3.1 [46]:

$$\Delta\lambda = \frac{\lambda^2 sin\,\phi_B}{(n_e - n_o)d\,(1 - cos^2\alpha\,cos^2\,\phi_B)} \qquad 3.1$$

The free spectral range (FSR) of the BRF can be estimated following the equation 3.2 [50], where c is the velocity of light and d is the thickness of the BRF plate:

$$\Delta\upsilon_{FSR} = \frac{c\,sin\,\phi_B}{(n_e - n_o)d\,(1 - cos^2\alpha\,cos^2\,\phi_B)} \qquad 3.2$$

Fig. 3-4 emphasizes the fact that the tuning angle has a relatively small effect on FSR. The reason for this behaviour is that the optical axis is located on the surface plane of the BRF plate. However, the variation was more significant for thinner crystals as shown in Fig. 3-4. The average wavelength for all calculations was taken as 1047 nm. The variation in average wavelength also has little effect on $\Delta\lambda$. The estimated values of FSR for different BRF plate thickness are shown in Table 3-1.

Table 3-1: Calculated values of Δλ and FSR with respect to the BRF plate thickness for tuning angle $\alpha = 40^0$.

BRF plate	n_o	n_e	$n_e - n_o$	$\Delta\nu_{FSR}$ (THz)	$\Delta\lambda$ (nm)
2 mm	1.5343	1.5431	0.00875	17.4	63.6
4 mm				8.7	31.8
6 mm				5.8	21.2

3.3 **Results and discussion**

Initially a free-running operation was studied without using any intracavity BRF plates. In this regime, the output wavelength entirely depended on the output coupler. This can be explained by the quasi-three level nature of laser transitions which leads to the wavelength-dependent gain and loss [51]. The results are displayed in Fig. 3-5. The best performance was obtained for 10% OC.

After the measurements in the free-running regime, a BRF plate was introduced into one of the cavity arms (see Fig. 3-1). In this case beyond a certain level of pump power, the spectrum splits into two lines, giving rise to a dual-wavelength output. A typical example of the dual-wavelength result is shown in Fig. 3-6.

It was possible to switch between a single wavelength and dual-wavelength operation by varying the pump power. Fig. 3-6 shows the switching between the single and dual-wavelength regimes just by reducing the pump power. In this example, a combination of 6 mm-thick plate and 10% OC was used for the measurements. The dual-wavelength operation switched back to stable single wavelength regime when the absorbed pump power was lower than 8.1 W. Therefore, at low pump powers the laser operated in single wavelength and at high pump powers the laser operated in a dual-wavelength regime. In the range of pump powers between the 8.1 W and 9.8 W the laser was switching between the single and dual-wavelength regimes. The linewidths of both oscillating wavelengths for 6 mm-thick plate were measured to be no more

than 0.07 nm wide at half maximum. This measurement, however, was limited by the resolution of the used spectrometer. The recorded linewidth for a 2 mm-thick plate was broadened to 0.3 nm, as expected [6, 52]. By careful rotation of the plate the power ratio of the two generated wavelengths could also be adjusted.

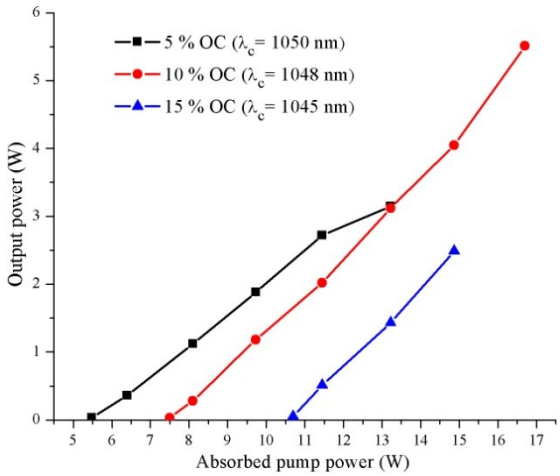

Fig. 3-5: Output power versus absorbed pump power for various output couplers (5%, 10% and 15%). λ_c is the central wavelength.

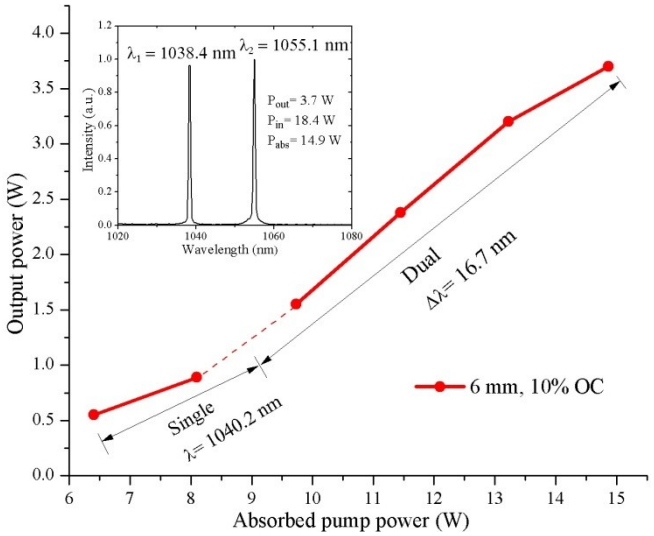

Fig. 3-6: Dual-wavelength measurements using 6 mm-thick BRF plate. Output power versus absorbed pump power: transition from a single-wavelength operation to dual-wavelength operation with 10% OC; measured dual-wavelength spectrum is shown in the inset.

The dual-wavelength experiment started with a 5% OC and 6 mm-thick BRF plate (Fig. 3-7). It was more likely to get dual-wavelength regime using a thick BRF plate and a low transmission output coupler. The laser with the 6 mm-thick plate generated an output power of 4.1 W at an absorbed pump power of 14.9 W. The wavelength separation in this case was 16.6 nm with two peaks at 1040.7 nm and 1057.3 nm. Next, the 6 mm-thick BRF plate was replaced by a 4 mm-thick one and the output power decreased to 2.95 W. In this case, in accordance with the theory, the dual-wavelength separation increased to 28.7 nm with peak wavelengths at 1033.3 nm and 1062.0 nm as shown in Fig. 3-7. As the BRF plate was replaced with a 2 mm-thick one,

the power further reduced to 1.41 W while the wavelength separation further increased to 47.1 nm with peak wavelengths of 1021.4 nm and 1068.5 nm. In all cases dual-wavelength operation could be achieved at specific rotation angles of the BRFs. For example, for the 2 mm-thick BRF plate with 5% OC, the dual-wavelengths were observed around discrete angles of 56° (FSR = 46.9 nm) and 126° (FSR = 47.1 nm). In all cases the polarization of both emission lines was the same (σ) and horizontal, i.e. set by the Brewster angle of incidence of BRFs.

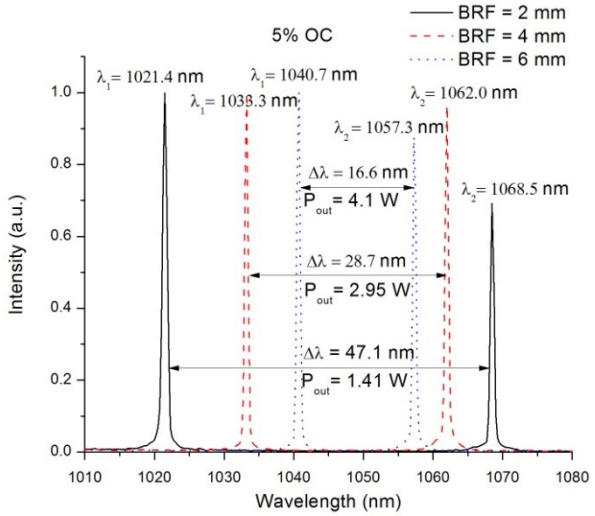

Fig. 3-7: Spectra of dual-wavelength operation for 5% OC using 2 mm, 4 mm and 6 mm-thick BRF plates.

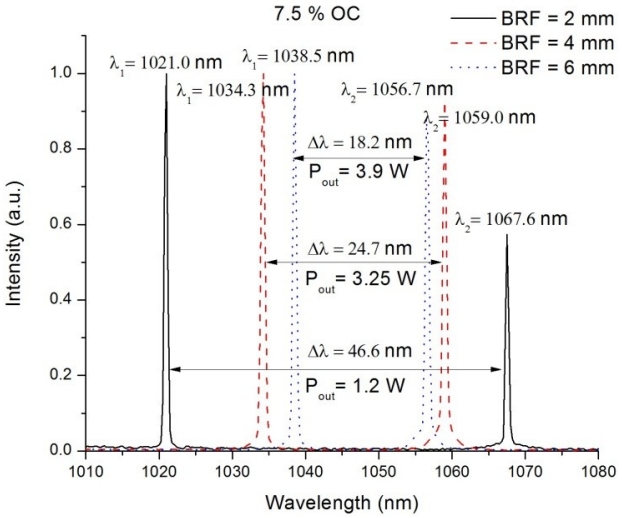

Fig. 3-8: Spectra of dual-wavelength operation for 7.5% OC using 2 mm, 4 mm and 6 mm-thick BRF plates.

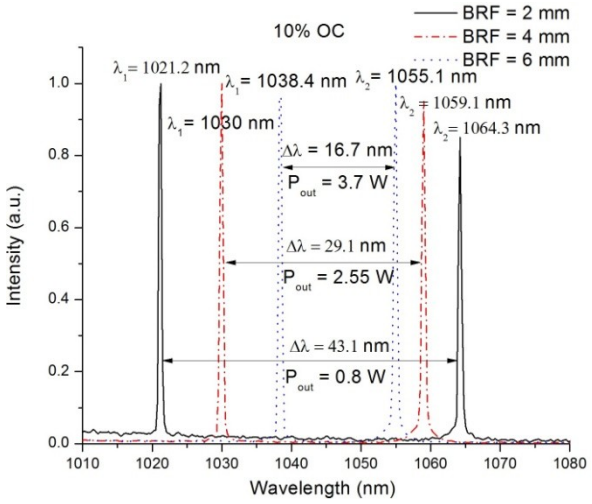

Fig. 3-9: Spectra of dual-wavelength operation for 10% OC using 2 mm, 4 mm and 6 mm-thick BRF

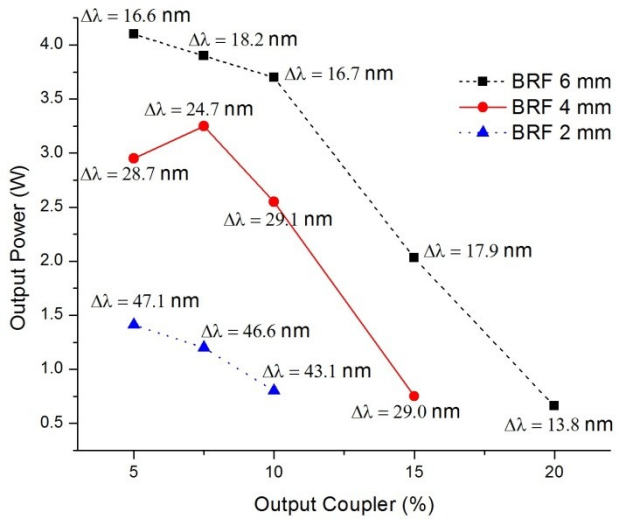

Fig. 3-10: Summary of dual-wavelength operation results for 2 mm, 4 mm and 6 mm BRF plates using

plates. different output couplers.

Similar experiments were repeated for 7.5% OC and 10% OC as shown in Fig. 3-8 and Fig. 3-9, respectively. The wavelength separation was increasing when thinner plates were used as in the previous case. However, the peak wavelengths were slightly different in all the cases. The mean emission wavelength was around 1047 nm. The results are summarized in Fig. 3-10. All of them were taken at a fixed absorbed pump power of 14.9 W. As can be seen, there is a relation between the maximum dual-wavelength output power and the plate thickness: the maximum dual wavelength output power scales with the plate thickness. This can be explained by the shape of the gain spectrum (see Fig. 3-3), i.e. the smaller FSR of a plate generates two wavelengths that are closer to the peak of the gain and vice versa.

The power ratio and stability of the two generated wavelengths was highly dependent on the intracavity power due to gain competition [37]. The power ratio fluctuations were more pronounced for thinner BRF plates and output couplers with higher transmission. For example, the power fluctuations observed for a thin BRF plate (2 mm) with higher output couplers (i.e. 7.5% OC and 10% OC) were up to 20% from the average value (i.e. at 1:1 power ratio), whereas the power fluctuations for a thick BRF plate (6 mm) with lower output coupler (i.e. 5%) were less than 5%. A possible explanation for this behavior is that for a 6 mm-thick BRF the observed dual-wavelength emission occurs in the relatively flat region of the gain spectrum closer to its peak, whereas for a 2-mm-thick BRF, the two emission lines are separated much wider and oscillate at the steeper and weaker regions of the gain spectrum. Therefore even a small variation in loss can induce a sudden fluctuation in the output power levels. The experiments were also conducted for 15% OC and 20% OC. However, as expected from decrease of the Yb:CALGO gain away from the central wavelength of ~1045 nm, it did not work for thinner BRF plates with

large FSRs as shown in the Fig. 3-10.

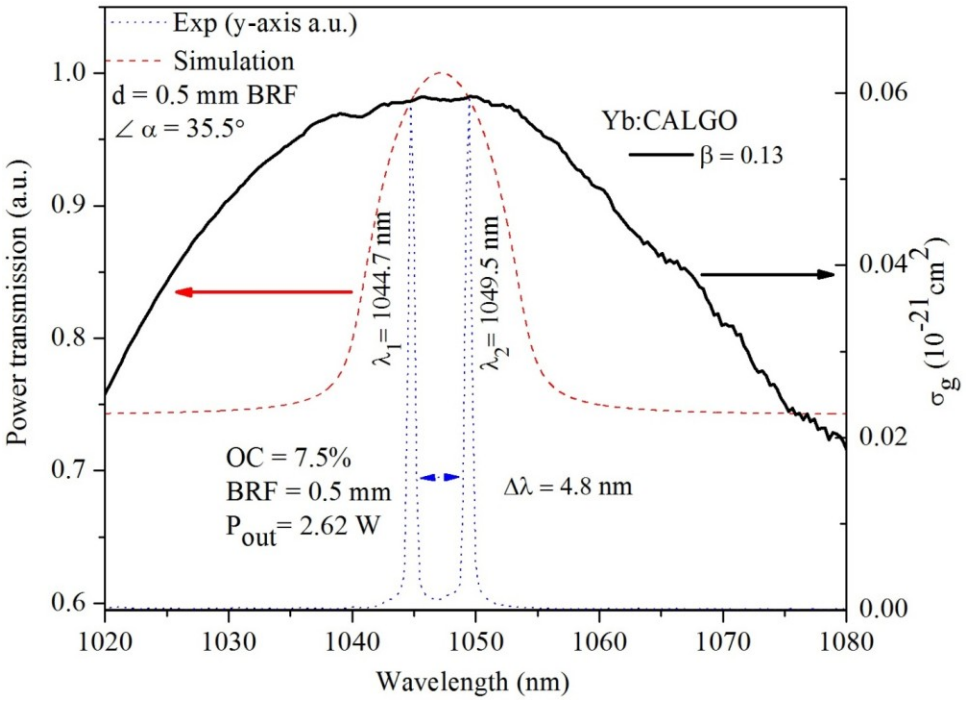

Fig. 3-11: Calculated power transmission of the 0.5 mm-thick BRF plate and measured dual-wavelength spectrum. Also shown is the gain cross-section spectrum of Yb:CALGO for σ-polarization and population inversion ratio β of 0.13.

The difference in FSR for a given BRF plate could be a result of the combined effect of gain dynamics and the tuning angle. We believe that the choice of the output coupler is the more influential factor for these small (2-3 nm) variations, because the output coupler determines the gain dynamics [51]. The tuning angle was only slightly adjusted to achieve a 1:1 power ratio.

The entire set of experiment was also conducted for a very thin BRF plate of 0.5 mm thickness. This thin BRF plate is suitable for single wavelength tuning because of large FSR. Single wavelength tuning results using different OCs are shown in Table 3-2. In this case the maximum power was observed in the middle of the tuning range. Surprisingly, we also got dual-wavelength operation that does not comply well with the theoretical values of FSR. More than

one dual-wavelength combinations were possible with 0.5 mm-thick plate by simple power adjustments (Table 3-2). A possible explanation of this behavior is that the fairly broad transmission window of the 0.5 mm-thick BRF plate in combination with a fairly flat gain of Yb:CALGO could support two narrowly separated peaks as shown in Fig. 3-11. In contrast to the regular operation of BRF where each generated wavelength is caused by one of its low loss transmission windows (see Fig. 3-11), in this case dual-wavelength regime was supported by a single transmission peak due to the mentioned peculiarities of the gain spectrum.

Table 3-2: Single wavelength tuning results using 0.5 mm-thick BRF plate.

OC	Single wavelength tuning (output power)	Single wavelength tuning range	Possible dual wavelength operations	Δλ (Δν)	Dual wavelength power
5 %	1043.3 nm (3.0 W) 1050.3 nm (4.1 W) 1056.0 nm (0.9 W)	1043.3 nm – 1056.0 nm (12.7 nm)	1) 1043.9 nm – 1048.8 nm 2) 1039.6 nm – 1048.9 nm	4.9 nm (1.34 THz) 9.3 nm (2.56 THz)	3.3 W 2.1 W
7.5%	1043.0 nm (3.3 W) 1047.5 nm (3.9 W) 1049.5 nm (2.5 W)	1043.3 nm – 1049.5 nm (6.2 nm)	1) 1044.7 nm – 1049.5 nm	4.8 nm (1.31 THz)	2.6 W
10 %	1043.0 nm (3.4 W) 1047.7 nm (3.7 W) 1052.0 nm (1.6 W)	1043.0 nm – 1052.7 nm (9.7 nm)	1) 1043.8 nm – 1048.5 nm	4.7 nm (1.29 THz)	3.3 W
15 %	1039.3 nm (2.0 W) 1045.0 nm (2.4 W) 1050.0 nm (1.1 W)	1039.3 nm – 1050.0 nm (10.7 nm)	1) 1039.7 nm – 1044.5 nm	4.8 nm (1.33 THz)	1.9 W
20 %	1039.6 nm (0.3 W) 1041.8 nm (0.5 W) 1042.3 nm (0.4 W)	1039.6 nm – 1042.3 nm (2.7 nm)	None	None	None

A brief comparison of similar works in the multi-watt regime using Yb:KGW laser is as follows: the maximum output power obtained for thermal lens driven simultaneous dual-wavelength operation of Yb:KGW laser was 4.6 W at a pump power of 26.8 W [34]. The FSR options were very limited in this experiment and polarization-switching was observed. Another

work on Yb:KGW utilizing the option of a single BRF plate produced a lower output power of 3.4 W at a pump power of 27.9 W [37]. The maximum possible dual-wavelength separation using BRF plate thickness was limited by the gain bandwidth of Yb:KGW. In this work a higher output power level was reported (4.1 W) with a much lower pump power of 18.4 W. In addition to the significantly wider discrete tunability of the possible frequency offset, the optical-to-optical efficiency (η_{o-o}) of this work was 22.3%, which is much higher than the η_{o-o} of the above mentioned Yb:KGW lasers (17.2% [34] and 12.2% [37]). This points out that Yb:CALGO is a more attractive choice than Yb:KGW for multi-watt dual-wavelength operation with widely tunable frequency offset.

3.4 **Conclusion**

A diode-pumped dual-wavelength Yb:CALGO laser was demonstrated based on the use of a single intracavity BRF plate. Four BRF plates of thickness 0.5 mm, 2 mm, 4 mm and 6 mm were tested in the experiments to produce discretely tunable separation of the generated wavelengths. An average wavelength separation for the 2 mm, 4 mm and 6 mm-thick plates was 45.6 nm ($\Delta\nu$ = 12.5 THz), 27.9 nm ($\Delta\nu$ =7.7 THz) and 16.64 nm ($\Delta\nu$ = 4.4 THz), respectively. The maximum output power of 4.1 W in dual-wavelength regime was observed for 6 mm-thick BRF plate using an optimized output coupler transmission of 5%. For the 0.5 mm-thick BRF plate a single-wavelength output and occasionally a closely separated dual-wavelength regimes were observed. The latter one can be explained by the broad transmission window of the BRF and the relatively flat gain spectrum of Yb:CALGO. We believe that the developed dual-wavelength Yb:CALGO laser with multi-watt output power is a suitable and cost effective candidate for dual-wavelength mode-locked lasers [53-55] and generation of THz radiation [56]. At the same time such lasers

can be attractive as a pump source for second harmonic generation or optical parametric oscillators in the visible and near-IR spectral ranges [57-61].

3.5 References

[1] S. Chang, Y. Mao, and C. Flueraru, "Dual-Source Swept-Source Optical Coherence Tomography Reconstructed on Integrated Spectrum," *International Journal of Optics,* vol. 2012, p. 6, 2012.

[2] R. Czarny, M. Alouini, C. Larat, M. Krakowski, and D. Dolfi, "THz-dual-frequency Yb^{3+}:$KGd(WO_4)_2$ laser for continuous wave THz generation through photomixing," *Electronics Letters,* vol. 40, pp. 942-943, 2004.

[3] S. Feng, O. Xu, S. Lu, X. Mao, T. Ning, and S. Jian, "Single-polarization, switchable dual-wavelength erbium-doped fiber laser with two polarization-maintaining fiber Bragg gratings," *Optics Express,* vol. 16, pp. 11830-11835, 2008.

[4] Y. Ji, J. Cao, J. Xu, Z. You, and C. Tu, "2.4 W highly efficient simultaneous dual-wavelength laser operation of monoclinic Yb^{3+}:$Ca_4LaO(BO_3)_3$ crystals," *Applied Optics,* vol. 53, pp. 5517-5521, 2014.

[5] A. Brenier, "Active Q-Switching of the Diode-Pumped Two-Frequency Yb^{3+}:$KGd(WO_4)_2$ Laser," *Quantum Electronics,* vol. 47, pp. 279-284, 2011.

[6] K. Naganuma, G. Lenz, and E. P. Ippen, "Variable bandwidth birefringent filter for stable femtosecond lasers," *Quantum Electronics, IEEE Journal of,* vol. 28, pp. 2142-2150, 1992.

[7] C. G. Trevino-Palacios, O. J. Zapata-Nava, E. V. Mejia-Uriarte, N. Qureshi, G. Paz-Martinez, and O. Kolokolstev, "Dual wavelength continuous wave laser using a birefringent filter," *Journal of the European optical society,* vol. 8, p. 5, 2013.

[8] S. Ghanbari and A. Major, "High power continuous-wave dual-wavelength alexandrite laser," *Laser Physics Letters,* vol. 14, p. 105001, 2017.

[9] U. Demirbas, R. Uecker, J. G. Fujimoto, and A. Leitenstorfer, "Multicolor lasers using birefringent filters: experimental demonstration with Cr:Nd:GSGG and Cr:LiSAF," *Optics Express,* vol. 25, pp. 2594-2607, 2017.

[10] T. Yerebakan, U. Demırbas, S. Eggert, R. Bertram, P. Reiche, and A. Leitenstorfer, "Red-diode-pumped Cr:Nd:GSGG laser: two-color mode-locked operation," *Journal of the Optical Society of America B,* vol. 34, pp. 1023-1032, 2017.

[11] T. Waritanant and A. Major, "Thermal lensing in Nd:YVO_4 laser with in-band pumping at 914 nm," *Applied Physics B,* vol. 122, p. 135, 2016.

[12] T. Waritanant and A. Major, "High efficiency passively mode-locked Nd:YVO_4 laser with direct in-band pumping at 914 nm," *Optics Express,* vol. 24, pp. 12851-12855, 2016.

[13] R. C. Talukder, Md. Z. E. Halim, T. Waritanant, and A. Major, "Multiwatt continuous wave Nd:KGW laser with hot-band diode pumping," *Optics Letters,* vol. 41, pp. 3810-3812, 2016.

[14] Md. Z. E. Halim, R. C. Talukder, T. Waritanant, and A. Major, "Passive mode locking of a Nd:KGW laser with hot-band diode pumping," *Laser Physics Letters,* vol. 13, p. 105003, 2016.

[15] G. Shayeganrad and L. Mashhadi, "Dual-wavelength CW diode-end-pumped a-cut Nd:YVO4 laser at 1064.5 and 1085.5 nm," *Applied Physics B,* vol. 111, pp. 189-194, 2013.

[16] T. Waritanant and A. Major, "Diode-pumped Nd:YVO_4 laser with discrete multi-wavelength tunability and high efficiency," *Optics Letters,* vol. 42, pp. 1149-1152, 2017.

[17] T. Waritanant and A. Major, "Discretely selectable multiwavelength operation of a semiconductor saturable absorber mirror mode-locked Nd:YVO_4 laser," *Optics Letters,* vol. 42, pp. 3331-3334, 2017.

[18] R. Moncorgé, B. Chambon, J. Y. Rivoire, N. Garnier, E. Descroix, P. Laporte*, et al.*, "Nd doped crystals for medical laser applications," *Optical Materials,* vol. 8, pp. 109-119, 1997.

[19] F. Brunner, G. J. Spühler, J. Aus der Au, L. Krainer, F. Morier-Genoud, and R. Paschotta, "Diode-pumped femtosecond Yb:$KGd(WO_4)_2$ laser with 1.1-W average power," *Optics Letters,* vol. 25, p. 3, 2000.

[20] A. Major, L. Giniunas, N. Langford, A. I. Ferguson, D. Burns, E. Bente*, et al.*, "Saturable Bragg reflector-based continuous-wave mode locking of Yb:$KGd(WO_4)_2$ laser," *Journal of Modern Optics,* vol. 49, pp. 787-793, 2002.

[21] H. Zhao and A. Major, "Megawatt peak power level sub-100 fs Yb:KGW oscillators," *Optics Express,* vol. 22, pp. 30425-30431, 2014.

[22] R. Akbari, H. Zhao, K. A. Fedorova, E. U. Rafailov, and A. Major, "Quantum-dot saturable absorber and Kerr-lens mode-locked Yb:KGW laser with > 450 kW of peak power," *Optics Letters,* vol. 41, pp. 3771-3774, 2016.

[23] R. Akbari, K. A. Fedorova, E. U. Rafailov, and A. Major, "Diode-pumped ultrafast Yb:KGW laser with 56 fs pulses and multi-100 kW peak power based on SESAM and Kerr-lens mode locking," *Applied Physics B,* vol. 123, p. 123, 2017.

[24] G. Machinet, P. Sevillano, F. Guichard, R. Dubrasquet, P. Camy, J. L. Doualan*, et al.*, "High-brightness fiber laser-pumped 68 fs- 2.3 W Kerr-lens mode-locked Yb:CaF_2 oscillator," *Optics Letters,* vol. 38, pp. 4008-4010, 2013.

[25] P. Sévillano, P. Georges, F. Druon, D. Descamps, and E. Cormier, "32-fs Kerr-lens mode-locked Yb:$CaGdAlO_4$ oscillator optically pumped by a bright fiber laser," *Optics Letters,* vol. 39, pp. 6001-6004, 2014.

[26] A. Major, R. Cisek, and V. Barzda, "Development of diode-pumped high average power continuous-wave and ultrashort pulse Yb:KGW lasers for nonlinear microscopy," *Proc. SPIE,* vol. 6108, p. 61080Y, 2006.

[27] D. Sandkuijl, R. Cisek, A. Major, and V. Barzda, "Differential microscopy for fluorescence-detected nonlinear absorption linear anisotropy based on a staggered two-beam femtosecond Yb:KGW oscillator," *Biomedical Optics Express,* vol. 1, pp. 895-901, 2010.

[28] I. P. Nikolakakos, A. Major, J. S. Aitchison, and P. W. E. Smith, "Broadband characterization of the nonlinear optical properties of common reference materials," *IEEE J. Sel. Top. Quantum Electron* vol. 10, pp. 1164-1170, 2004.

[29] A. Major, F. Yoshino, J. S. Aitchison, P. W. E. Smith, E. Sorokin, and I. T. Sorokina, "Ultrafast nonresonant third-order optical nonlinearities in ZnSe for photonic switching at telecom wavelengths," *Applied Physics Letters,* vol. 85, pp. 4606-4608, 2004.

[30] N. Prent, C. Green, C. Greenhalgh, R. Cisek, A. Major, B. Stewart*, et al.*, "Inter-myofilament dynamics of myocytes revealed by second harmonic generation microscopy," *Journal of Biomedical Optics,* vol. 13, pp. 0413181-0413187, 2008.

[31] J. Liu, H. Zhang, J. Wang, and V. Petrov, "Output-coupling-dependent polarization state of a continuous-wave Yb:$YCa_4O(BO_3)_3$ laser," *Optics Letters,* vol. 32, pp. 2909-2911, 2007.

[32] N. V. Kuleshov, A. A. Lagatsky, A. V. Podlipensky, V. P. Mikhailov, and G. Huber, "Pulsed laser operation of Yb-doped $KY(WO_4)_2$ and $KGd(WO_4)_2$," *Optics Letters,* vol. 22, p. 3, 1997.

[33] A. Brenier, "Tunable THz frequency difference from a diode-pumped dual-wavelength Yb 3+ :$KGd(WO_4)_2$ laser with chirped volume Bragg gratings," *Laser Physics Letters,* vol. 8, p. 520, 2011.

[34] H. Zhao and A. Major, "Orthogonally polarized dual-wavelength Yb:KGW laser induced by thermal lensing," *Applied Physics B,* vol. 122, pp. 163-169, 2016.

[35] P. Loiko, S. Manjooran, K. Yumashev, and A. Major, "Polarization anisotropy of thermal lens in Yb:KY(WO4)2 laser crystal under high-power diode pumping," *Applied Optics,* vol. 56, pp. 2937-2945, 2017.

[36] H. Zhao and A. Major, "A continuous wave Yb:KGW laser with polarization-independent pump absorption," *Laser Physics,* vol. 23, p. 095001, 2013.

[37] R. Akbari, H. Zhao, and A. Major, "High-power continuous-wave dual-wavelength operation of a diode-pumped Yb:KGW laser," *Optics Letters,* vol. 41, pp. 1601-1604, 2016.

[38] R. L. Aggarwal, D. J. Ripin, J. R. Ochoa, and T. Y. Fan, "Measurement of thermo-optic properties of $Y_3Al_5O_{12}$, $Lu_3Al_5O_{12}$, $YAlO_3$, $LiYF_4$, $LiLuF_4$, BaY_2F_8, $KGd(WO_4)_2$, and $KY(WO_4)_2$ laser crystals in the 80-300K temperature range," *Journal of Applied Physics,* vol. 98, p. 103514, 2005.

[39] F. Druon, F. Balembois, and P. Georges, "New laser crystals for the generation of ultrashort pulses," *Comptes Rendus Physique,* vol. 8, pp. 153-164, 2007.

[40] J. Petit, P. Goldner, and B. Viana, "Laser emission with low quantum defect in Yb:$CaGdAlO_4$," *Optics Letters,* vol. 30, pp. 1345-1347, 2005.

[41] P. Loiko, F. Druon, P. Georges, B. Viana, and K. Yumashev, "Thermo-optic characterization of Yb:$CaGdAlO_4$ laser crystal," *Optical Materials Express,* vol. 4, pp. 2241-2249, 2014.

[42] F. Druon, M. Olivier, A. Jaffres, P. Loiseau, N. Aubry, J. DidierJean*, et al.*, "Magic mode switching in Yb:$CaGdAlO_4$ laser under high pump power," *Optics Letters,* vol. 38, pp. 4138-4141, 2013.

[43] S. Manjooran and A. Major, "Generation of Sub-50 fs Pulses With >1.5 MW of Peak Power From a Diode-Pumped Yb:CALGO Laser Oscillator," in *Conference on Lasers and Electro-Optics*, San Jose, California, 2016, p. JTu5A.82.

[44] P. Loiko, J. M. Serres, X. Mateos, X. Xu, J. Xu, V. Jambunathan*, et al.*, "Microchip Yb:$CaLnAlO_4$ lasers with up to 91% slope efficiency," *Opt. Lett.,* vol. 42, pp. 2431-2434, 2017.

[45] H. Mirzaeian, S. Manjooran, and A. Major, "A simple technique for accuarte characterization of thermal lens in solid state lasers," *Proc. SPIE,* vol. 9288, p. 928802, 2014.
[46] S. Zhu, "Birefringent filter with tilted optic axis for tuning dye lasers: theory and design," *Applied Optics,* vol. 29, pp. 410-415, 1990.
[47] B. Stormont, A. J. Kemp, I. G. Cormack, B. Agate, C. T. A. Brown, W. Sibbett*, et al.*, "Broad tunability from a compact, low-threshold Cr:LiSAF laser incorporating an improved birefringent filter and multiple-cavity Gires-Tournois interferometer mirrors," *Journal of the Optical Society of America B,* vol. 22, pp. 1236-1243, 2005.
[48] G. Ghosh, "Dispersion-equation coefficients for the refractive index and birefringence of calcite and quartz crystals," *Optics Communications,* vol. 163, p. 8, 1999.
[49] P. Loiko, J. M. Serres, X. Mateos, X. Xu, J. Xu, V. Jambunathan*, et al.*, "Microchip Yb:CaLnAlO4 lasers with up to 91% slope efficiency," *Optics Letters,* vol. 42, pp. 2431-2434, 2017.
[50] O. Svelto, *Principles of Lasers*, 5 ed.: Springer Science, 2010.
[51] H. Zhao and A. Major, "Dynamic characterization of intracavity losses in broadband quasi-three-level lasers," *Opt. Express,* vol. 22, pp. 26651-26658, 2014.
[52] S. Manjooran, P. Loiko, and A. Major, "Dual-wavelength Yb:CALGO laser with 1.31 THz frequency offset," presented at the SPIE Photonics West, San Francisco, California, United States, 2018.
[53] H. Yoshioka, S. Nakamura, T. Ogawa, and S. Wada, "Dual-wavelength mode-locked Yb:YAG ceramic laser in single cavity," *Optics Express,* vol. 18, pp. 1479-1486, 2010.
[54] Q. Yang, Y. G. Wang, D. H. Liu, J. Liu, L. H. Zheng, L. B. Su*, et al.*, "Dual-wavelength mode-locked Yb:$LuYSiO_5$ laser with a double-walled carbon nanotube saturable absorber," *Laser Physics Letters,* vol. 9, pp. 135-140, 2012.
[55] W. Z. Zhuang, M. T. Chang, K. W. Su, K. F. Huang, and Y. F. Chen, "High-power terahertz optical pulse generation with a dual-wavelength harmonically mode-locked Yb:YAG laser," *Laser Physics,* vol. 23, p. 075803, 2013.
[56] M. Scheller, J. M. Yarborough, J. V. Moloney, M. Fallahi, M. Koch, and S. W. Koch, "Room temperature continuous wave milliwatt terahertz source," *Optics Express,* vol. 18, pp. 27112-27117, 2010.
[57] S. Manjooran, H. Zhao, I. T. Lima, Jr., and A. Major, "Phase-matching properties of PPKTP, MgO:PPSLT and MgO:PPcLN for ultrafast optical parametric oscillation in the visible and near-infrared ranges with green pump," *Laser Physics,* vol. 22, pp. 1325-1330, 2012.
[58] H. Zhao, I. T. Lima, and A. Major, "Near-infrared properties of periodically poled $KTiOPO_4$ and stoichiometric MgO-doped $LiTaO_3$ crystals for high power optical parametric oscillation with femtosecond pulses," *Laser Physics,* vol. 20, pp. 1404-1409, 2010.
[59] I. T. Lima Jr., V. Kultavewuti, and A. Major, "Phasematching properties of congruent MgO-doped and undoped periodically poled $LiNbO_3$ for optical parametric oscillation with ultrafast excitation at 1 μm," *Laser Physics,* vol. 20, pp. 270-275, 2010.
[60] R. Akbari and A. Major, "Optical, spectral and phase-matching properties of BIBO, BBO and LBO crystals for optical parametric oscillation in the visible and near-infrared wavelength ranges," *Laser Physics,* vol. 23, p. 035401, 2013.

[61] A. Major, D. Sandkuijl, and V. Barzda, "Efficient frequency doubling of a femtosecond Yb:KGW laser in a BiB_3O_6 crystal," *Optics Express,* vol. 17, pp. 12039-12042, 2009.

Chapter 4: Intense short pulse lasers

4.1 Introduction and preview

This chapter deals with the most important objective of the initial thesis proposal of intense ultrashort pulse laser design and development. From the previous two chapters it was seen that Yb:CALGO could generate multi-watt output power and at the same time it could operate in a broad wavelength range of ~70 nm. This chapter explains how this broad gain bandwidth was utilized for the development of multi-watt ultrashort pulse laser. The design and development of two intense ultrashort pulse lasers using slightly different technologies are presented. The average output power, pulse duration, their repetition frequency, pulse train, beam quality and beam profile were recorded for each of these two developed lasers and the results were published in relevant journals.

Short pulse Yb-doped bulk lasers are widely used in efficient high harmonics generation [1], Raman spectroscopy [2], continuum generation [3] and optical parametric oscillators [4]. The shortest pulses achieved using Yb:CALGO crystal were 32 fs [5]. However, this was achieved using high beam quality fiber laser pumping. Similar pulse duration of 33 fs was achieved using Yb:CYA crystal using diode pumping [6]. The peak power was only 9.5 kW in that case. There are only a few works that attained high peak power (>100 kW) operation in sub-100-fs regime. One way to produce such pulses is to use a thin disk geometry [7, 8]. In the case of bulk crystals, H. Zhao *et al.* [9] and A. Greborio *et al.* [10] managed to generate 85 fs and 94 fs pulses with MW peak power using Yb:KGW and Yb:CALGO crystals, respectively. This chapter discusses the design and development of two Yb:CALGO short pulse lasers, namely,

KLAS laser and KLM laser. KLAS laser utilizes a combination of a nonlinear technique called Kerr-lens mode locking and a semiconductor saturable absorber mirror to generate ultrashort pulses, whereas KLM laser uses pure nonlinear Kerr effect.

The two most common techniques to generate short laser pulses are Q-switching and mode locking. The main limitation of Q-switching is that the pulse duration will be always longer than the cavity round-trip time. Q-switching can generate only pulses as short as a few picoseconds (ps). Therefore, the most common technique to generate femtosecond (fs) pulses is mode locking. Detaiedl analysis of Q-switching is outside the scope of this report. However, sometimes Q-switching can interfere with mode locking and results in a modulated pulse train. This process is called Q-switched mode locking and Q-switching instabilities [11] are generally considered as an unwanted effect. The different operation regimes of a laser are shown in Fig. 4-1.

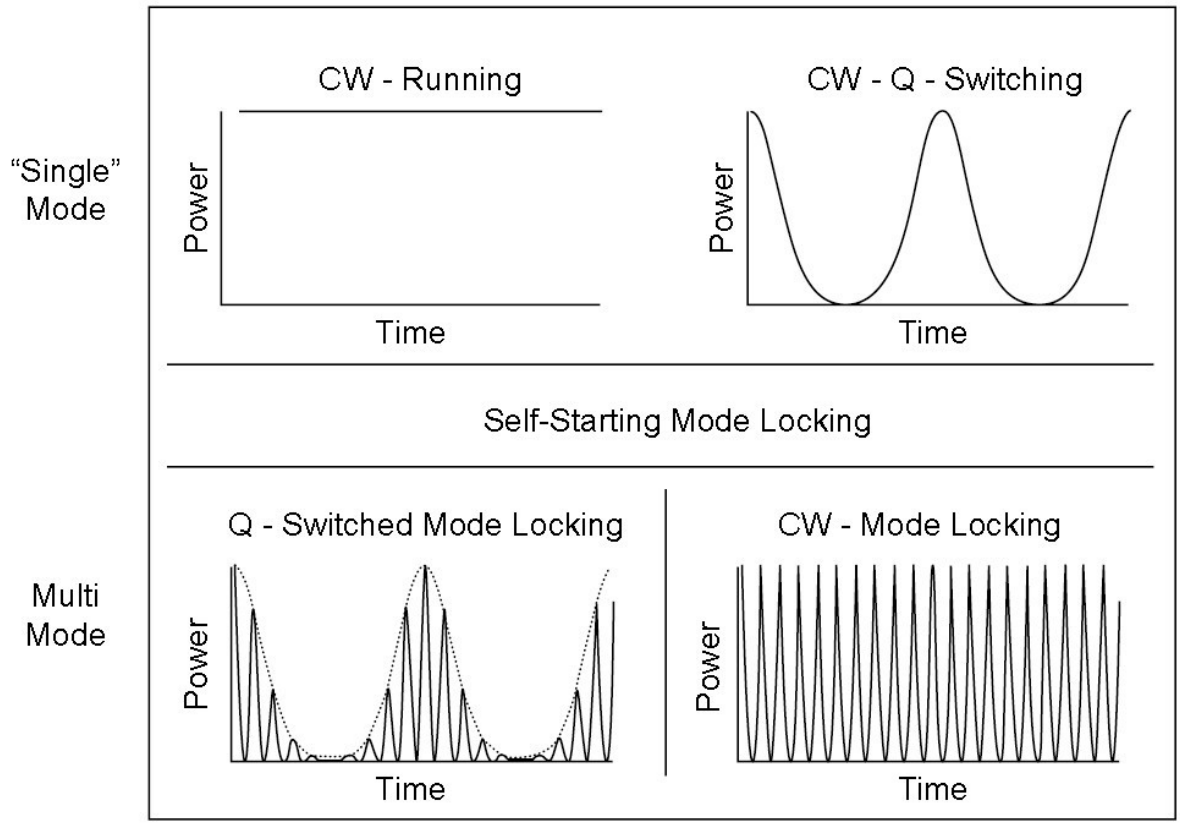

Fig. 4-1: Different regimes of laser operation [11].

Yb:CALGO has the advantage of high nonlinear refractive index ($n_2 = 9\times10^{-20}$ m^2/W^2) [12]. As mentioned earlier, it has broad gain bandwidth and high thermal conductivity. All these factors contributed to the development of the high peak power lasers in this thesis.

4.2 **Pulse propagation**

At a given point in space, the complex electric field of a short laser pulse is defined as Eq. 4.1, where ω_0 is the frequency of the field, A(t) is the pulse envelope and E(t) is the fast oscillating electric field. If the pulse is Gaussian in shape, it can be represented as Eq.4.2, where Γ can be a complex number. Another important pulse shape is the $sech^2$ pulse (Eq.4.3), where τ_0 denotes the temporal half-width.

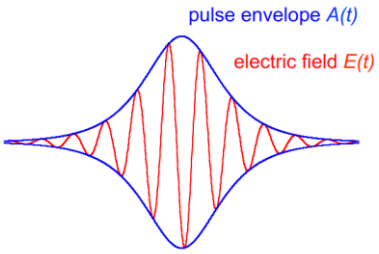

Fig. 4-2: A short light pulse

Pulse shape	$E(t) = A(t)e^{i\omega_0 t}$	4.1
Gaussian	$E(t) = e^{-\Gamma t^2} e^{i\omega_0 t}$	4.2
Sech^2	$E(t) = \text{sech}\left(\frac{t}{\tau_0}\right) e^{i\omega_0 t}$	4.3

4.2.1 Dispersive pulse broadening

Dispersion is the phenomenon in which the phase velocity of a light wave in the material depends on its frequency. For ultrashort pulsed light the dispersion effect is very common and this will result in the temporal spreading of the pulse. For most of the materials the refractive index decreases with increasing wavelength, i.e. $dn/d\lambda < 0$. In this case the medium is said to have normal dispersion. If the refractive index increases with increasing wavelength, the medium is said to have anomalous dispersion.

The light pulse corresponds to a plane wave multiplied by the time-shifted envelope. The plane wave propagates in a medium with a phase velocity, υ_p, given by Eq. 4.4.

$$v_p(\omega_0) = \frac{\omega_0}{k(\omega_0)} = \frac{c}{n_p(\omega_0)} \tag{4.4}$$

where c is the velocity of light in vacuum and n_p is the refractive (phase) index of the medium. The pulse envelope propagates at the so called group velocity, v_g, given by Eq. 4.5.

$$v_g(\omega_0) = \left(\frac{d\omega}{dk}\right)_{\omega_0} = \frac{c}{n_g(\omega_0)} \tag{4.5}$$

where n_g is the group index. A relationship between the phase and group indexes can be found using the dispersion relation and its derivative with respect to frequency:

$$k(\omega) = \frac{\omega}{c} n_p(\omega) \tag{4.6}$$

where the wave number k(ω) is real if the medium is non-absorbing. Taking the derivative of Eq. 4.6 will give Eq. 4.7.

$$k'(\omega) = \frac{dk}{d\omega} = \frac{n_p(\omega)}{c} + \frac{\omega}{c}\frac{dn_p(\omega)}{d\omega} \tag{4.7}$$

Substituting Eq. 4.5 in Eq. 4.6 and rearranging it will give Eq. 4.8.

$$n_g = n_p + \omega\frac{dn_p}{d\omega} = n_p - \lambda\frac{dn_p}{d\lambda} \tag{4.8}$$

Since all materials are dispersive, $n_g \neq n_p$, the envelope propagates at a different velocity than the plane wave, i.e., $v_g \neq v_p$.

If the wave number varies slowly with ω, we can expand it in a Taylor series around ω_0 (Eq. 4.9).

$$\begin{aligned} k(\omega) &= k(\omega_0) + \left(\frac{dk}{d\omega}\right)_{\omega_0}(\omega - \omega_0) + \frac{1}{2}\left(\frac{d^2k}{d\omega^2}\right)(\omega - \omega_0)^2 + \cdots \\ &= k(\omega_0) + k'(\omega_0)\Delta\omega + \frac{1}{2}k''(\omega_0)\Delta\omega^2 + \ldots \end{aligned} \tag{4.9}$$

After propagating a distance z in the medium, the field acquires a spectral phase given by Eq. 4.10.

$$\phi(\omega) = k(\omega)z \tag{4.10}$$

Substituting Eq. 4.10 in Eq. 4.9 gives Eq. 4.11.

$$\begin{aligned} \phi(\omega) &= \varphi(\omega_0) + \left(\frac{d\phi}{d\omega}\right)_{\omega_0}(\omega - \omega_0) + \frac{1}{2}\left(\frac{d^2\phi}{d\omega^2}\right)(\omega - \omega_0)^2 + \cdots \\ &= \varphi(\omega_0) + \phi'(\omega_0)\Delta\omega + \frac{1}{2}\phi''(\omega_0)\Delta\omega^2 + \ldots \end{aligned} \tag{4.11}$$

Each of these terms has an effect on the temporal shape of the pulse and gets a name according to the effect it produces (Table 4-1).

Table 4-1: Higher order dispersions

Dispersion	**Phase term**	**Equation**
Phase Velocity, v_p	$\frac{\omega}{k_n}$	$\frac{c}{n}$
Group Velocity, v_g	$\frac{d\omega}{dk_n}$	$\frac{c}{n}\frac{1}{1-\frac{dn}{d\lambda}\frac{\lambda}{n}}$
Group Delay, T_g	$T_g = \frac{z}{v_g} = \frac{d\phi}{d\omega}, \phi \equiv k_n z$	$\frac{nz}{c}\left(\frac{1}{1-\frac{dn}{d\lambda}\frac{\lambda}{n}}\right)$
Dispersion: 1st Order	$\frac{d\phi}{d\omega}$	$\frac{nz}{c}\left(\frac{1}{1-\frac{dn}{d\lambda}\frac{\lambda}{n}}\right)$
Dispersion: 2nd Order	$\frac{d^2\phi}{d\omega^2}$	$\frac{\lambda^3 z}{2\pi c^2}\frac{d^2 n}{d\lambda^2}$
Dispersion: 3rd Order	$\frac{d^3\phi}{d\omega^3}$	$\frac{-\lambda^4 z}{4\pi^2 c^3}\left(3\frac{d^2 n}{d\lambda^2}+\lambda\frac{d^3 n}{d\lambda^3}\right)$

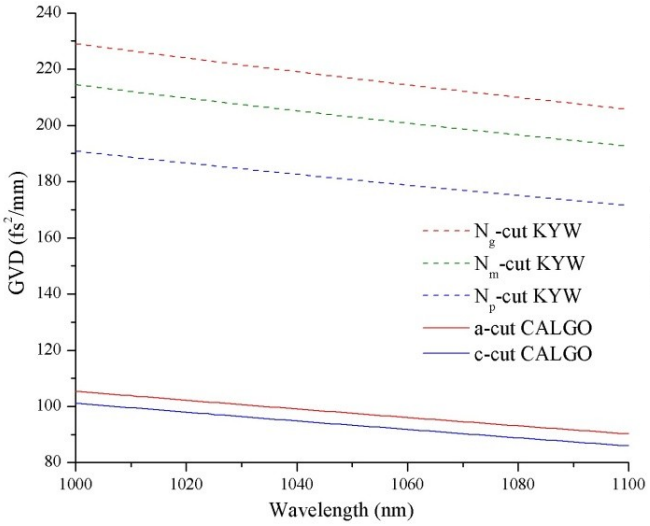

Fig. 4-3: Calculated GVD for KYW and CALGO.

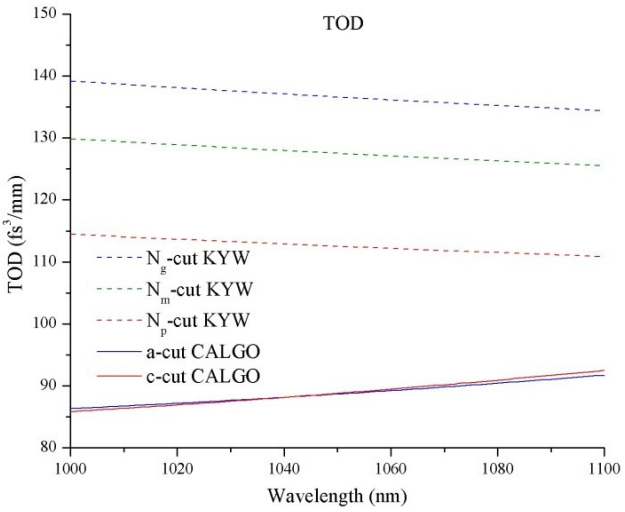

Fig. 4-4: Calculated TOD for KYW and CALGO.

The first order phase produces a time delay in the pulse envelope. Group delay dispersion (GDD) and third order dispersion (TOD) temporally deforms the pulse. The phase shift due to TOD can be calculated using the equation

$$\Delta\phi = \frac{1}{6} L \times TOD \times \Delta\omega \qquad 4.12$$

For the shortest pulse of 38 fs that were generated in this thesis, the calculated phase shift due to TOD was approximately 0.024 rad. This phase shift was negligible compared to π rad. Therefore the TOD and higher order dispersion effects were neglected in this thesis.

4.2.1.1 Dispersion compensation

One of the major challenges in generation of high peak power ultrashort pulses is dispersion compensation. Traditionally, prism pairs were used for this purposes, however they have the disadvantage of high amount of power loss and high third order nonlinear effects. In all cases intracavity dispersion compensation was achieved using only chirped mirrors and no extracavity pulse compression was employed. Mirror coatings have been developed which can provide tailored GDD and TOD compensation. These are designed as multiple dielectric stacks of

varying thicknesses. These dielectric stacks reflect each wavelength from a different depth through the dielectric coating thus providing the required negative dispersion. However, precise dispersion compensation using chirped mirrors was a tedious task.

4.2.2 Self-phase modulation

The Kerr effect introduces not only a spatial dependence but also a temporal dependence on refractive index (Eq. 4.13) [13] .

$$n(r,t) = n + n_2 I(r,t) \tag{4.13}$$

The nonlinear refractive index produces a nonlinear phase shift during pulse propagation (Eq. 4.14).

$$\begin{aligned} \emptyset(z,r,t) &= -kn(r,t)z = -k[n + n_2 I(r,t)]z \\ &= -knz - \delta|A(r,t)|^2 \end{aligned} \tag{4.14}$$

where δ is the self-phase modulation (SPM) coefficient defined as

$$\delta = kn_2 z. \tag{4.15}$$

The change in pulse envelope due to SPM is approximated as Eq. 4.16.

$$\Delta A \approx -i\delta|A|^2 A \tag{4.16}$$

4.3 Mode locking theory

In the thesis only two passive mode locking techniques, namely, semiconductor saturable absorber mirror (SESAM) mode locking and Kerr-lens mode locking (KLM), are discussed. A combination of these two techniques, SESAM and KLM, is used in the design of our laser oscillators. In passive mode locking a nonlinear device such as a saturable absorber or a Kerr medium is used to generate ultrashort pulses. A saturable absorber can be either a fast saturable absorber or a slow saturable absorber. If the cavity pulses are longer than the absorber recovery

time, then it is called a fast saturable absorber. A fast saturable absorber can produce short pulses of the order of the absorber recovery time. The shortest absorber recovery time is few femtoseconds. If the cavity pulses are shorter than the absorber recovery time, then it is called a slow saturable absorber.

4.3.1 Semiconductor saturable absorber mirror (SESAM)

A saturable absorber is a material that has decreasing light absorption with increasing light intensity or in other words a saturable absorber transmits light at high intensity. Saturable absorber mode locking is also called loss modulation because it introduces periodic losses into the cavity. The peak of the laser pulse has more intensity and it saturates the absorber more than the wings of the pulse, which has low intensity. Therefore the saturable absorber only allows central high intensity region of the pulse to oscillate and attenuates the low intensity wing regions thereby reducing the pulse duration in time domain. A typical semiconductor saturable absorber mirror (SESAM) incorporates a Bragg mirror structure and a quantum well saturable absorber. Such absorber works in reflection regime.

The working principle of SESAM was explained in detail by U. Keller *et al.* in [14] (see Fig. 4-5). A semiconductor absorber absorbs light when the photon energy is sufficient to excite carriers from the valence band to the conduction band. At strong excitation, the absorption gets saturated because initial states of the pump transition are depleted while the final states are partially occupied. Therefore the SESAM only permits high intensity pulses to oscillate in the laser cavity and prevents the CW operation of the laser.

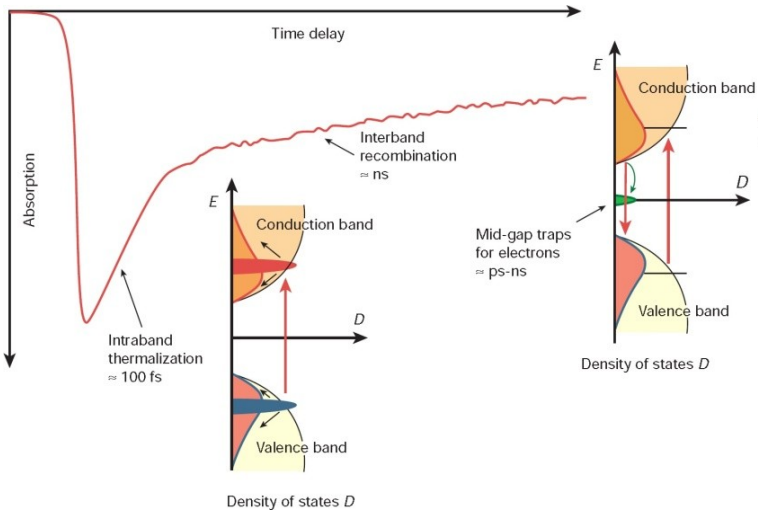

Fig. 4-5: SESAM working principle explained in [14]. Copyright © 2003, Springer Nature.

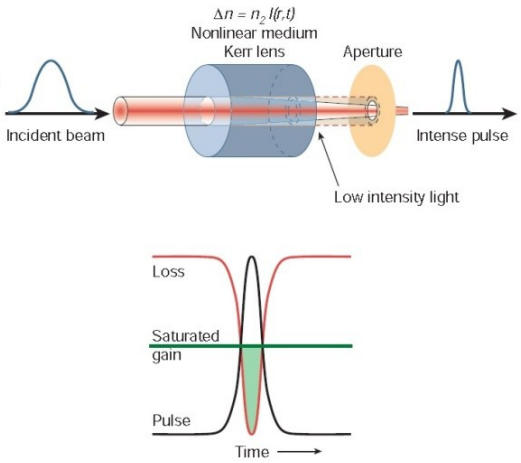

Fig.4-6: KLM working principle explained in [14]. Copyright © 2003, Springer Nature.

4.3.2 Kerr-lens mode locking (KLM)

The principle of Kerr-lens mode locking (KLM) is based on optical Kerr effect. The Kerr effect is directly proportional to the square of the electric field (where $|E|^2 = I$ is the intensity of light) and this leads to an intensity dependent refractive index in the material. Due to transverse Gaussian or $Sech^2$ profile of the pulse, the Kerr-lens will be stronger at the center and weaker at the wings of the pulse and this will produce an intensity dependent nonlinear lens. This will focus the laser pulse and this effect is called self-focusing. The formed lens is called Kerr-lens. The Kerr-lens is only formed when the intensity of the light is high or in other words Kerr-lens is only formed in the pulsed mode of operation. The CW laser is not intense enough to induce an optical Kerr effect. This mechanism of focusing the high intensity mode-locked pulses has been utilized for Kerr-lens mode locking. By introducing an aperture into the laser cavity most of the weak intensity pulses and CW radiation can be filtered out or attenuated. This is called hard aperture KLM. A hard aperture KLM is shown in Fig.4-6 [14]. In this laser chapter, the laser cavity was designed in such a way that the gain medium itself acted like an aperture and

attenuated the CW operation. The design of the cavity was such that the laser gain was higher in the presence of an intensity dependent nonlinear Kerr-lens. This was achieved through the Kerr lens induced better cavity mode overlap with the pumped volume in the crystal. The laser operated close to the cavity stability edge. This lensing effect would make the laser unstable in the CW mode of operation. This method is generally known as a soft aperture KLM.

4.3.3 Time-bandwidth product

Time-bandwidth product is the product of the measured pulse duration and the spectral width of the pulse at FWHM. Time-bandwidth product indicates how close the pulse duration is to the limit set by its spectral width. If there are N longitudinal modes locked with a frequency separation of $\Delta\omega$, the overall mode-locked bandwidth is $N\Delta\omega$, and the wider this bandwidth, the shorter is the pulse duration. The relationship between the mode-locked bandwidth and the pulse duration is given by a time-bandwidth product. The product of mode-locked bandwidth and the minimum possible pulse duration will be a constant (Eq. 4.17).

$$N\Delta\omega \times \Delta t = K \tag{4.17}$$

The minimum possible pulse duration is determined by the Fourier transform limit. For example, it is ~0.315 for the transform-limited $Sech^2$- shaped pulses or ~0.441 for Gaussian-shaped pulses. This means that for a given spectral width, there is a lower limit for the pulse duration. This limitation is a property of the Fourier transform. For ultrashort lasers, pulses with hyperbolic secant temporal shape are used. Therefore, all our calculations to find pulse duration used hyperbolic secant function. Corresponding values and equations are shown in Table 4-2.

Table 4-2: Values of the time-bandwidth constants for Gaussian and $Sech^2$ functions.

Function	E(t)	K
Gaussian	$e^{-(t/t_0)^2/2}$	0.441

Hyperbolic Secant	$1/\cosh(t/t_0)$	0.315

4.4 Mode-locked laser design

The pump beam was imaged into the gain medium with the help of 50 mm and 75 mm focal length lenses, resulting in a spot size radius of about 85 μm. The design was influenced by a paper published by G.Holtom *et al*. [15] and similar technique was used by H. Zhao *et al*. [16] to produce high peak power laser pulses. In this method, a movable mirror on a translation stage was used to adjust the beam size inside the laser crystal. When the beam size was increased, at some point the laser suddenly jumps from the continuous wave regime to the mode-locked (ML) regime. H. Zhao *et al*. observed a multi-pulsing regime in between and we also observed multi-pulsing occasionally.

4.4.1 Design 1. Ultra short pulse KLAS laser with 42.3 MHz repetition rate

In this case mode locking was achieved using Kerr-lens and SESAM mode locking (KLAS) [16]. SESAM helps to start the mode locking process and KLM helps to increase the modulation depth. Fig. 4-7 shows the laser cavity designed for mode locking based on the dual action of Kerr lensing and saturable absorber, KLAS [3,5].

The exact role of KLM and SESAM was unknown in the KLAS design. However, some assumptions were made about the working principle of KLAS ML. It was observed that the ML process was started by SESAM and it is believed that KLM helped to shorten the pulse duration. Many studies showed that the laser can continue to work in the ML regime even if the SESAM was removed after starting the ML process. Different terms were used to denote this ML process depending on the influence of SESAM (eg. SESAM assisted ML, etc.) (see Fig. 4-7). However, in our case ML could be achieved only when both SESAM and KLM were present in the cavity.

Therefore, it is believed that both SESAM and KLM had almost equal influence in the ML process. A comparison of the SESAM and KLM ML techniques is shown in Table 4-3.

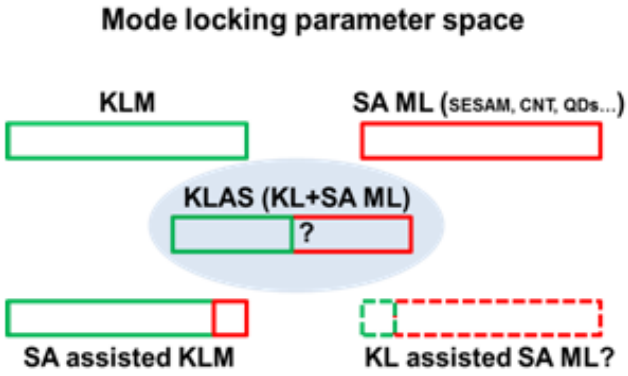

Fig. 4-7: ML parameter space for KLM and SESAM. SA – saturable absorber, KL – Kerr-lens. (Courtesy R. Akbari)

Table 4-3: Comparison: SESAM and KLM

Properties	SESAM	KLM
Fast recovery	×	✓
Broadband operation	×	✓
Large beam size	✓	×
Center of cavity stability region	✓	×
Self-starting	✓	×

To achieve a precise control of the fluence (pulse energy per spot area) on the SESAM, one of the laser arms was collimated and then a telescopic mirror arrangement was introduced to adjust the beam spot size on it. The beam radius of the laser mode in the gain medium was controlled by changing the distance (TR) from 255 mm to 275 mm. A SESAM with modulation depth of 1.4% initiated the mode locking process which was accompanied by a soft aperture KLM [9]. The total length of the cavity was about 3.56 m (see Fig. 4-8) which corresponds to a repetition rate of 42.3 MHz. The corresponding variation in beam radius from the SESAM to the OC is shown in Fig 4-9. A combination of negative dispersion (GTI) mirrors with discrete values of -100 fs^2, 250 fs^2, 550 fs^2 and -1300 fs^2 (Layertec) was used for dispersion compensation.

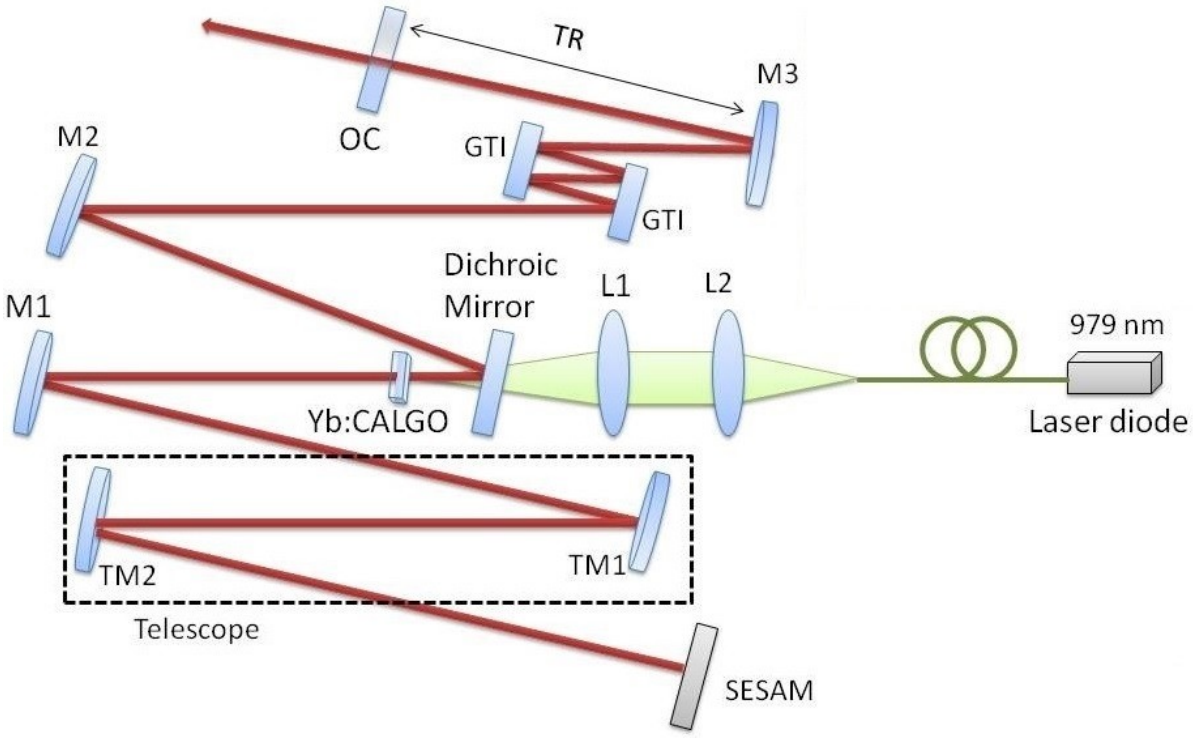

Fig. 4-8: KLAS laser setup. The curved mirrors: M1= 750 mm, M2= 600 mm and M3 = 500mm. GTI: chirped mirrors. Telescopic mirrors, TM1= 2000 mm and TM2 = 600 mm.

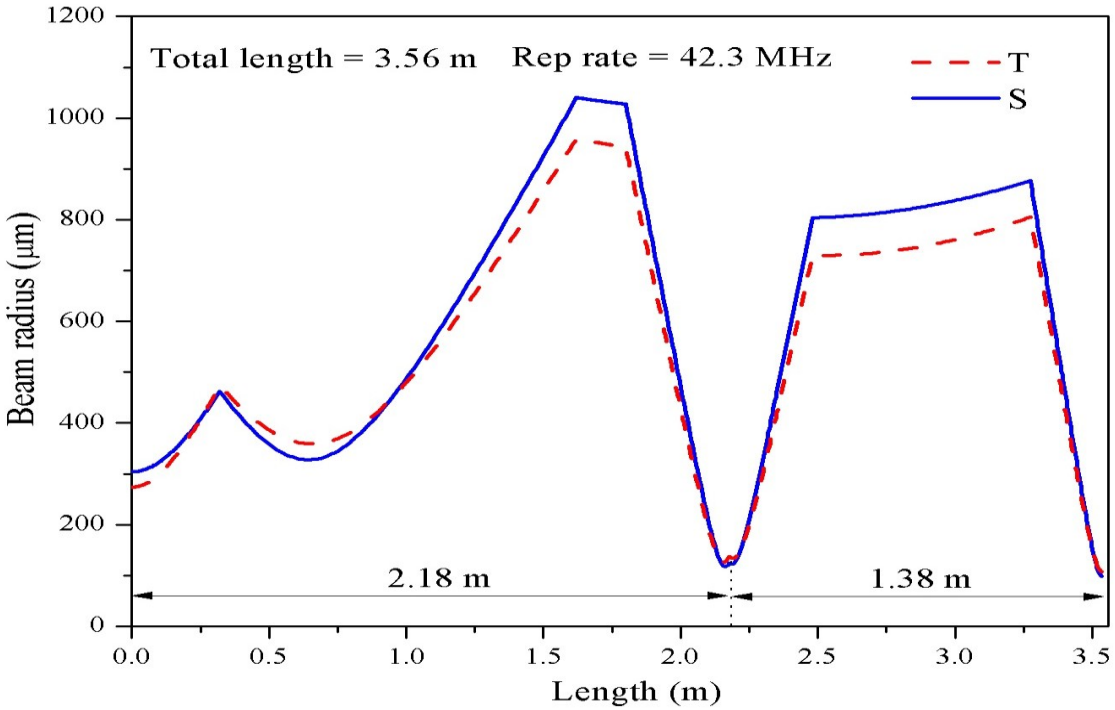

Fig 4-9: Beam radius of KLAS laser along the cavity. The long arm was about 2.18 m and the short arm was about 1.38 m long. Dotted line denotes the tangential plane and solid line denotes the sagittal plane.

4.4.1.1 Results and discussion (KLAS laser)

Initially, the laser was tested in continuous-wave regime. The best results were obtained using 10% OC. An HR mirror was used in place of the SESAM to obtain the CW results. For the input pump power of 20.4 W the crystal absorbed 16.7 W under non-lasing conditions. The CW output power at this incident pump power was 7.2 W.

After CW regime the SESAM was introduced into the cavity to initiate the mode locking process. The mode locking was self-starting with the introduction of SESAM. All the measurements in this experiment were taken by adjusting only four parameters: 1) output coupler transmission; 2) negative intracavity dispersion; 3) arm length (TR) (see Fig. 4-8); and 4) incident pump power. The ML experiments were conducted using 2.5, 5, 10 and 15% output

couplers (OC). The shortest pulses obtained for above OC's are 38 fs, 39 fs, 43 fs and 45 fs, respectively.

The pulses were initially monitored using a combination of a fast photodiode (Thorlabs DET08CFC, rise time < 70 ps) and oscilloscope (6 GHz, Tektronix TDS 6604) as shown in Fig. 4-10. Tthe top pulse train is shown on the 80 ns /div scale and the bottom pulse train is shown on the 1 ms/div scale.

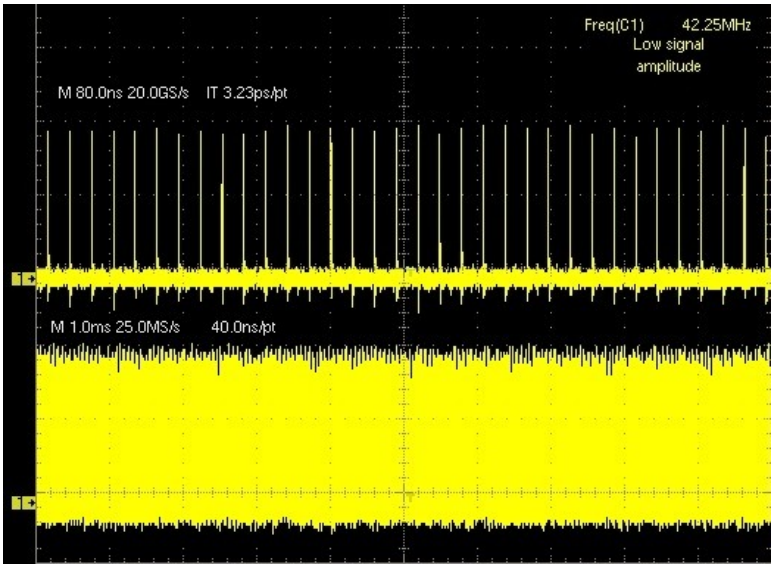

Fig. 4-10. Oscilloscope traces of 42.3 MHz KLAS laser pulse train: span of 80 ns/div (top) span of 1 ms/div (bottom).

The radio frequency (RF) spectrum of the pulse trains was measured using the DSA 800 spectrum analyzer from Rigol Technologies (range: 9 kHz-1.5GHz). The primary objective of the RF spectrum analyzer was to compare the strength of laser signal with respect to the noise signal. It helps to detect any unwanted oscillations, even a fraction of magnitude, and ensure that only the desired laser pulse of given repetition rate oscillates inside the cavity. In other words, the frequency spectrum analyzer helps to monitor the detrimental effect of multiple pulsing.

For single pulse measurements a span of 1 MHz with high resolution bandwidth of 1 kHz

was used (Fig. 4-11). For high resolution measurements the signals were taken using a fast photodetector (Thorlabs DET01CFC). For KLAS laser, the power ratio of signal to noise (dBc) was about 43.1 dBc (see Fig. 4-11).

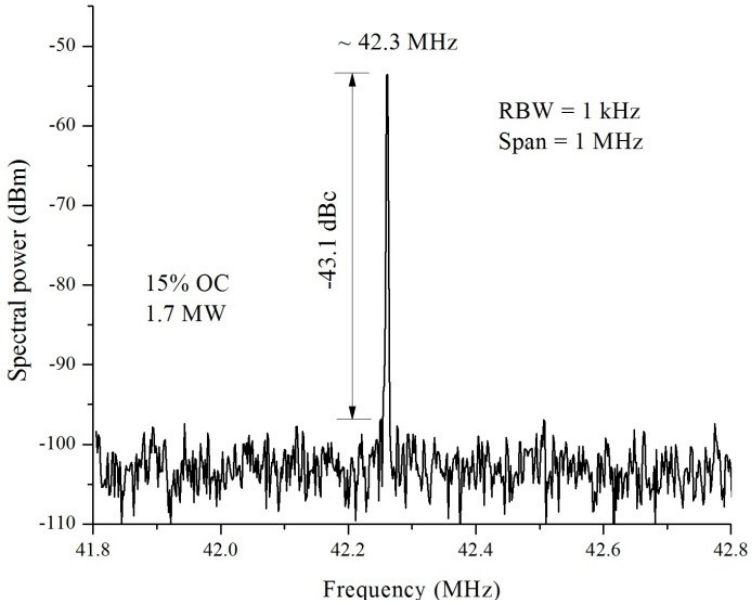

Fig. 4-11. Radio frequency (RF) spectrum of the fundamental harmonic with a frequency span of 1 MHz and resolution bandwidth (RBW) of 1 kHz.

The pulse duration was measured using the intensity autocorrelator (AC, Femtochrome FR-103 XL) with resolution <5 fs. The second harmonic crystal used in the autocorrelator was BBO of thickness 100 μm. To make sure the laser was still working in the single-pulse regime, the autocorrelator was scanned over the entire range of 200 ps. The secondary pulses that could be separated by more than 200 ps from the main one could be detected using an oscilloscope and a fast photodiode. The optical spectrum was measured using a high resolution spectrometer with resolution of 0.07 nm (Anritsu OSA MS9710B). The highest average output power of 3.25 W was achieved with 45 fs pulses using 15% OC and -1900 fs^2 of negative dispersion (see Fig. 4-12 & Fig. 4-13). This corresponds to a pulse energy of 77 nJ and a peak power of 1.7 MW. The

time-bandwidth product was calculated to be 0.369 indicating that the pulses were not completely transform limited. The intracavity peak power and pulse energy for 15% OC was about 11.3 MW and 0.5 μJ respectively.

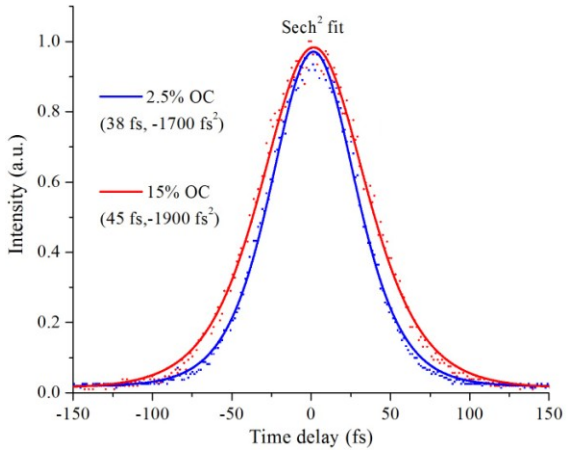

Fig. 4-12: KLAS laser. AC traces for 2.5% OC (shortest pulse) and 15% OC (highest peak power).

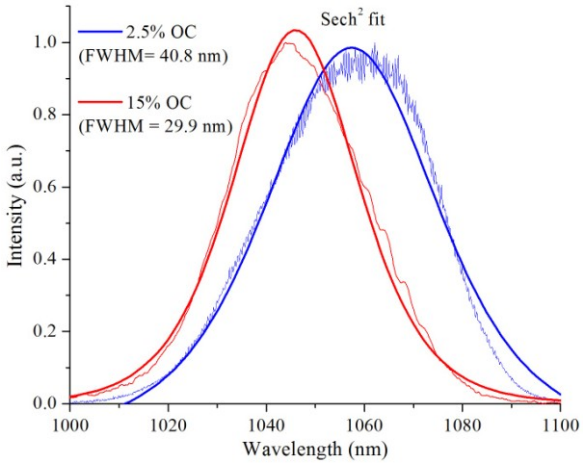

Fig. 4-13: KLAS laser. Spectrum for 2.5% OC and 15% OC with sech^2 fit.

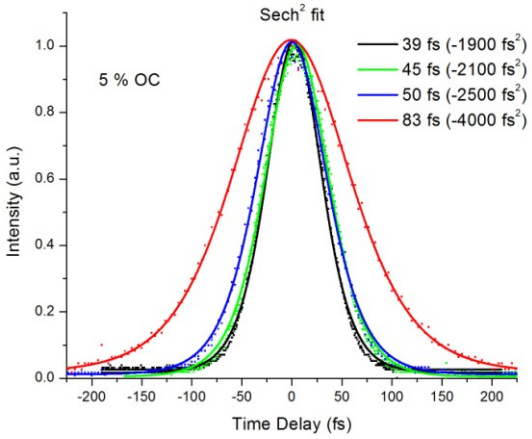

Fig. 4-14: KLAS laser. AC traces for 5% OC and different GDD values.

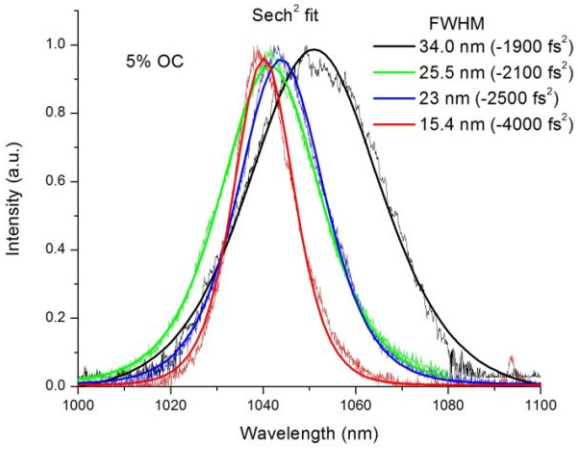

Fig. 4-15: KLAS laser. Spectrum for 5% OC and different GDD values.

In an attempt to achieve the shortest pulses, a 2.5% OC was employed in combination with a lower value of dispersion of -1700 fs^2. The average output power dropped to 300 mW and the measured pulse duration was 38 fs (Fig. 4-12). This corresponds to a pulse energy of 7 nJ and a peak power of 187 kW. The spectrum was about 40.8 nm broad (Fig. 4-13) resulting in the

time-bandwidth product of 0.416. A red shift of the central wavelength with respect to the 15% OC can be explained by the quasi-three-level nature of the gain [17]. Dispersive pulse broadening due to the output coupler was estimated to be less than 0.5 fs. The intracavity peak power and pulse energy for 2.5% OC was about 7.48 MW and 0.28 μJ respectively. The beam quality factor was measured for 15% OC in the vertical direction (y axis) and it is shown in Fig. 4-16.

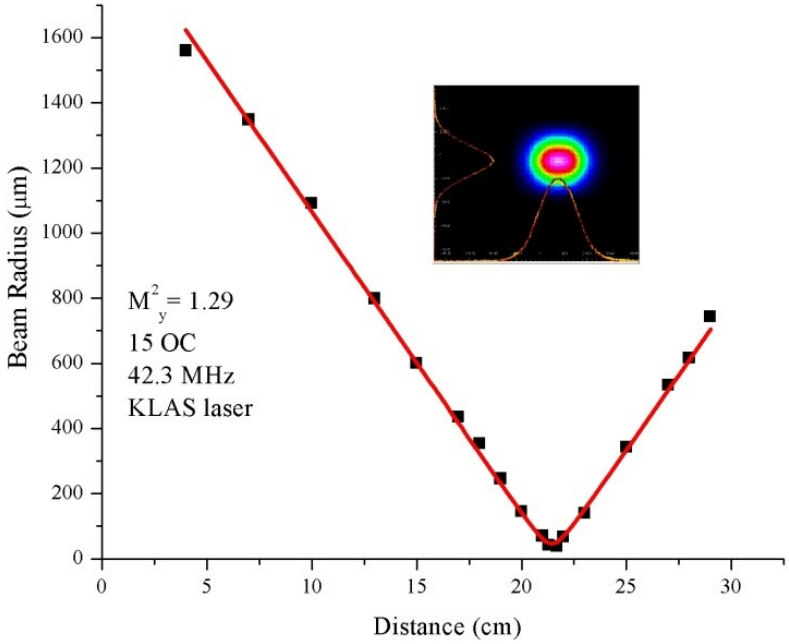

Fig. 4-16: Measured beam quality factor for KLAS laser was 1.29.

The summary of results for the 42.3 MHz KLAS laser is shown in Table 4-4. The spectral width in our case was most likely limited by the bandwidth of the chirped mirrors, dichroic mirror and the SESAM. The other output couplers that were tested with the laser were 5% and 10%. For 5% OC, as expected, shorter pulses were generated by reducing the negative dispersion as shown in Fig. 4-14 & Fig. 4-15 . The 5% OC resulted in 39 fs pulses with 485 kW of peak power and 10% OC produced 43 fs pulses with 880 kW. The pulse energies for 5% OC and 10%

OC were 19 nJ and 38 nJ (0.8 W and 1.6 W of average output power), respectively. The pulses were highly stable and easily reproducible. This OC was initially used to optimize the dispersion. The intracavity power was reduced for lower output couplers to prevent damage of the SESAM. In the future, higher peak power can be achieved by increasing the spot size on the SESAM, extending the cavity and increasing the output coupler transmission.

Table 4-4 : Summary of results for KLAS laser

KLAS Laser (42.3 MHz)	P_{avg} (W)	E_p (nJ)	P_{peak}(MW)	τ_p (fs)	TBP
2.5% OC	0.3	7	0.187	38	0.416
5% OC	0.8	19	0.485	39	0.36
10% OC	1.6	38	0.88	43	0.355
15 % OC	3.25	77	1.7	45	0.369

4.4.2 Design 2. Ultrashort pulse KLM laser with extended cavity laser design: 10.2 MHz repetition rate

Typical repetition rates of Yb-doped bulk femtosecond oscillators are in the range of 80-100 MHz. Some applications such as fluorescence lifetime imaging or seeding of amplifiers, however, require lower repetition rates. As an additional benefit, the pulse energy can be increased since it is inversely proportional to the repetition rate. Unfortunately, generation of ultrashort pulses (<100 fs) at low repetition rates (<40 MHz) is a challenging task because of the increased influence of the nonlinearities at higher pulse energies. This requires careful management of the dispersion and mode locking process.

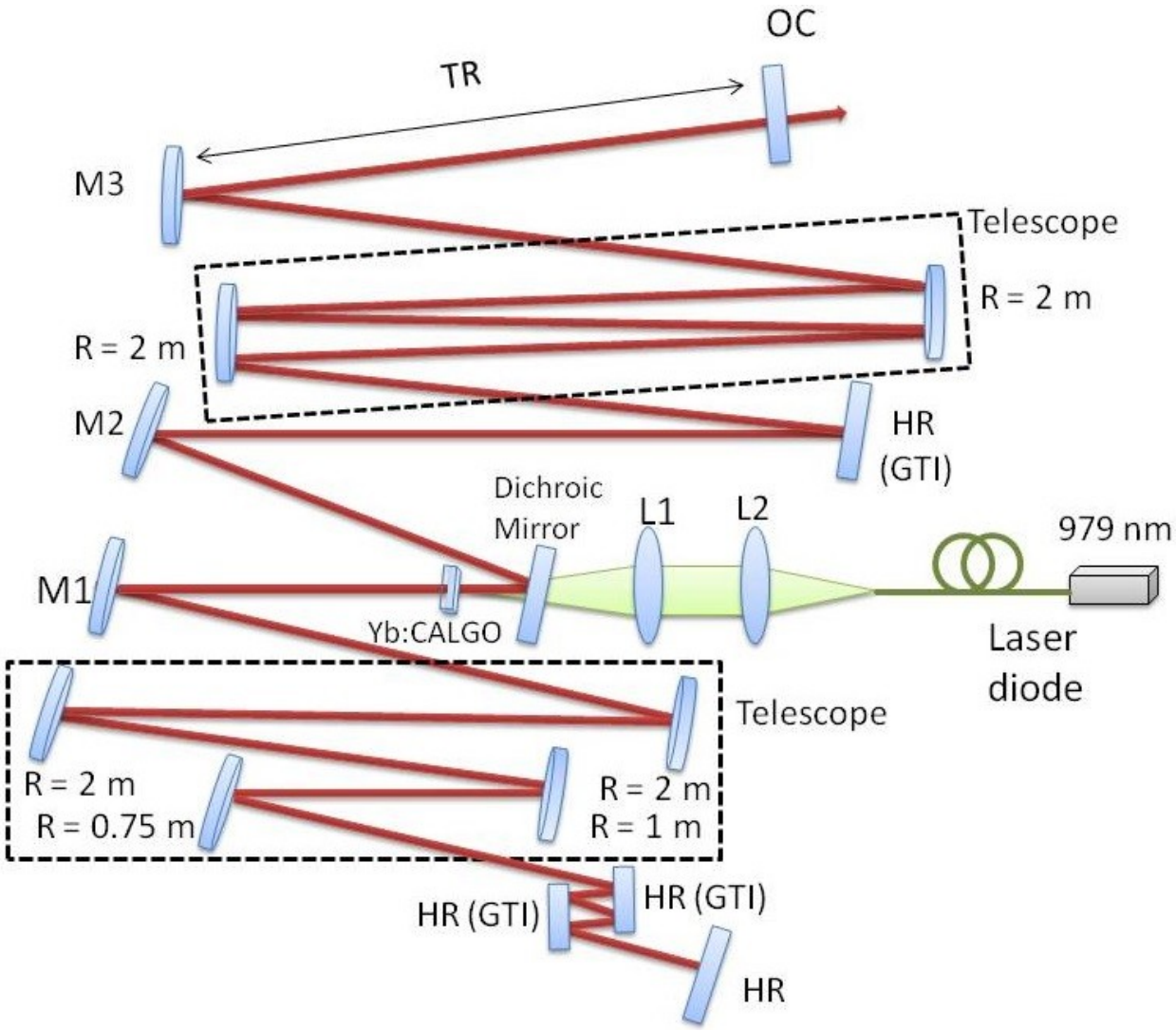

Fig 4-17: KLM laser set up: The curved mirrors: M1= 750 mm, M2= 600 mm and M3 = 500mm. GTI: chirped mirrors.

The developed KLM laser of 10.2 MHz repetition rate is shown in Fig 4-17. The laser was Kerr-lens mode-locked and directly diode-pumped by a fiber-coupled diode module. The basic laser design was very similar to the previously described KLAS laser. The length of the cavity was further increased with the help of several telescopic mirror arrangements as shown in the Fig 4-17. The total length of the cavity was about 14.7 m and the corresponding variation in beam radius from the end HR mirror to the OC is shown in Fig. 4-18. The use of additional

mirrors, slight adjustments in the cavity and the increased thermal lens attributed to the increase in the pump power and intracavity pulse energy pushed the laser further towards the edge of the stability region and the laser started to oscillate in the pulsed regime without the help of SESAM. The ML was started by a slight tapping on one of the end mirrors.

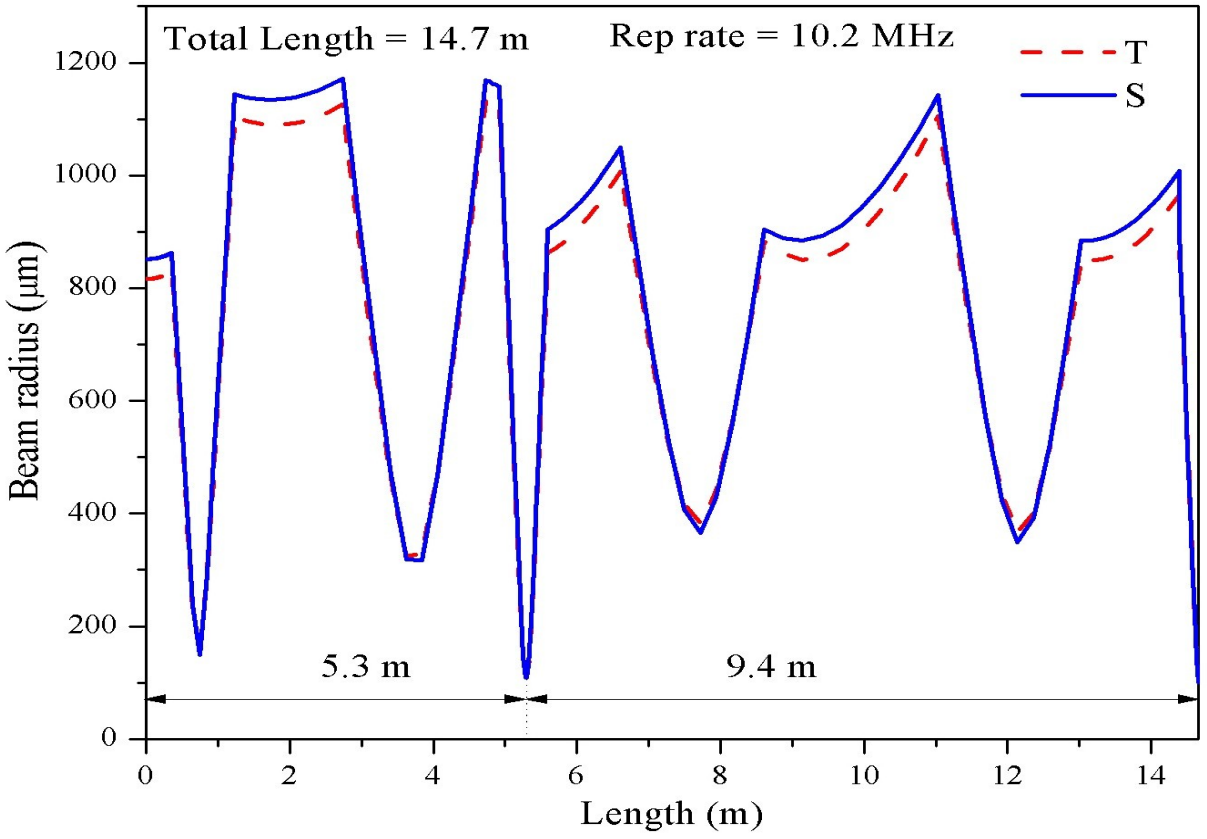

Fig. 4-18: Beam radius of KLM laser along the cavity. The long arm was about 9.4 m and the short arm was about 5.3 m long. Dotted line denotes the tangential plane and solid line denotes the sagittal plane.

4.4.2.1 Results and discussions (KLM laser)

Firstly, the power measurements were recorded for the KLM laser and the highest average power recorded was 1 W using 10% OC. However, because of the low repetition rate of 10.2 MHz, this would correspond to a pulse energy of 98 nJ. Using 10% OC, the mode locking was obtained at an incident pump power of 23.1 W of which 19.1 W was absorbed. Then the 10% OC was

replaced by 5% OC and the mode locking was observed at an incident pump power of 20.4 W (16.7 W of pump power absorbed). The generated average output power was 650 mW and the pulse energy was 64 nJ.

For KLM laser, all the previously mentioned measurements were also taken. Initially, the pulse train was recorded using an oscilloscope (Fig 4-19). The oscilloscope recoded pulse train frequency of 10.22 MHz which was in total agreement with the design. No modulations were observed in either shorter (200 ns/div) or longer (1 μs/div) time spans. The next step was to employ the RF spectrum analyzer to verify that the laser was working in the single-pulse regime.

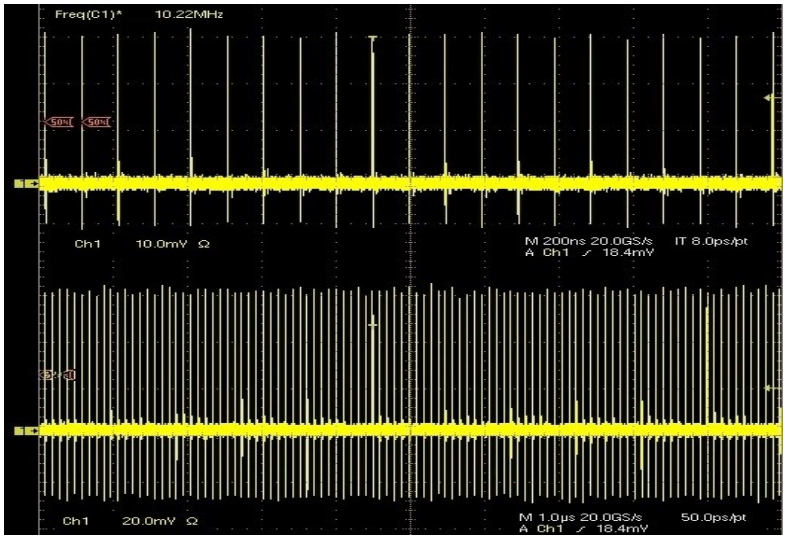

Fig 4-19: Oscilloscope traces of the 10.2 MHz KLM laser: span of 200 ns/div (top) span of 1 μs/div (bottom).

The RF spectrum analyzer recorded a single pulse in a frequency span of 1 MHz and the measured spectral power was 47 dBc above the noise background (see Fig. 4-20). Further verifications of the single pulse mode locking were also done by recording a large span of 100 MHz (see inset Fig. 4-20). For a span of 100 MHz a slow photodetector (Thorlabs02AFC) was

used. These observations ruled out the possibility of multiple pulsing or any other unwanted oscillations.

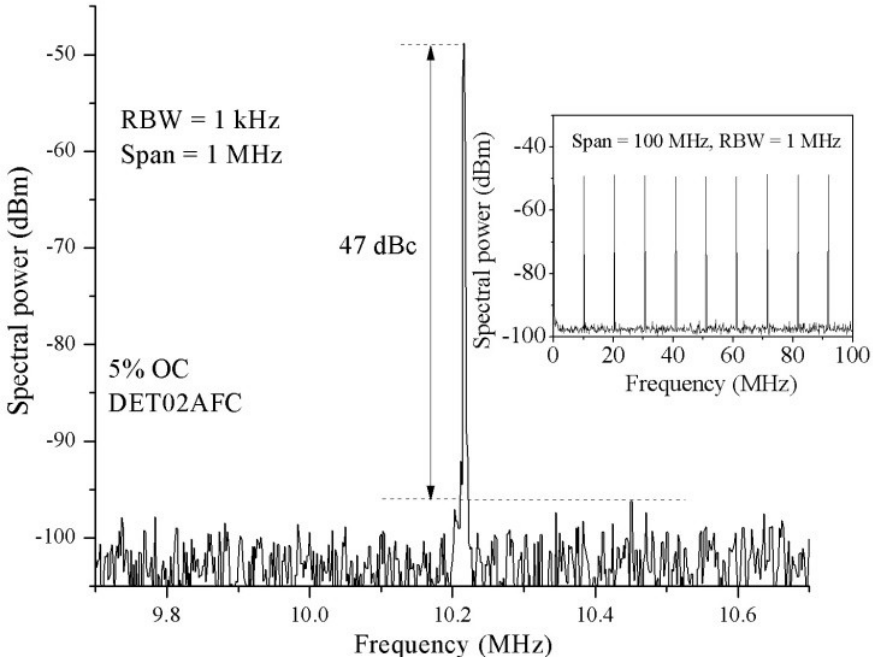

Fig. 4-20: Frequency spectrum of 10.2 MHz laser. Inset shows a span of 100 MHz.

As mentioned earlier, the pulse duration was measured using an intensity autocorrelator (see Fig 4-21) and the spectrum (Fig. 4-22) was recorded using a high resolution spectrometer. The pulse duration was 72 fs and the FWHM of spectrum was 21.1 nm for 10% OC and a shorter pulse of 66 fs (FWHM spectrum was 17.7 nm) was measured for 5 % OC. The peak power was 1.36 MW and 0.97 MW respectively. No external pulse compression or prisms were used in the design. Dispersion compensation was achieved using only intracavity chirped mirrors. Negative dispersion (per round trip) used for 10% OC was -3800 fs^2 and for 5% OC was -3200 fs^2.

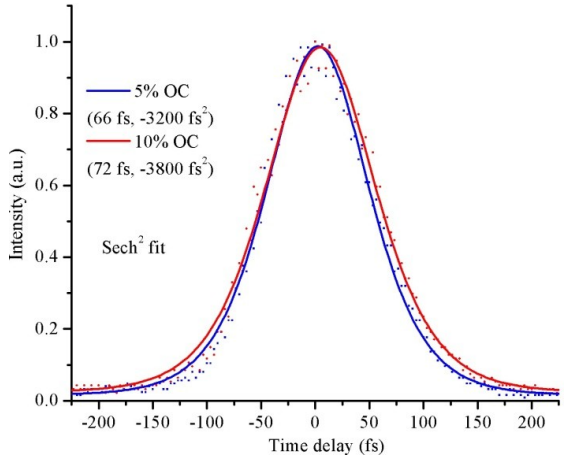

Fig 4-21: KLM laser. AC traces for 5% and 10% OC.

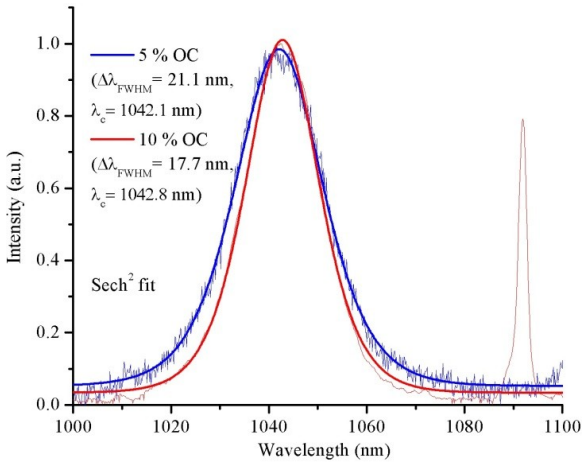

Fig. 4-22: KLM laser. Spectrum for 5% and 10% OC.

The measured beam quality factor for KLM laser is shown in Fig 4-23. The beam quality factor was measured for 10% OC and the beam profile is shown in the inset. The measured beam quality factor was 1.44 and 1.41 for x and y axis, horizontal and vertical directions, respectively. Summary of the 10.2 MHz KLM laser results is shown in Table 4-5.

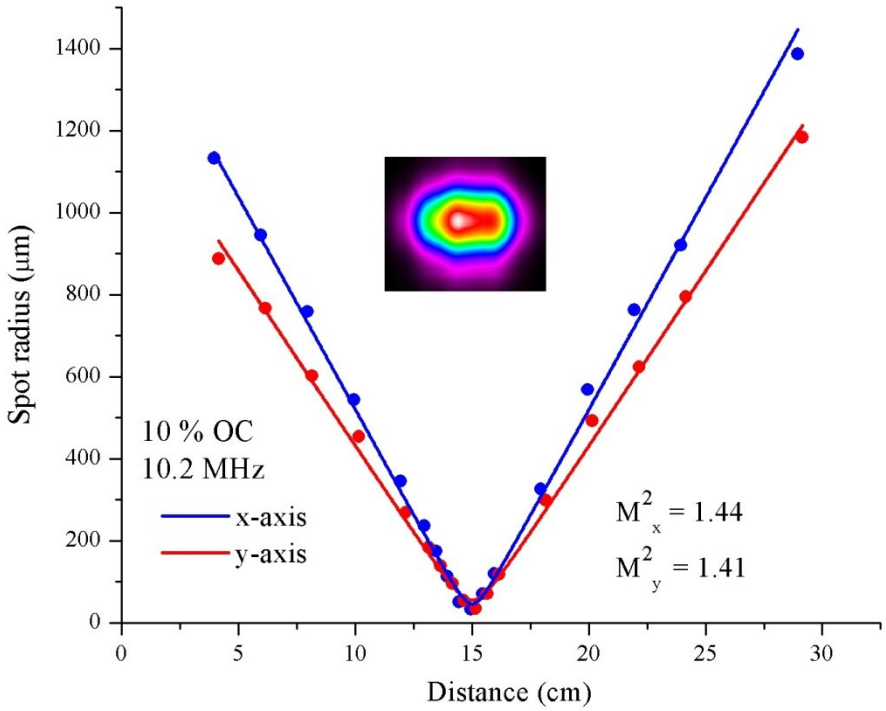

Fig 4-23: Measured beam quality factor for KLM laser was 1.4. Inset: beam intensity profile.

Table 4-5: Summary of results for KLM laser.

KLM laser (10.2 MHz)	P_{avg} (W)	E_p (nJ)	P_{peak}(MW)	τ_p(fs)	TBP
5% OC	0.65	64	0.97	66	0.384
10% OC	1	98	1.36	72	0.351

4.5 Comparison

Comparing the above two lasers, the KLAS laser was able to generate higher peak power and shorter pulses than the KLM laser. However, the KLM laser was able to generate higher pulse energy because of the low repetition rate. The average power was only one-third for the KLM laser when compared to the KLAS laser. The KLM cavity was about 4 times longer than the KLAS cavity and it contained several more curved mirrors and GTI mirrors. One possible explanation for lower average power would be the extra loss caused by the additional mirrors. Another possible explanation is that, for starting the KLM regime, it is required to work closer to the stability edge. The average power drops at the edges of the stability region. It is assumed that a combination of both of the above mentioned reasons contributed to a lower average power. One of the advantages of the KLM laser was absence of the Q-switching instabilities. The Q-switching instabilities in KLAS were mainly caused by the SESAM. The time delay between two consecutive pulses was approximately 24 ns in the KLAS laser and 98 ns in the KLM laser as shown in Fig. 4-24.

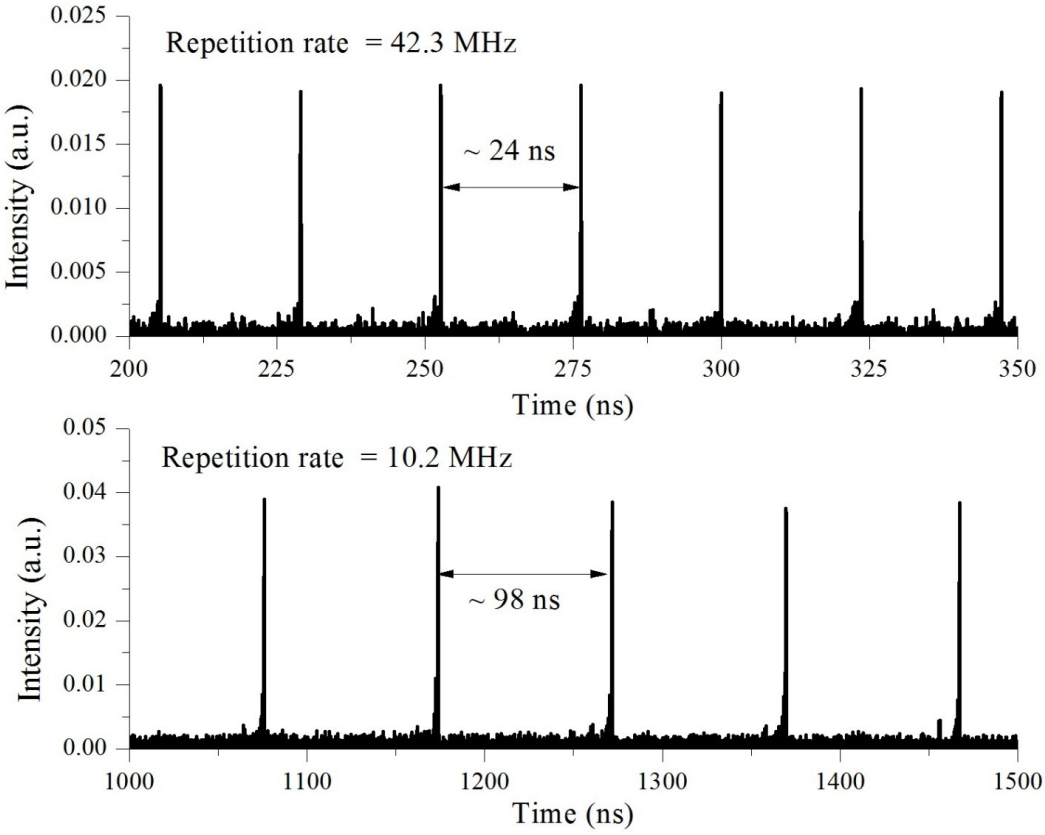

Fig. 4-24: Time delay between the consecutive pulses for 42.3 MHz laser and 10.2 MHz laser.

The summary of pulse energies measured using different OC's from both lasers are shown in Fig. 4-25. The graph (Fig. 4-25) shows that the pulse duration is scaled with the output coupler transmission.

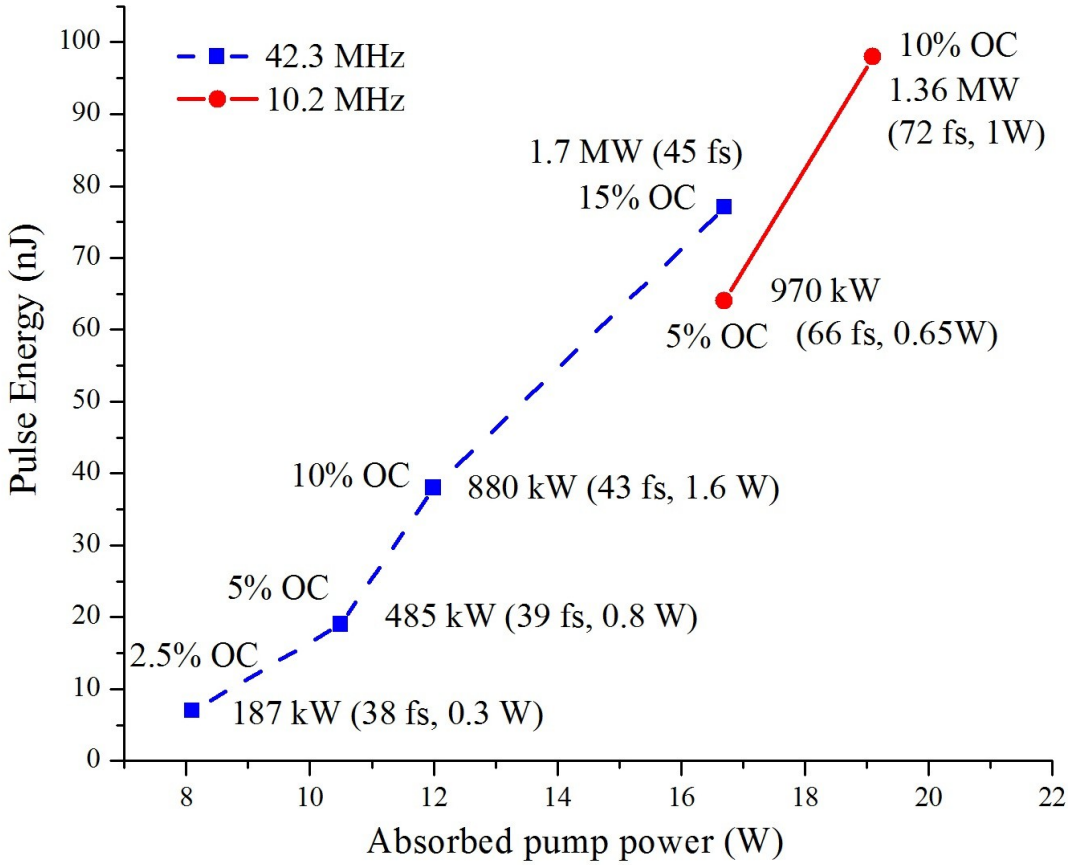

Fig. 4-25. Output power, peak power and pulse energy for different output couplers versus the pump power.

The results are compared with other Yb-doped lasers in Fig. 4-26. Both thin-disk lasers (TDL) and bulk (B) lasers as well as diode-pumped (DP) and non diode-pumped lasers were considered. It can be seen that there is no other bulk crystal solid-state laser or TDL that work in the sub-50 fs with more than 1.5 MW peak power. The major competition is from the TDL. TDL has the advantage of better thermal management; however, it has a complex pump power system design and requires higher pump power [7, 18].

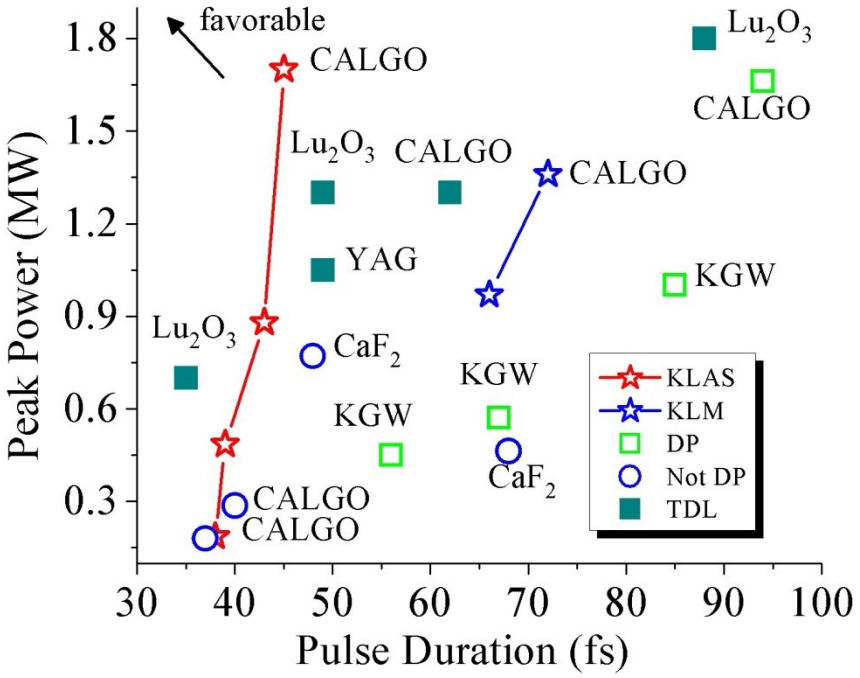

Fig. 4-26: Comparison with other (>100 kW of peak power) ultrafast lasers. Yb: CALGO [7, 10, 19], Yb:Lu_2O_3 [18], Yb:CaF_2 [20, 21], Yb:KGW [22], Yb:YAG [8]. Solid points represent TDL and hollow points are bulk gain media. DP represent diode-pumped.

As mentioned earlier, there are only a few lasers that can generate sub-100-fs pulses in the low-repetition regime. Fig. 4-27 clearly shows that KLM laser at 10.2 MHz can claim the lowest repetition rate for diode-pumped solid-state laser in the sub-100-fs region, whereas the KLAS laser can claim the lowest repetition rate for diode-pumped solid-state laser in the sub-50-fs regime. These are one of the shortest pulses that were generated *directly* from the diode-pumped Yb:CALGO lasers to date and, at the same time, the most powerful in the sub-40 fs regime. Recently, F. Pirzio *et al.* reported 36 fs pulses with a relatively low peak power of 3 kW [23]. The 40 fs pulses reported in [19] were obtained only after extracavity compression starting from the 70 fs pulses emitted by the laser oscillator.

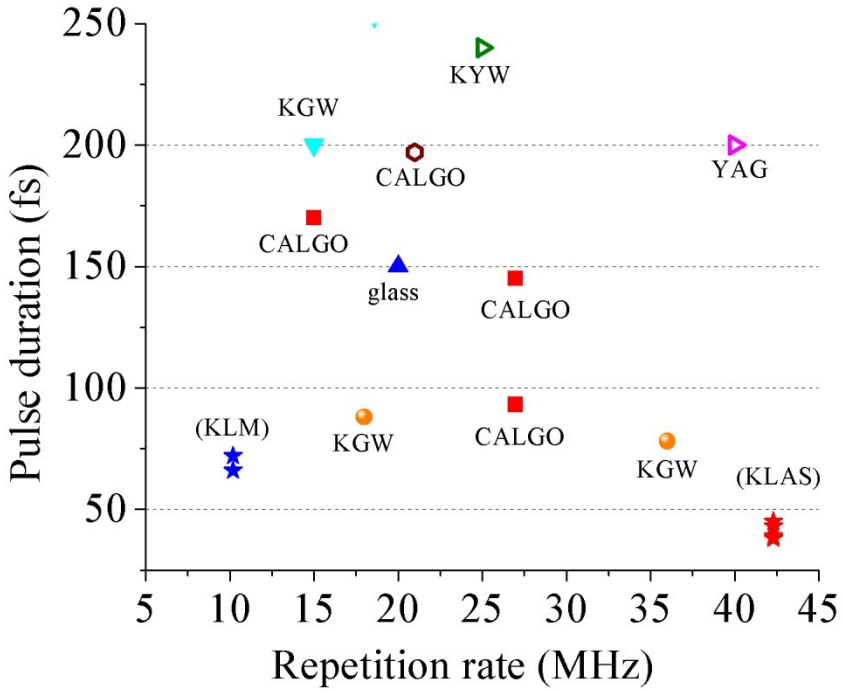

Fig. 4-27. Comparison with other low-repetition rate lasers (<45 MHz) ultrafast lasers.

One of the ways to highlight the efficiency of the developed lasers is to calculate the ratio of peak power with respect to the incident pump power. This peak-to-pump power efficiency (η_{p-p}) is calculated as follows:

$$\eta_{p-p} = \frac{P_{peak}}{P_{pump}} = \frac{\eta_{opt-opt}}{f_{rep} \times \tau_p}, \qquad \text{and} \qquad P_{peak} = \frac{E_{pulse}}{\tau_p} = \frac{P_{avg}}{f_{rep} \times \tau_p} \;\; \& \;\; E_{pulse} = \frac{P_{avg}}{f_{rep}}$$

and can be thought as the optical-to-optical efficiency $\eta_{opt\text{-}opt}$ normalized with respect to the pulse duration and repetition rate. In this expression P_{peak} and P_{avg} are the peak power and average power, respectively, τ_p and f_{rep} are the pulse duration and repetition rate. A comparison of this parameter is shown in Fig. 4-28. It is worthwhile to reiterate that an incident diode pump power of just 20.4 W was capable of producing up to 1.7 MW of peak power with a laser beam quality

factor of M^2= 1.3.

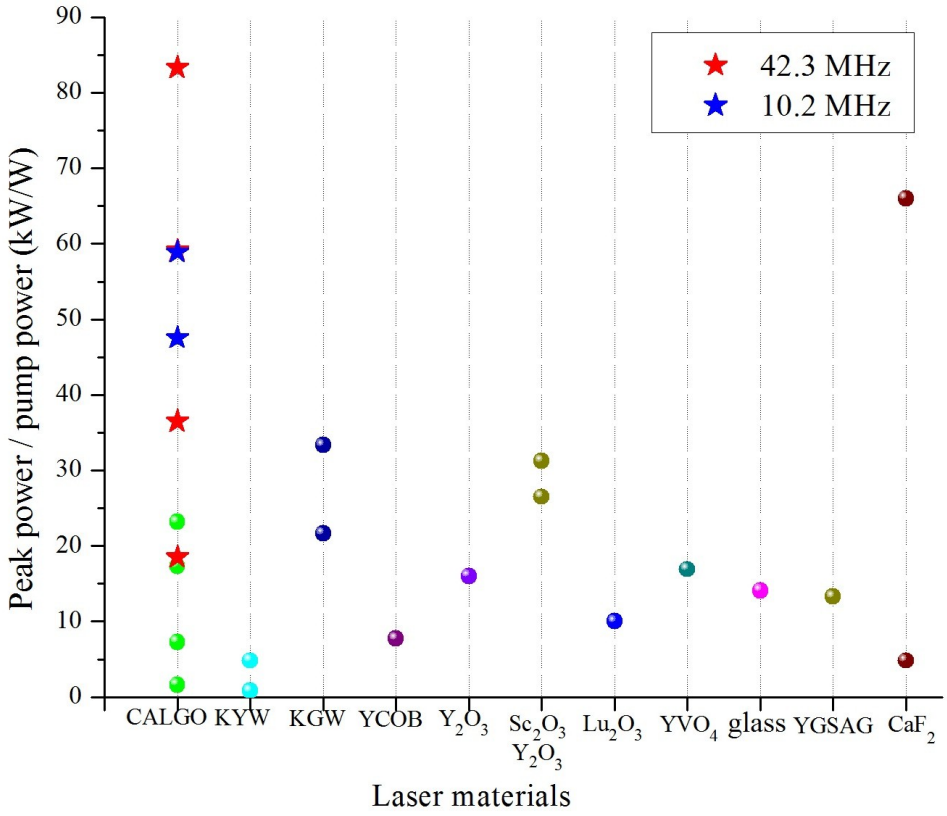

Fig. 4-28. Comparison of peak to-pump power efficiency with other Yb-doped lasers in the sub-100 fs regime.

4.6 **Challenges**

Mode locking becomes more challenging at this power and pulse duration range. Saturable absorber mirrors get easily damaged and therefore the fluence should be precisely controlled to prevent this detrimental effect. At the same time critical cavity alignment is required for KLM (see appendix B).

CW mode, spectral sidebands and stability issues were the most common challenges associated with the ML laser design. In other words, spectral sidebands indicate that the dispersion compensation was inadequate.

The wavelength scan range of 1000-1100 nm was used to detect sidebands and spectrum modulations. If the dispersion was not compensated in the right amount, sidebands were most likely to appear in the spectrum as shown in Fig. 4-29. Multi-pulsing was also a major challenge in the ML processes. Multiple pulses with separation greater than 200 ps could be easily detected with the help of the used fast oscilloscope and photodetector. Mutiple pulses with less than 200 ps separation were detected using an autocorrelator (see Fig. 4-30). They could be also detected using a spectrometer. Multiple pulsing can be avoided by adjusting the pump power or spot size on the crystal/SESAM or optimizing the intracavity negative dispersion.

Dispersive pulse broadening due to the output coupler was estimated using the equation 4.18.

$$t = \tau_0 \sqrt{1 + \left(\frac{4 \ln 2 \cdot D \cdot L}{\tau_0^2}\right)^2} \qquad 4.18$$

where t and τ_0 are the initial and final pulse duration respectively. D represents the group velocity dispersion and L is the length of the material. Dispersive pulse broadening due to the output coupler of thickness 6.35 mm was estimated to be about ~5 fs.

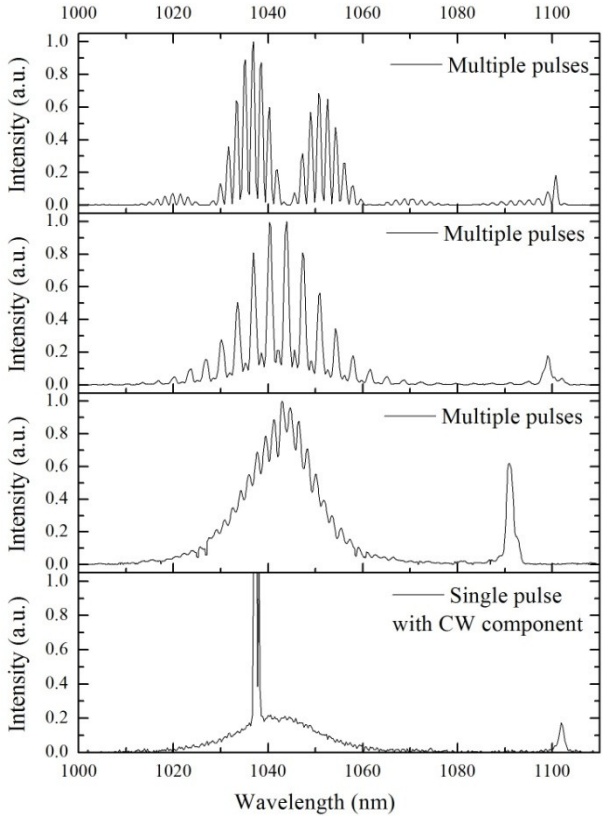

Fig. 4-29: Spectrometer traces of multi-pulsing.

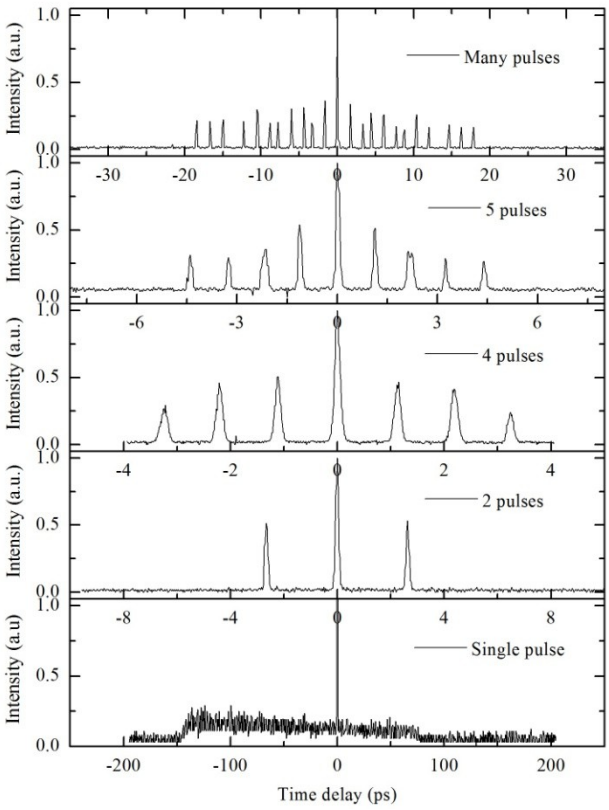

Fig. 4-30: Autocorrelator traces of multi-pulsing.

4.7 **Conclusion**

In this chapter the design and development of two ultra-short pulse lasers operating in the sub-100-fs regime was explained in detail and the associated challenges were discussed. As mentioned earlier, sub-100-fs lasers with MW peak power are not available in the commercial market. This points out to the challenges and complexity in the design and development of such lasers. Two slightly different technologies, namely KLAS and KLM, were employed to achieve these results.

Using the KLAS method, a high peak power diode-pumped bulk Yb:CALGO laser oscillator in the sub-50-fs category was demonstrated. The peak power of 1.7 MW was produced using 15% OC with 45 fs long pulses. Such sources are very attractive for nonlinear frequency

conversion and spectroscopy. Very short pulses of 38 fs were also generated using the KLAS method. By careful optimization of intracavity dispersion profile even shorter pulses can be generated directly from the diode-pumped Yb:CALGO lasers.

The pulse energy was further increased by developing a low-repetition rate KLM laser. The KLM Yb:CALGO laser operating at 10.2 MHz repetition rate generated 66 fs and 72 fs pulses with 64 nJ and 98 nJ of pulse energy, respectively. The laser was Kerr-lens mode-locked and directly diode-pumped by a fiber-coupled diode module. To the best of our knowledge, this is the first Yb:CALGO laser that generated sub-100 fs pulses directly out of the cavity at such a low repetition rate. Low repetition rate was achieved by extending the laser cavity using a telescopic mirror arrangement. No external pulse compression was used. This simple design excludes the use of any complex electronics, pulse pickers or cavity dumping. The oscillator produced 650 mW of average power for 5% OC and 1 W average power for 10% OC. This corresponds to a peak power of 0.97 MW and 1.36 MW, respectively. The ~98 ns time delay between the pulses can be useful for fluorescence lifetime imaging of biological samples.

In conclusion, these results show that Yb:CALGO is one of the best choices for intense ultrashort pulse generation. Taking into account that current record of high peak power pulses in the sub-100 fs soliton mode locking regime belongs to Ti:sapphire and is 3.5 MW [24], further peak power scaling of our design should be still possible. Further research is recommended using this crystal for power-scaling. One of the recommended approaches for power-scaling is to use an alternative pumping geometry (e.g. grazing incidence that is discussed in section 6.2.1). These high intensity ultrashort pulse lasers open a window of nonlinear applications to be tested. Some of the nonlinear applications are discussed in the next chapter.

.

4.8 References

[1] A. Major, D. Sandkuijl, and V. Barzda, "Efficient frequency doubling of a femtosecond Yb:KGW laser in a BiB_3O_6 crystal," *Optics Express,* vol. 17, pp. 12039-12042, 2009.

[2] V. Kumar, R. Osellame, R. Ramponi, G. Cerullo, and M. Marangoni, "Background-free broadband CARS spectroscopy from a 1-MHz ytterbium laser," *Optics Express,* vol. 19, pp. 15143-15148, 2011.

[3] A. S. Meyer, A. J. Squier, and A. S. Diddams, "Diode-pumped Yb:KYW femtosecond laser frequency comb with stabilized carrier-envelope offset frequency," *The European Physical Journal D,* vol. 48, pp. 19-26, 2008.

[4] S. Manjooran, H. Zhao, I. T. Lima, Jr., and A. Major, "Phase-matching properties of PPKTP, MgO:PPSLT and MgO:PPcLN for ultrafast optical parametric oscillation in the visible and near-infrared ranges with green pump," *Laser Physics,* vol. 22, pp. 1325-1330, 2012.

[5] P. Sévillano, P. Georges, F. Druon, D. Descamps, and E. Cormier, "32-fs Kerr-lens mode-locked Yb:$CaGdAlO_4$ oscillator optically pumped by a bright fiber laser," *Optics Letters,* vol. 39, pp. 6001-6004, 2014.

[6] Z. Gao, J. Zhu, J. Wang, Z. Wei, X. Xu, L. Zheng*, et al.*, "Generation of 33 fs pulses directly from a Kerr-lens mode-locked Yb:$CaYAlO_4$ laser," *Photonics Research,* vol. 3, pp. 335-338, 2015.

[7] A. Diebold, F. Emaury, C. Schriber, M. Golling, C. J. Saraceno, T. Südmeyer*, et al.*, "SESAM mode-locked Yb:$CaGdAlO_4$ thin disk laser with 62 fs pulse generation," *Opt. Lett.,* vol. 38, pp. 3842-3845, 2013.

[8] J. Zhang, J. Brons, M. Seidel, D. Bauer, D. Sutter, V. Pervak*, et al.*, "Generation of 49-fs pulses directly from distributed Kerr-lens mode-locked Yb:YAG thin-disk oscillator," *Advanced Solid State Lasers, Berlin, OSA,* p. ATh4A.7, 2015.

[9] H. Zhao and A. Major, "Megawatt peak power level sub-100 fs Yb:KGW oscillators," *Optics Express,* vol. 22, pp. 30425-30431, 2014.

[10] A. Greborio, A. Guandalini, and J. Aus der Au, "Sub-100 fs pulses with 12.5-W from Yb:CALGO based oscillators," *Proc. SPIE,* vol. 8235, pp. 823511-1, 2012.

[11] U. Keller, K. J. Weingarten, F. X. Kartner, D. Kopf, B. Braun, I. D. Jung*, et al.*, "Semiconductor saturable absorber mirrors (SESAM's) for femtosecond to nanosecond pulse generation in solid-state lasers," *Selected Topics in Quantum Electronics, IEEE Journal of,* vol. 2, pp. 435-453, 1996.

[12] E. Caracciolo, M. Kemnitzer, A. Guandalini, F. Pirzio, A. Agnesi, and J. Aus der Au, "High pulse energy multiwatt Yb:$CaAlGdO_4$ and Yb:CaF_2 regenerative amplifiers," *Optics Express,* vol. 22, pp. 19912-19918, 2014.

[13] U. Keller, "Ultrashort pulse generation," in *Advances in Lasers and Applications: Proceedings of the 52nd Scottish University Summer School in Physics*, D. M. Finlayson and B. D. Sinclair, Eds., ed: Institute of Physics Publishing and Scottish Universities Summer Schools in Physics, 1999, p. 83.

[14] K. Ursula, "Recent developments in compact ultrafast lasers," *Nature,* vol. 424, pp. 831-838, 2003.

[15] G. R. Holtom, "Mode-locked Yb:KGW laser longitudinally pumped by polarization-coupled diode bars," *Optics Letters,* vol. 31, pp. 2719-2721, 2006.
[16] H. Zhao and A. Major, "Powerful 67 fs Kerr-lens mode-locked prismless Yb:KGW oscillator," *Optics Express,* vol. 21, pp. 31846-31851, 2013.
[17] H. Zhao and A. Major, "Dynamic characterization of intracavity losses in broadband quasi-three-level lasers," *Opt. Express,* vol. 22, pp. 26651-26658, 2014.
[18] C. Paradis, N. Modsching, V. J. Wittwer, B. Deppe, C. Kränkel, and T. Südmeyer, "Generation of 35-fs pulses from a Kerr lens mode-locked Yb:Lu_2O_3 thin-disk laser," *Opt. Express,* vol. 25, pp. 14918-14925, 2017.
[19] A. Agnesi, A. Greborio, F. Pirzio, G. Reali, J. Aus der Au, and A. Guandalini, "40-fs Yb^{3+}:$CaGdAlO_4$ laser pumped by a single-mode 350-mW laser diode," *Opt. Express,* vol. 20, pp. 10077-10082, 2012.
[20] G. Machinet, P. Sevillano, F. Guichard, R. Dubrasquet, P. Camy, J. L. Doualan*, et al.*, "High-brightness fiber laser-pumped 68 fs- 2.3 W Kerr-lens mode-locked Yb:CaF_2 oscillator," *Opt. Lett.,* vol. 38, pp. 4008-4010, 2013.
[21] P. Sevillano, G. Machinet, R. Dubrasquet, P. Camy, J.-L. Doualan, R. Moncorge*, et al.*, "Sub-50 fs, Kerr-lens mode-locked Yb:CaF_2 laser oscillator delivering up to 2.7 W," in *Advanced Solid-State Lasers Congress*, Paris, 2013, p. AF3A.6.
[22] H. Zhao and A. Major, "Megawatt peak power level sub-100 fs Yb:KGW oscillators," *Opt. Express,* vol. 22, pp. 30425-30431, 2014.
[23] F. Pirzio, M. Kemnitzer, A. Guandalini, F. Kienle, S. Veronesi, M. Tonelli*, et al.*, "Ultrafast, solid-state oscillators based on broadband, multisite Yb-doped crystals," *Opt. Express,* vol. 24, pp. 11782-11792, 2016.
[24] J. A. M. Kowalevicz, A. T. Zare, F. X. Kärtner, J. G. Fujimoto, S. Dewald, U. Morgner*, et al.*, "Generation of 150-nJ pulses from a multiple-pass cavity Kerr-lens mode-locked Ti:Al_2O_3 oscillator," *Opt. Lett.,* vol. 28, pp. 1597-1599, 2003.

Chapter 5: Applications of intense ultrashort pulse laser

5.1 Introduction and preview

In this part of work a few nonlinear and spectroscopic applications of the developed lasers were studied. The results and discussions are presented in this chapter. The chapter begins with a detailed study on green light pumped optical parametric oscillators (section 5.3). Ultrashort pulses with wavelength tuning in the visible and near-infrared (VNIR) ranges (here approximately from ~700 nm to 2000 nm) have wide application in many biomedical devices especially in imaging and spectroscopy. The theoretical studies in this chapter considered the phase-matching conditions of three periodically poled crystals (PPKTP, MgO:PPcLN and MgO:PPSLT) to use for femtosecond optical parametric oscillators (OPO) to generate wavelength tunability in this range. The basic optical properties and the wavelength tuning ranges were calculated with respect to different grating periods and temperature variation. Dispersive properties of crystals relevant to the ultrafast operation regime were also discussed. The excitation wavelength used for the analysis is 520 nm (green light) which is the second harmonic wavelength of the Yb-doped ultrashort pulse solid-state lasers. The concept of the wavelength tunable femtosecond OPOs with green excitation presented here can be a better alternative to the widely used expensive Ti:sapphire lasers.

In addition, three application tests were conducted using the KLM laser demonstrated in the previous chapter. The most simple and straightforward application was second harmonic generation (SHG) as shown in section 5.4. At the same time one of the most interesting and

current hot topic is supercontinuum generation using photonic crystal fibers. This application and initial experiments are discussed in section 5.5. Raman spectroscopy and CARS microscopy are a major application of intense short pulse lasers. A few initial experiments and thoughts are presented in section 5.6. Being proof-of-principle tests, their primary objective was to demonstrate the capability of the generated intense ultrashort pulse laser.

5.2 **Phase-matching conditions for nonlinear process**

When light interacts with matter, if there is no net transfer of energy or momentum between the medium and the optical field then it is called a parametric process. Two examples of parametric processes are second harmonic generation and optical parametric oscillation. Both these are nonlinear optical frequency conversion processes and highly phase-sensitive. To obtain an efficient frequency conversion, the interacting fields have to maintain a proper phase relationship with each other along the propagation direction. These phase relationships are called phase-matching conditions. The phase-matching condition for SHG in terms of refractive indices is $n(\omega) = n(2\omega)$, i.e. the phase velocities of the fundamental (ω) and second (2ω) harmonics must be the same. The phase-matching conditions for the OPO are given in the following section.

5.3 **Green pumped optical parametric oscillator**

Ultrashort pulse optical parametric oscillator with wavelength tunable in the visible-near-infrared (VNIR) region is highly useful in microscopy and spectral imaging of biological samples. In nonlinear microscopy this wavelength range is important because of the low absorption in biological materials and therefore it is extensively used in label-free imaging of tissues and living cells [1-3]. Another possible application of such an OPO is in the generation of supercontinuum

light source in the visible range, to study the vibrational spectra of materials using coherent anti-Stokes Raman scattering (CARS) technique [4]. This wavelength range (700-2000 nm) is also widely used in nonlinear spectroscopy of various optical materials [5, 6]. Moreover, a previous research work showed that ultrashort pulses at 520 nm produced by the frequency doubled Yb-doped solid-state lasers can be used as an excitation source for optical DNA biosensors [7, 8].

Considering these factors, there is a significant motivation to design and develop widely tunable (700-2000 nm) femtosecond OPOs pumped with the frequency doubled Ytterbium-doped laser sources, since these are more cost effective than the commonly used Ti:sapphire lasers [9]. Recently it has been demonstrated that ultrafast OPOs pumped with the fundamental wavelength (1020-1060 nm) of Ytterbium-doped lasers are reliable sources of wavelength tunable infrared femtosecond laser pulses [10, 11]. To extend the wavelength tunability, feasibility of pumping using second harmonic wavelength (520 nm) of Ytterbium-doped lasers is studied in this section. To the best of our knowledge, this is the first time that the phase-matching properties of these three periodically poled nonlinear crystals were thoroughly studied for 520 nm excitation wavelength.

In optical parametric interaction, the phase-matching is an essential condition for the effective generation of the signal and idler fields. Quasi-phase-matching (QPM) is an efficient technique to achieve non-critical phase-matching for any wavelength in the transparency range of a given nonlinear crystal. The application of QPM to bulk nonlinear crystals is implemented by electric field poling techniques, for example, the periodic electrode can be fabricated on the surface of the crystal substrates by conventional photolithography [12].

In the following studies, the wavelength tunability was calculated for three periodically poled crystals: $KTiOPO_4$ (PPKTP), stoichiometric 0.5% MgO-doped $LiTaO_3$ (MgO:PPSLT) and

congruent 5% MgO-doped $LiNbO_3$ (MgO:PPcLN). These crystals were selected based on their availability and high performance in different power regimes. For example PPcLN has large nonlinear coefficient and it is good for low power but in high power applications PPSLT or PPKTP are preferred. PPcLN suffers from photorefractive effect, thermal damage and high coercive field. High coercive field limits the thickness of the medium. PPKTP is resistant to the photorefractive damage and its coercive field is ten times lower than that of PPcLN. Some properties of these periodically poled crystals are given in Table 5-1, where d_{eff} is the effective nonlinear coefficient and d_{33} is the highest nonlinear susceptibility tensor element.

Table 5-1 Comparison of the nonlinear coefficient, coercive field and temperature coefficients of PPKTP, PPcLN and PPSLT

Material	**Coercive field (kV/mm)**	**d_{eff} (pm/V)**	**d_{33} (pm/V)**	**Temperature coefficient [K^{-1}]**	
				α coefficient	β coefficient
PPcLN [11] [13]	21	~ 17	27	1.54×10^{-5}	5.3×10^{-9}
PPKTP [14] [15]	2	~ 9.5	12.9	6.7×10^{-6}	11×10^{-9}
PPSLT [16] [17, 18]	1.7	~ 6.7	15	1.6×10^{-5}	7×10^{-9}

Photorefractive damage threshold of periodically poled crystals can be improved in some cases by doping with magnesium oxide (MgO). MgO doped $LiNbO_3$ and $LiTaO_3$ has several orders of magnitude higher resistance to photorefractive damage than the undoped $LiNbO_3$ and $LiTaO_3$, while maintaining the advantage of high nonlinear coefficient [19]. MgO doping results in a decrease in refractive index and also helps in easier fabrication of uniform QPM gratings [20].

Photorefractive damage threshold of MgO:PPcLN and MgO:PPSLT decreases with shorter wavelengths [21]. In order to reduce this detrimental effect at 520 nm excitation

wavelength, an elevated temperature (100°C) can be used for these two crystals. Heating these two crystals to 100°C can significantly reduce the inhomogeneities in the refractive index [22] [23]. The ordinary and extraordinary refractive indices of nonlinear crystals can be experimentally determined using spectroscopic [24] or fluorescence [25] techniques.

5.3.1 Theory and Calculation

In optical parametric interaction, the converted wave with shorter wavelength is called the signal and the converted wave with the longer wavelength is called the idler. The equation 5.1 represents the energy conservation condition and the equation 5.2 gives the quasi-phase-matching condition. These two conditions must be satisfied simultaneously to obtain the optical parametric interaction for a given nonlinear material.

$$\frac{1}{\lambda_s}+\frac{1}{\lambda_i}=\frac{1}{\lambda_p} \tag{5.1}$$

$$\frac{n_e(\lambda_p,T)}{\lambda_p}-\frac{n_e(\lambda_s,T)}{\lambda_s}-\frac{n_e(\lambda_i,T)}{\lambda_i}-\frac{1}{\Lambda(T)}=0 \tag{5.2}$$

$$\Lambda(T)=\Lambda_0[1+\alpha(T-25^0C)+\beta(T-25^0C)^2] \tag{5.3}$$

The subscript "s" represents the signal wave, "i" the idler wave and "p" the pump wave. λ_s, λ_i and λ_p are the signal, idler and pump wavelengths, respectively. $n_e(\lambda_s, T)$, $n_e(\lambda_i, T)$ and $n_e(\lambda_p, T)$ are the refractive indices of the signal, idler and pump waves, respectively. $\Lambda(T)$ shown in equation 5.3 is the actual grating period of the crystal taking into account the thermal expansion of the material. The temperature coefficients α and β that were used to calculate the $\Lambda(T)$ are given in Table 5-1. The dependence of the refractive index on the wavelength and temperature is written in the form of Sellmeier equations.

The phase-matching range for a particular temperature and grating period for a specific

pump wavelength was obtained by solving the equations 5.1 to 5.3. The Sellmeier equation and the corresponding constants are different for different crystals and are presented in appendix C. For PPKTP, at 520 nm excitation a temperature correction of -26°C was considered in this work based on the previous work of H. Zhao *et al.* [14].

The theoreticall studies given in this section will be helpful in the future implementation of green-pumped OPOs. The conceptual diagram of the green-pumped OPO is given in Fig. 5-1.

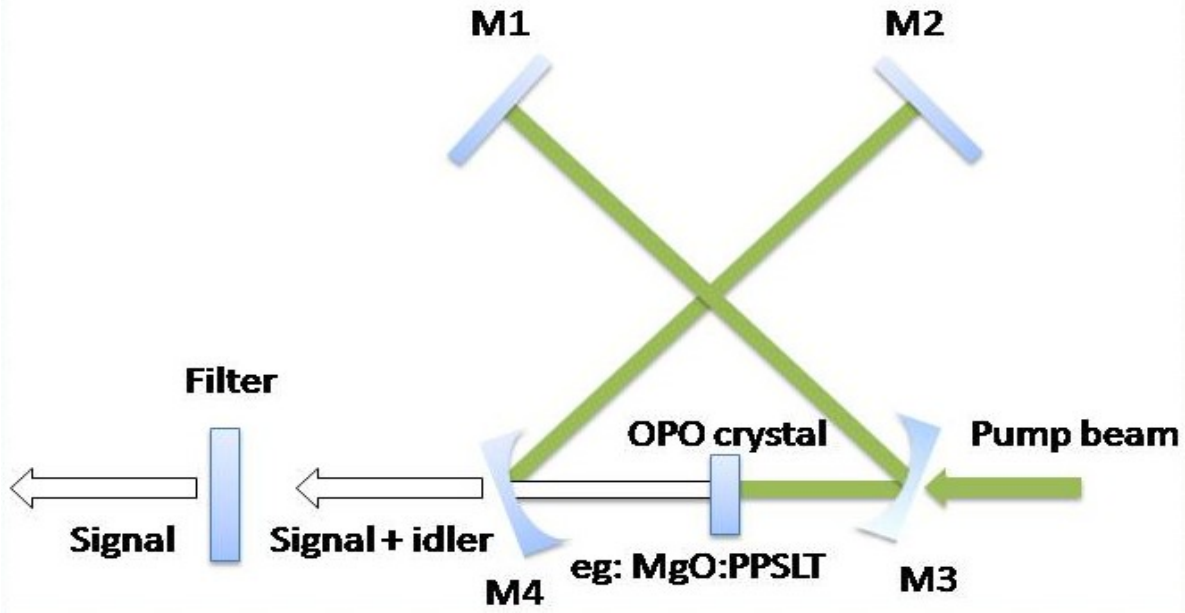

Fig. 5-1: Conceptual diagram of OPO experimental set-up.

5.3.2 Optical properties

In a quasi-phase-matched crystal the nonlinear interaction is significant because of the highest nonlinear susceptibility tensor element, d_{33}. In this case all the waves are extraordinary (e+e→e), i.e., the two extraordinary waves induce an extraordinary nonlinear polarization [17, 26].

Fig. 5-2 shows the variation of the extraordinary refractive indices, n_e, of these nonlinear crystals in a spectral range of 0.68 to 2 µm. The refractive indices of MgO:PPSLT and MgO:PPcLN are similar and have only a difference of about 1%. However, there is a 15% difference of the

refractive index for PPKTP when compared to the other two crystals. The average refractive indices for PPKTP at 22°C, MgO:PPSLT and MgO:PPcLN at 100°C in the 0.68 to 2 μm range are 1.82, 2.13 and 2.16, respectively. Fig. 5-2 also shows the corresponding group velocities of these nonlinear crystals. Here also, the difference between the group velocities of MgO:PPcLN and MgO:PPSLT is very small, only about 0.5%, whereas PPKTP has a difference of about 15% when compared to the other two crystals.

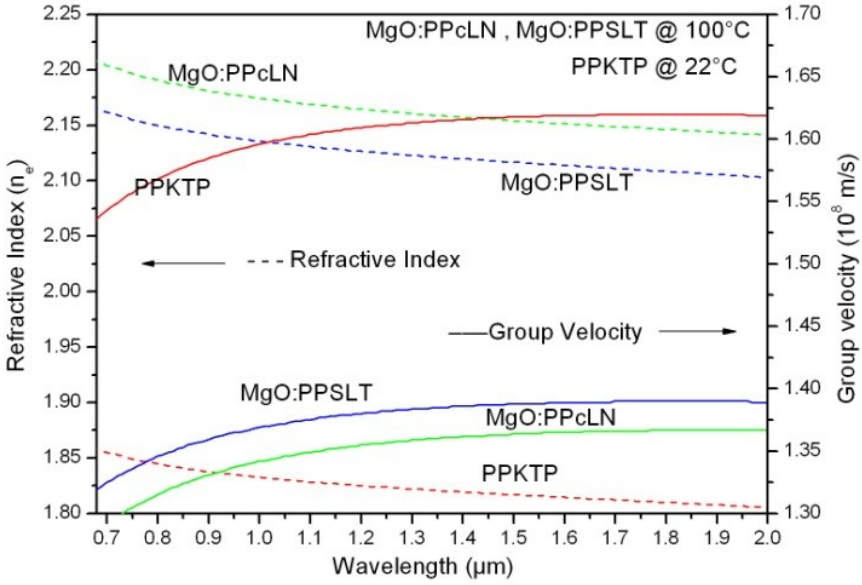

Fig. 5-2: Extraordinary refractive indices and group velocities for PPKTP, MgO:PPcLN and MgO:PPSLT in the 680-2000 nm wavelength range.

5.3.3 Wavelength tuning characteristics

Wavelength tuning in OPOs based on periodically poled nonlinear crystals can be practically achieved by changing either the temperature of the crystal or the grating period. In this work the wavelength tuning was studied by changing the temperature from 20 to 200°C and grating periods from 6.3 to 10 μm at a pump wavelength of 520 nm. Control of the grating period helps to achieve quasi-phase-matching over a wide wavelength range. Each crystal can contain up to 10 different gratings and therefore the OPO can be made for a wide wavelength range. Fig. 5-3

depicts the tuning of signal and idler wavelengths with respect to the grating period ranging from 6.5 to 10 µm.

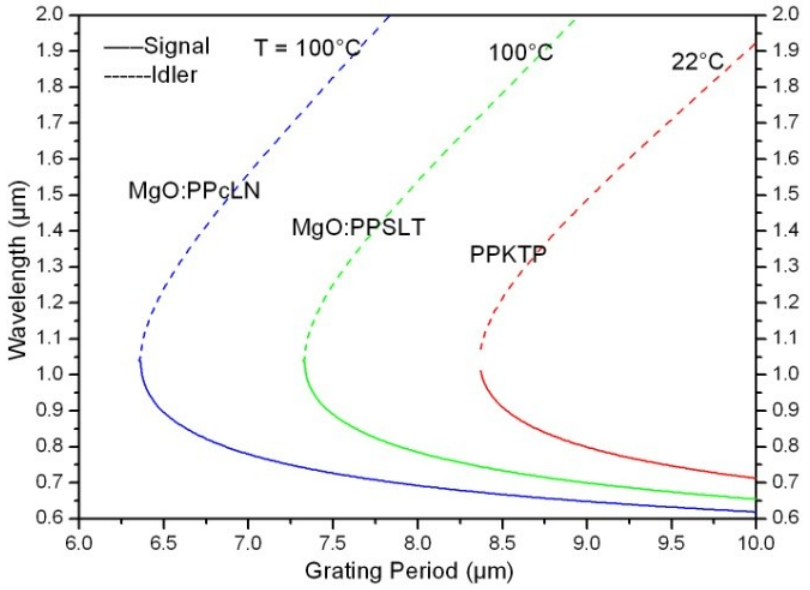

Fig. 5-3: Signal and idler wavelengths as a function of the grating period for PPKTP, MgO:PPcLN and MgO:PPSLT with excitation at 520 nm.

It is apparent that wavelength tuning by changing the grating period is quite coarse and continuous fine-tuning can only be achieved by changing the temperature. Fig. 5-4 (a) represents the variation in signal wavelength for grating periods of 8.3, 8.5, 9, 9.5 and 10 µm and Fig. 5-4 (b) represents the wavelength tuning of idler for the same grating periods in the temperature range of 20 to 200°C using a PPKTP crystal. Fig. 5-5 (a) and Fig. 5-5 (b) show the signal and idler wavelength tuning of MgO:PPSLT for grating periods of 7.25, 7.5, 7.75, 8, 8.5 and 9 µm at the same temperature and wavelength ranges. A similar set of temperature tuning curves are presented in Fig. 5-6 (a) and Fig. 5-6 (b) for MgO:PPcLN using grating periods of 6.3, 6.5, 6.75, 7, 7.25, 7.5 and 7.75 µm at the same temperature and wavelength ranges.

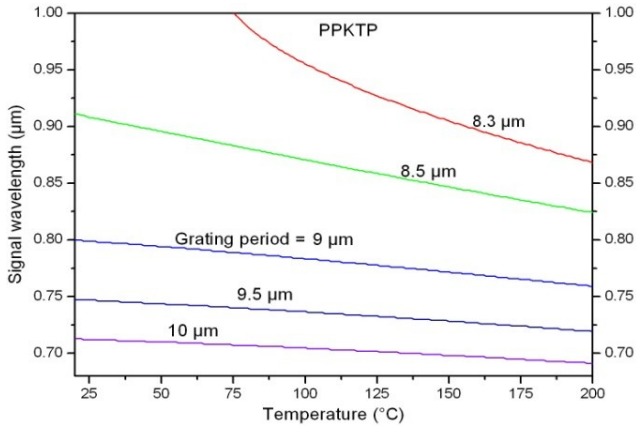

Fig. 5-4 (a): Temperature tuning of the signal wavelength in PPKTP from 680 nm to1000 nm.

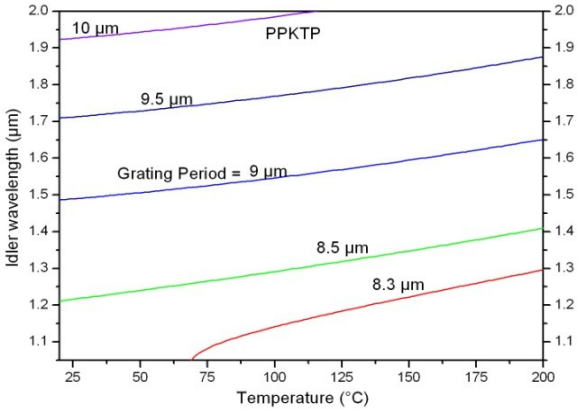

Fig. 5-4 (b): Temperature tuning of the idler wavelength in PPKTP from 1000 nm to 2000 nm.

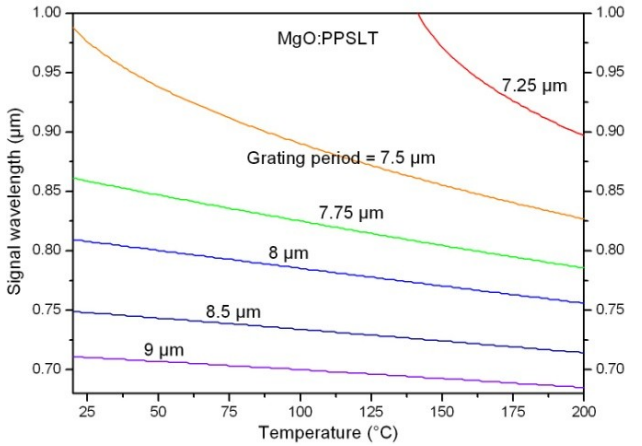

Fig. 5-5(a): Temperature tuning of the signal wavelength in MgO:PPSLT from 680 nm to 1000 nm.

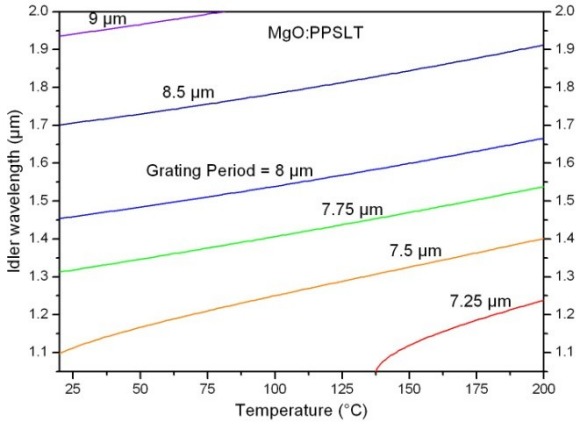

Fig. 5-5 (b): Temperature tuning of the idler wavelength in MgO:PPSLT from 1000 nm to 2000 nm.

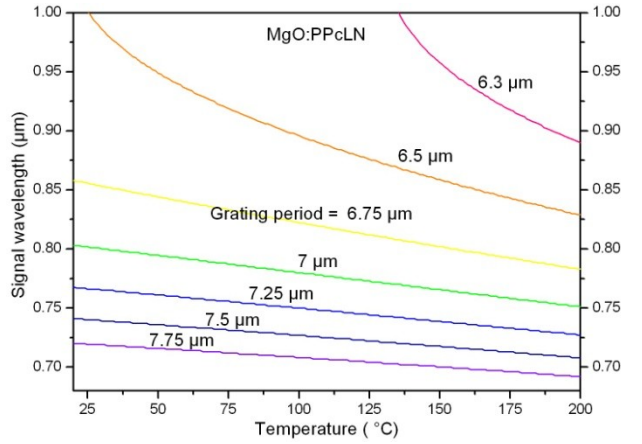

Fig. 5-6 (a): Temperature tuning of the signal wavelength in MgO:PPcLN from 680 to1000 nm.

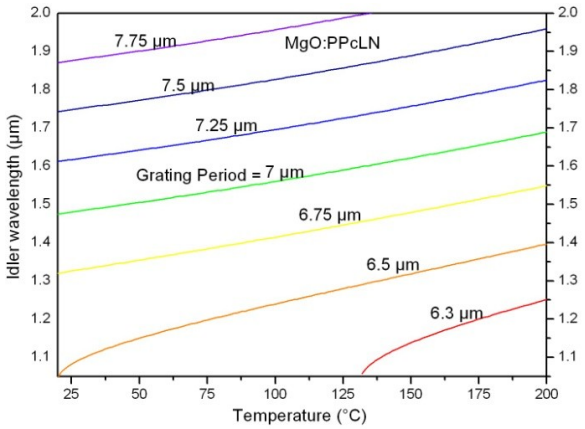

Fig. 5-6 (b): Temperature tuning of the idler wavelength in MgO:PPcLN from 1000 nm to 2000 nm.

5.3.4 Dispersive properties

The crystal length cannot be increased beyond a certain limit because of the dispersive properties of the crystal [11]. A change in refractive index with respect to temperature, pump wavelength and grating period will induce a difference in the group velocities v_g (Eq. 5.4) of pump and signal waves. This mismatch in group velocities will lead to a spatial walk-off and this will limit the length of the crystal.

$$v_g(\lambda, T) = \frac{c}{n_e(\lambda, T) - \lambda \frac{d}{d\lambda} n_e(\lambda, T)} \quad 5.4$$

The dispersive properties were evaluated in terms of group velocity dispersion (GVD) and group velocity mismatch (GVM). The temporal spreading of the pulses is characterized by GVD and it is measured in fs^2/mm. GVD depends on the second derivative of the extraordinary refractive index with respect to the wavelength and it is given by Eq. 5.5.

$$GVD(\lambda, T) = \frac{\lambda^3}{2\pi c^2} \frac{d^2}{d\lambda^2} n_e(\lambda, T) \quad 5.5$$

GVD varies from 0 to 500 fs^2/mm in the wavelength range of 680 nm to 2000 nm as shown in Fig. 5-7. The GVD is zero at thewavelength of about 1.8 µm, 1.825 µm and 1.915 µm for PPKTP at 22°C, and MgO:PPSLT and MgO:PPcLN at 100°C, respectively, and beyond these wavelengths the GVD becomes negative.

The group velocities of the pump, signal and idler are different. The delay between the two pulses will vary according to the position in the nonlinear crystal and this delay or GVM is measured in fs/mm. In frequency domain, GVM means that phase-matching can occur over a certain range of frequencies [27]. The GVM between the interacting waves and their initial pulse duration determine the effective interaction length between theses waves. GVM is calculated using Eq.5.6, where λ_1 and λ_2 are the two interacting waves.

$$GVM(\lambda_1, \lambda_2) = \frac{1}{v_g(\lambda_1, T)} - \frac{1}{v_g(\lambda_2, T)} \quad 5.6$$

Periodical poling does not change the refractive index of the material. Therefore, the dispersive properties will be identical for the bulk and periodically poled crystals [11]. The effect of GVM between the pump and signal (P-S) and the pump and idler (P-I) in PPKT, MgO:PPcLN and MgO:PPSLT is illustrated in Fig. 5-8.

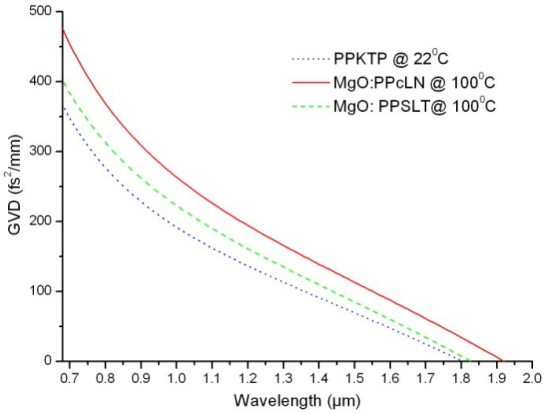

Fig. 5-7: GVD at signal (680-1000 nm) and corresponding idler (1000-2000 nm) wavelength range for PPKTP at 22°C, MgO:PPcLN and MgO:PPSLT at 100°C .

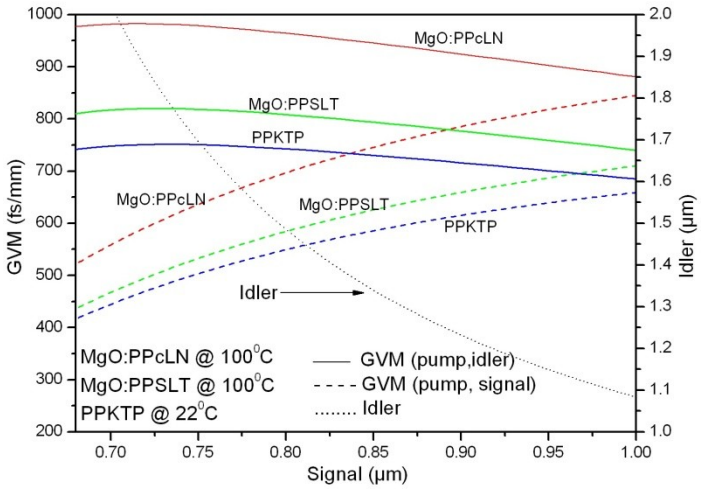

Fig. 5-8: GVM between the pump (520 nm) and the signal in the 680 nm to 1000 nm range and the corresponding GVM between the pump and the idler for PPKTP at 22°C, MgO:PPcLN and MgO:PPSLT at 100°C.

The average value of GVM between the pump wavelength (520 nm) and the signal in the 680-1000 nm range for MgO:PPcLN is about 718 fs/mm. The average value of GVM for MgO:PPSLT is about 602 fs/mm and the minimum is for PPKTP, about 565 fs/mm. This means that a MgO:PPcLN crystal of 1 mm in length will produce a temporal separation of 718 fs between the pump and the signal pulses. Therefore, a thin crystal must be used in ultrashort pulse OPOs, which unfortunately produces a lower parametric gain and higher operation threshold.

5.4 Second Harmonic Generation (SHG)

Second harmonic generation (SHG) is the nonlinear process of mixing two identical frequency signals ($\omega = \omega_1 = \omega_2$) to generate an output signal at twice the frequency of the input signal ($\omega_3 = \omega_1 + \omega_2 = 2\omega$). The SHG experiments were done using monoclinic bismuth borate (BiBO) crystals. The nonlinear coefficient of BiBO (d_{eff}) is 3.2 pm/V [28].

Preliminary experiments were conducted using BiBO crystal to understand the SHG process and to get a hand-on experience with this nonlinear application. The motivation behind this test was to visualize the relationship between the pulse duration and the thickness of the nonlinear crystal. Three crystals of thickness 150 µm, 1 mm and 5 mm were tested to verify the dependence of pulse duration on crystal thickness in the second harmonic generation process. The input pulses had an average power of 300 mW and pulse duration of 72 fs. The laser pulses were focused into the SHG crystal using a broadband silver-coated curved mirror as shown in Fig. 5-9. The spectrum was measured using 'Ocean Optic' spectrometer (HR-4000 CG-UV-NIR), which has a bandwidth of 200 – 1100 nm. Nearly 30% of conversion efficiency (i.e. 520 nm power / 1040 nm power) was observed in all of the experiments.

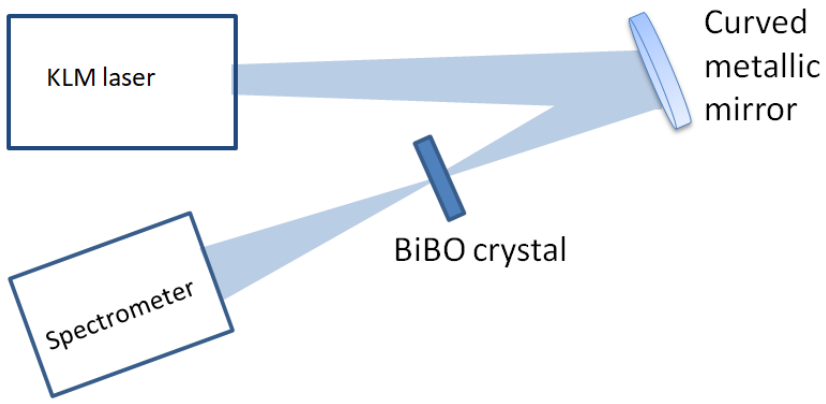

Fig. 5-9: Schematic of SHG experiment setup.

Table 5-2: Observed spectral width at 521 nm.

Length of BiBO crystal	**Observed spectral width (FWHM)**
150 μm	6.93 nm
1 mm	4.36 nm
5 mm	1.35 nm

To design the optimum ultrashort pulse frequency-doubler many parameters need to be considered including the spatial walk-off, beam divergence and GVM. However, even under the optimum crystal thickness, the spectral width of the produced second harmonic will be lower than or equal to half of the spectral width of the fundamental harmonic. For example for a 17.7 nm wide input spectrum, the FWHM of the second harmonic spectrum will be less than or equal to 8.85 nm. The broadest spectrum observed in these experiments had a FWHM of 6.93 nm as shown in Fig. 5-9.

Second harmonic conversion efficiency depends on power density, beam divergence, and spectral bandwidth, the nonlinear coefficient, crystal length, angular, thermal, and spectral sensitivity to deviations from the exact phase-matching angle. At a fixed input intensity and beam divergence there is an optimum length of the nonlinear material. Generally, the thicker crystals are preferred for high efficiency frequency conversion, because there will be more medium for nonlinear interaction. However, for broadband (short fs pulse) fundamental pulse, it is difficult to achieve phase-matching for all of the frequency components using a thick SHG crystal. The phase-matching condition will limit the allowed frequency range that can be converted into second harmonic. The fundamental frequencies outside the narrow phase-matching band will not get doubled. Therefore, to a great extent, the allowed frequency

bandwidth is inversely proportional to the thickness of the crystal.

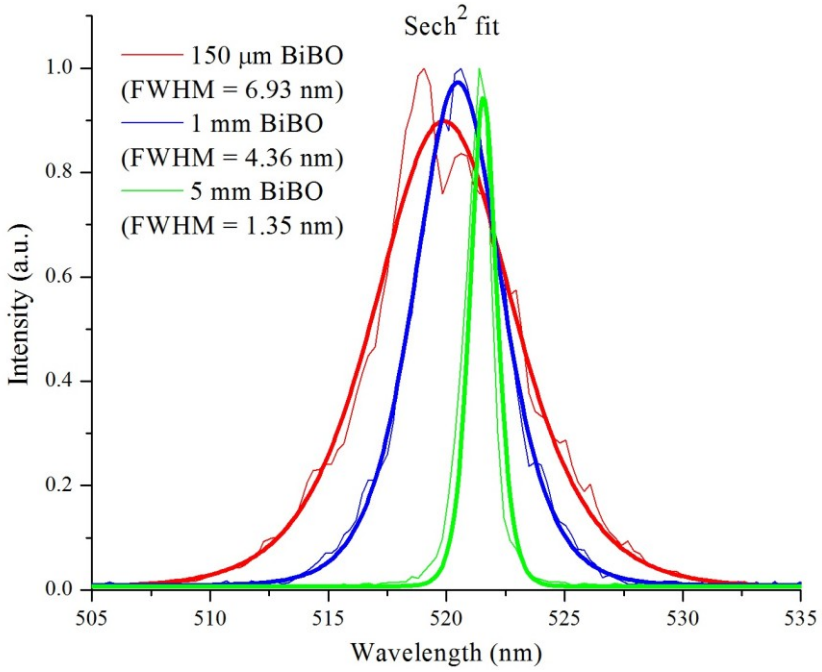

Fig. 5-10: Linewidths of second harmonic for 150 μm, 1 mm and 5 mm BiBO crystals.

All of the above mentioned results were obtained using the KLM laser and the input power was ~300 mW. Since the width of the spectrum is inversely proportional to the pulse duration (see section 4.3.3), the shortest second harmonic pulses were produced by the thinnest crystal.

In an earlier attempt, the 5 mm BiBO crystal was tested with the KLAS laser working at maximum power (3.25 W, 45 fs) to obtain a powerful green laser. The obtained output power was about 900 mW centered at 521 nm. The observations from this experiment are shown in Fig. 5-11 and Fig. 5-12.

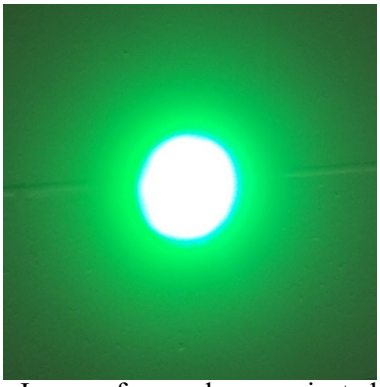

Fig. 5-11: Image of green laser projected on a wall.

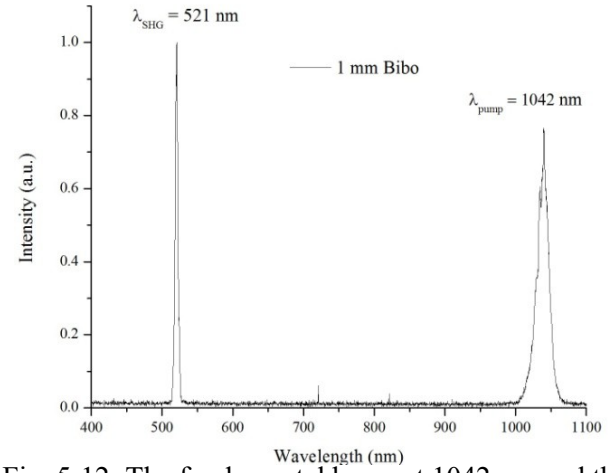

Fig. 5-12: The fundamental beam at 1042 nm and the second harmonic at 521 nm.

5.5 Spectral broadening using Photonic Crystal Fiber (PCF)

PCF is an optical fiber in which the cladding is formed by a matrix of microstructured air-silica material with lower effective refractive index than the core. This special structure of cladding helps to increase the nonlinear properties of the optical fiber. The PCF used in this experiment was manufactured by NKT photonics (Part no: NL-1050-Zero-2). The PCF was interfaced to the FC/APC connector by another company AlphaNov. The pure silica core had a diameter of 2.3 ± 0.3 μm. The fiber had microstructured cladding of diameter 127 ± 5 μm. The coupling efficiency achieved was in the range of 5-10%. The laser pulse was focussed into the crystal using a lens of focal length f = 4.51 mm (C230TME-B, Thorlabs).

The given PCF had zero dispersion wavelengths at around 1050 nm (see Fig. 5-13). The length of the PCF was about 15 cm (see Fig. 5-14) and the PCF was mounted on a high precision microblock to achive a better coupling efficiency (Fig. 5-15). Inorder to prevent damage to the PCF, the average power was controlled using a beam splitter and half-wave plate as shown in Fig. 5-16. A lens of focal length 4.51 mm was used to focus the laser pulses in to the PCF.

The spectral broadening in PCF was due to the self-phase modulation (SPM) (see section 4.2.2). The SPM coefficient (δ_{SPM}) is defined by equation 5.7, where ω is the spot size of the laser beam at the input face of the fiber.

$$\delta_{SPM} = \frac{2\pi}{\lambda}\frac{n_2}{A_{eff}},\ A_{eff} = \pi\omega^2 \qquad 5.7$$

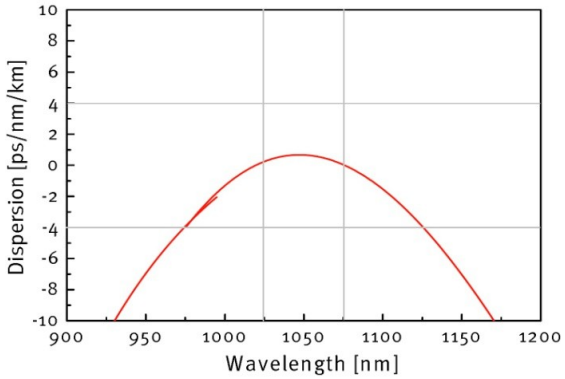

Fig. 5-13: Dipersion properties of PCF NL-1050-zero-2 [29].

Fig. 5-14: 15 cm long PCF NL-1050-zero-2 with FC/APC connector.

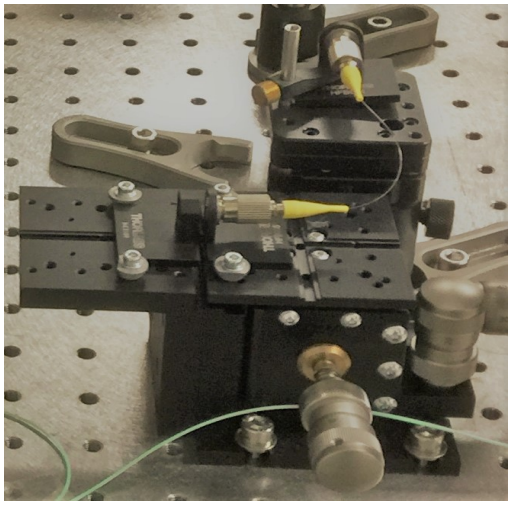

Fig. 5-15: PCF mounted on Thorlabs microblock 3-axis flexture stage.

For the given PCF length of 15 cm, the nonlinear coefficient was specified as ~ 37 $(Wkm)^{-1}$. The nonlinear refractive index (n_2) of silica core is 2.36 × 10^{-16} cm^2/W [30]. Therefore, the effective mode area A_{eff} would be 3.84 μm^2 at 1043 nm. For 20 mW average power and 72 fs pulse duration, the peak power will be approximately 27 kW. The peak intensity, $I_0 = \frac{P_p}{A_{eff}} = 7\times 10^{15}$ W/m^2. The maximum possible spectral broadening due to SPM can be calculated using the equation 5.8 [31].

$$2 \times \Delta\omega_{\max} = 0.86\frac{\omega_0 n_2 L I_0}{c\tau_0} = 1790\, THz \qquad 5.8$$

In terms of wavelength this is equivalent to $\Delta\lambda = 2067$ nm. However, the observed spectral broadening was only up to ~500 nm (see Fig. 5-17 and Fig. 5-18). This was probably caused by the poor coupling efficiency.

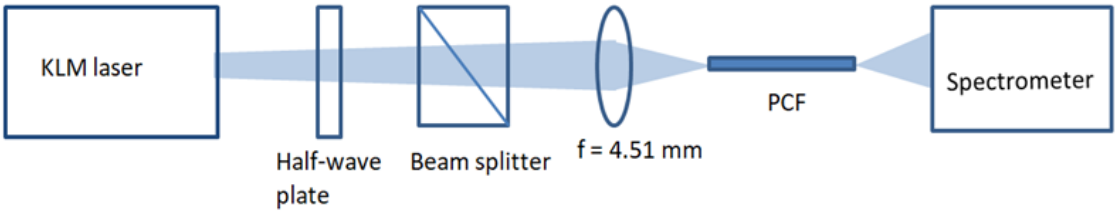

Fig. 5-16: Schematic of PCF spectral broadening experiment setup.

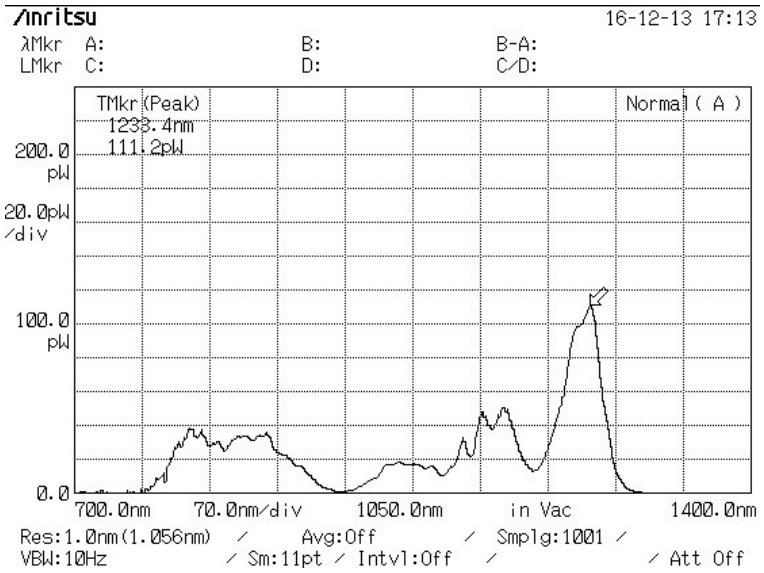

Fig. 5-17: Spectrogram of output from PCF at 1 nm resolution and 10 Hz bandwidth.

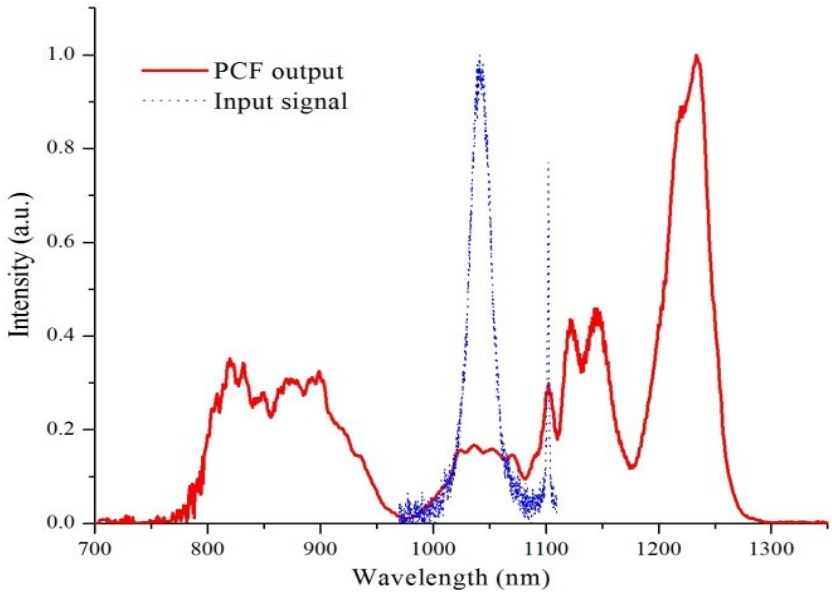

Fig. 5-18: The input short-pulse laser spectrum and the output from the PCF.

5.6 **Raman spectroscopy**

Raman spectroscopy is a light scattering technique used to study vibrational energy levels of a sample. Laser photon interacts with the molecular vibrations and the photon energy increases or

decreases. The light that comes out of the sample will be frequency shifted by the amount that corresponds to the particular molecular vibration. Therefore, Raman scattering is an inelastic scattering. The spontaneous Raman spectra was tested using the crystal of undoped potassium gadolinium tungstate [$KGd(WO_4)_2$] commonly known as KGW (a sister material of KYW). This crystal was 20 mm long and cut along the N_p-axis. The KLM laser was focused to the KGW crystal using a broadband curved metallic mirror (Fig. 5-19) In the case of KGW, the crystallographic b-axis is parallel to the dielectric N_p-axis. Previous studies on KGW observed the Raman Stokes lines at 905 cm^{-1} and 765 cm^{-1} at an excitation wavelength of 1064 nm shown in Fig. 5-20. In our experiment, two peaks were detected at 1123 nm and 1137 nm and the corresponding wave number shift from the peak excitation wavelength was about 725 cm^{-1} and 830 cm^{-1}. Since a broad spectrum was used in our experiments, there is an ambiguity on the exact excitation wavelength. The obtained spectrogram is shown in Fig. 5-21 and the evaluated wave numbers and the spectrum of the excitation pulse are shown in Fig. 5-22. From the Fig. 5-22 it can be seen that the expected (theoretical) shift is possible with the used excitation wavelength range. The results indicate that there is a high probability that the observed peaks were Raman lines when compared to the previous studies. A detailed study of Raman spectroscopy is outside the scope of this thesis. More details about Raman spectroscopy of KGW can be found in [32] and [33].

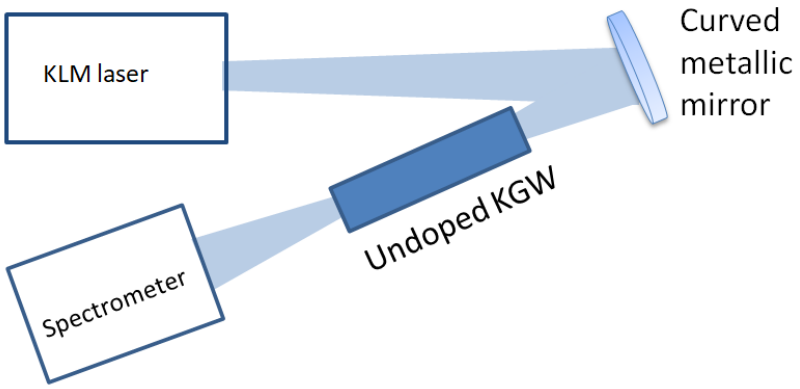

Fig. 5-19: Schematic of Raman spectroscopy experiment setup.

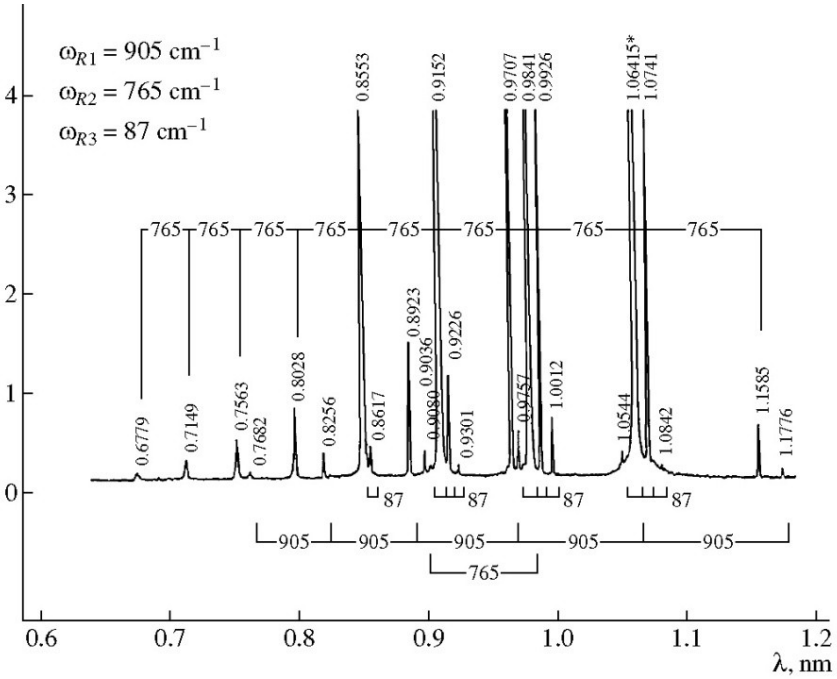

Fig. 5-20: Previously demonstrated Raman lines in Nd: KGW [32].

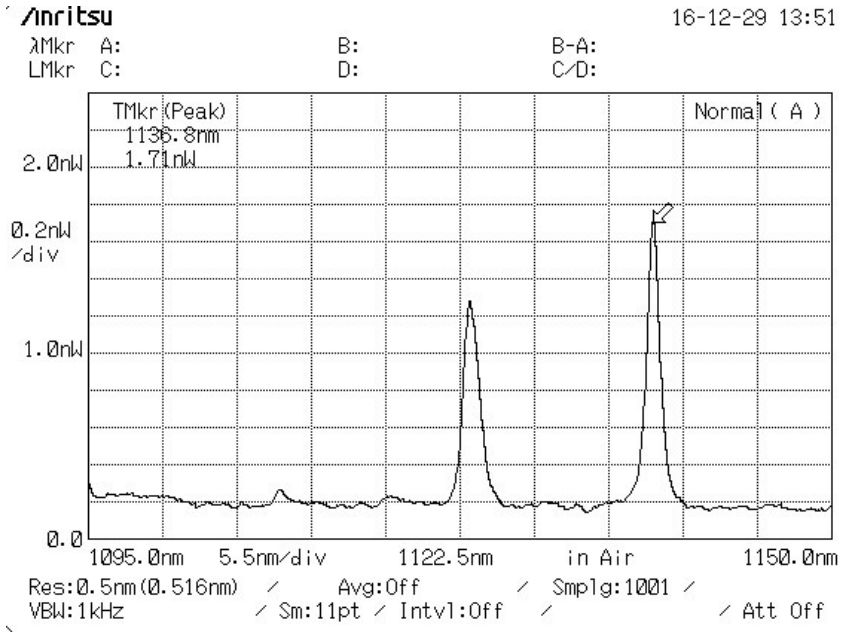

Fig. 5-21: Spectrogram of Raman lines at 1123 nm and 1137 nm.

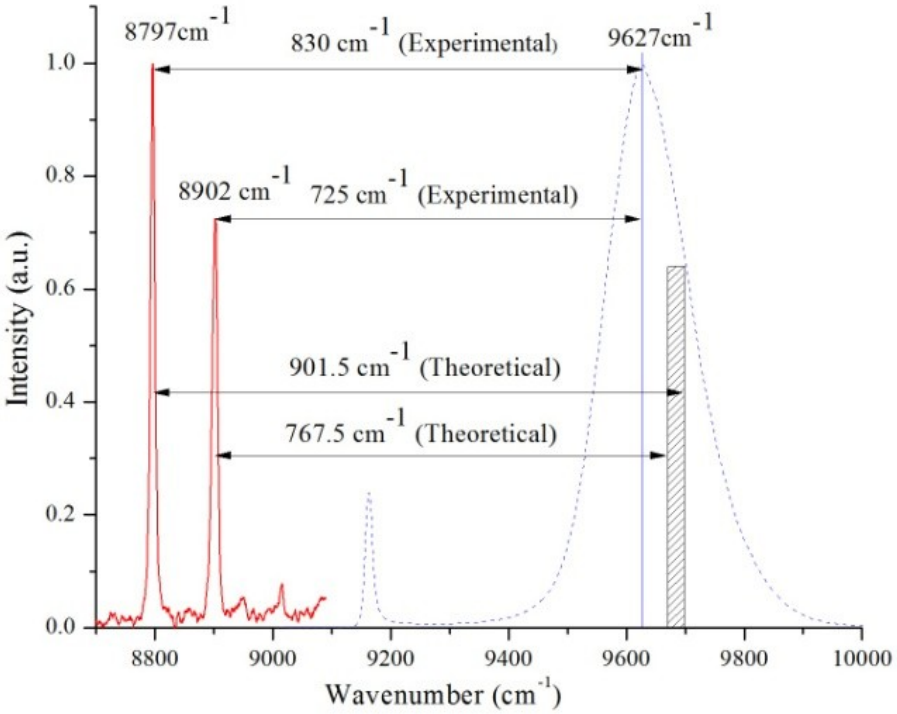

Fig. 5-22: Experimental and theoretical line-spacing for undoped-KGW.

5.7 **Conclusion**

In this chapter, the phase-matching conditions of PPKTP, MgO:PPcLN and MgO:PPSLT crystals were determined to study the wavelength tuning characteristics of green-pumped OPOs based on these crystals. Moreover, related properties of these nonlinear crystals, such as the optical and dispersive characteristics, were analyzed for the first time, to our knowledge, for a pump wavelength of 520 nm and the corresponding signal (680-1000 nm) and idler (1000-2000nm) wavelength ranges. The phase-matching grating periods (6 μm -10 μm) for the second harmonic pump wavelength of 520 nm are different from the OPOs based on fundamental wavelength (1040 nm) grating periods. The GVD of these crystals varies from 0 to 500 fs^2/mm in the wavelength range from 680 nm to 2000 nm. The average value of GVM between the pump wavelength (520nm) and the signal is 565 fs/mm, 602 fs/mm and 718 fs/mm for PPKTP, MgO:PPSLT and MgO:PPcLN, respectively. The results of the accurate analysis of phase-matching properties, wavelength tuning ranges and grating periods presented here are the main requirements in successful design of practical femtosecond OPO devices with 520 nm excitation wavelength.

Preliminary experiments were also conducted using some of the available nonlinear crystals and PCF. Generation of green laser radiation using second harmonic BiBO crystals was demonstrated. It was verified that the crystal thickness is a major factor in determining the pulse duration of the generated green laser. Three BiBO crystals of thickness 150 μm, 1 mm and 5 mm were tested and the spectral broadening was observed for thinner crystals.

The initial tests with PCF showed a spectral broadening by an additional 500 nm to the input spectrum because of the SPM effect. However, the major concern was the low efficiency of the PCF. More studies are required to improve the efficiency of this process.

Finally, two emission peaks were observed in the vicinity of Stokes Raman wavelength region of the undoped KGW crystal. The importance of this observation is that the developed intense short pulse laser could also find its application in nonlinear Raman spectroscopy and microscopy.

5.8 **References**

[1] D. Sandkuijl, R. Cisek, A. Major, and V. Barzda, "Differential microscopy for fluorescence-detected nonlinear absorption linear anisotropy based on a staggered two-beam femtosecond Yb:KGW oscillator," *Biomed. Opt. Express,* vol. 1, pp. 895-901.

[2] I. H. Chen, S. W. Chu, C. K. Sun, P. C. Cheng, and B. L. Lin, "Wavelength dependent damage in biological multi-photon confocal microscopy: A micro-spectroscopic comparison between femtosecond Ti:sapphire and Cr:forsterite laser sources," *Optical and Quantum Electronics,* vol. 34, pp. 1251-1266, 2002.

[3] A. Major, R. Cisek, C. Greenhalgh, N. Prent, B. Stewart, and V. Barzda, "A diode-pumped high power extended cavity femtosecond Yb:KGW laser: from development to applications in nonlinear microscopy," in *Photonics North 2006*, 2006, pp. 634345-8.

[4] M. Okuno, H. Kano, P. Leproux, V. Couderc, and H.-o. Hamaguchi, "Ultrabroadband (>2000 cm^{-1}) multiplex coherent anti-Stokes Raman scattering spectroscopy using a subnanosecond supercontinuum light source," *Opt. Lett.,* vol. 32, pp. 3050-3052, 2007.

[5] A. Major, J. S. Aitchison, P. W. E. Smith, F. Druon, P. Georges, B. Viana*, et al.*, "Z-scan measurements of the nonlinear refractive indices of novel Yb-doped laser crystal hosts," *Applied Physics B: Lasers and Optics,* vol. 80, pp. 199-201, 2005.

[6] I. P. Nikolakakos, A. Major, J. S. Aitchison, and P. W. E. Smith, "Broadband characterization of the nonlinear optical properties of common reference materials," *IEEE J. Sel. Top. Quantum Electron* vol. 10, pp. 1164-1170, 2004.

[7] A. Major, D. Sandkuijl, and V. Barzda, "Efficient frequency doubling of a femtosecond Yb:KGW laser in a BiB3O6 crystal," *Opt. Express,* vol. 17, pp. 12039-12042, 2009.

[8] A. Major, V. Barzda, P. A. E. Piunno, S. Musikhin, and U. J. Krull, "An extended cavity diode-pumped femtosecond Yb:KGW laser for applications in optical DNA sensor technology based on fluorescence lifetime measurements," *Opt. Express,* vol. 14, pp. 5285-5294, 2006.

[9] A. Major, R. Cisek, D. Sandkuijl, and V. Barzda, "Femtosecond Yb:KGd(WO4)2 laser with > 100 nJ of pulse energy," *Laser Physics Letters,* vol. 6, pp. 272-274, 2009.

[10] R. Hegenbarth, A. Steinmann, G. Tóth, J. Hebling, and H. Giessen, "Two-color femtosecond optical parametric oscillator with 1.7 W output pumped by a 7.4 W Yb:KGW laser," *J. Opt. Soc. Am. B,* vol. 28, pp. 1344-1352, 2011.

[11] H. Zhao, I. T. Lima Jr. , and A. Major, "Near-Infrared Properties of Periodically Poled $KTiOPO_4$ and Stoichiometric MgODoped $LiTaO_3$ Crystals for High Power Optical Parametric Oscillation with Femtosecond Pulses," *Laser Physics,* vol. 20, pp. 1404-1409, 2010.

[12] J.-P. Meyn, C. Laue, R. Knappe, R. Wallenstein, and M. M. Fejer, "Fabrication of periodically poled lithium tantalate for UV generation with diode lasers," *Appl. Phys. B,* vol. 73, pp. 111-114, 2001.

[13] I. T. Sorokina and K. L. Vodopyanov, *Solid-State Mid-Infrared Laser Sources* vol. 89, 2003.

[14] H. Zhao, J. I. T. Lima, and A. Major, "Peculiarities of temperature-dependent Sellmeier equations for periodically poled $KTiOPO_4$ crystal in the near-infrared and visible ranges," in *Photonics North 2010*, Niagara Falls, Canada, 2010, pp. 77501D-8.

[15] R. Le Targat, J. J. Zondy, and P. Lemonde, "75%-Efficiency blue generation from an intracavity PPKTP frequency doubler," *Optics Communications,* vol. 247, pp. 471-481, 2005.

[16] H. Zhao, I. Lima, and A. Major, "Near-infrared properties of periodically poled $KTiOPO_4$ and stoichiometric MgO-doped $LiTaO_3$ crystals for high power optical parametric oscillation with femtosecond pulses," *Laser Physics,* vol. 20, pp. 1404-1409, 2010.

[17] I. Dolev, A. Ganany-Padowicz, O. Gayer, A. Arie, J. Mangin, and G. Gadret, "Linear and nonlinear optical properties of MgO:$LiTaO_3$," *Applied Physics B: Lasers and Optics,* vol. 96, pp. 423-432, 2009.

[18] A. Bruner, D. Eger, M. B. Oron, P. Blau, M. Katz, and S. Ruschin, "Temperature-dependent Sellmeier equation for the refractive index of stoichiometric lithium tantalate," *Opt. Lett.,* vol. 28, pp. 194-196, 2003.

[19] D. A. Bryan, R. Gerson, and H. E. Tomaschke, "Increased optical damage resistance in lithium niobate," *Applied Physics Letters,* vol. 44, pp. 847-849, 1984.

[20] B. Zhou, C.-q. Xu, B. Chen, Y. Nihei, A. Harada, X. Yang*, et al.*, "Efficient 1.5 μm - Band MgO-Doped $LiNbO_3$ Quasi-Phase-Matched Wavelength Converters," *Japanese Journal of Applied Physics,* vol. 40, p. L796, 2001.

[21] O. Eknoyan, H. F. Taylor, W. Matous, T. Ottinger, and R. R. Neurgaonkar, "Comparison of photorefractive damage effects in $LiNbO_3$,$LiTaO_3$, and $Ba_{1-x}Sr_xTi_yNb_{2-y}O_6$ optical waveguides at 488 nm wavelength," *Applied Physics Letters,* vol. 71, pp. 3051-3053, 1997.

[22] T. Hatanaka, K. Nakamura, T. Taniuchi, H. Ito, Y. Furukawa, and K. Kitamura, "Quasi-phase-matched optical parametric oscillation with periodically poled stoichiometric LiTaO3," *Opt. Lett.,* vol. 25, pp. 651-653, 2000.

[23] T. Andres, P. Haag, S. Zelt, J. P. Meyn, A. Borsutzky, R. Beigang*, et al.*, "Synchronously pumped femtosecond optical parametric oscillator of congruent and stoichiometric MgO-doped periodically poled lithium niobate," *Applied Physics B: Lasers and Optics,* vol. 76, pp. 241-244, 2003.

[24] A. L. Aleksandrovskiĭ , G. I. Ershova, G. Kh. Kitaeva, S. P. Kulik, I. I. Naumova, and V. V. Tarasenko, "Dispersion of the refractive indices of $LiNbO_3$:Mg and $LiNbO_3$:Y crystals," *Sov. J. Quantum Electron.,* vol. 21, p. 3, 1991.

[25] V. Z. Kolev, M. W. Duering, and B. Luther-Davies, "Corrections to refractive index data of stoichiometric lithium tantalate in the 5-6 μm range," *Optics Letters,* vol. 31, pp. 2033-2035, 2006.

[26] L. E. Myers, R. C. Eckardt, M. M. Fejer, R. L. Byer, W. R. Bosenberg, and J. W. Pierce, "Quasi-phase-matched optical parametric oscillators in bulk periodically poled LiNbO3," *J. Opt. Soc. Am. B,* vol. 12, pp. 2102-2116, 1995.

[27] A. Weiner, "Effect of group velocity mismatch on the measurement of ultrashort optical pulses via second harmonic generation," *Quantum Electronics, IEEE Journal of,* vol. 19, pp. 1276-1283, 1983.

[28] CASTECH. *http://www.castech.com/*.

[29] NKT-Photonics. *http://www.nktphotonics.com/*.

[30] K. S. Kim, W. A. Reed, K. W. Quoi, and R. H. Stolen, "Measurement of the nonlinear index of silica-core and dispersion-shifted fibers," *Optics Letters,* vol. 19, pp. 257-259, 1994.

[31] O. Svelto, *Principles of Lasers*, 5 ed.: Springer Science, 2010.

[32] A. A. Kaminskii, A. F. Konstantinova, V. P. Orekhova, A. V. Butashin, R. F. Klevtsova, and A. A. Pavlyuk, "Optical and nonlinear laser properties of the $\chi^{(3)}$-active monoclinic α-$KY(WO_4)_2$ crystals," *Crystallography Reports,* vol. 46, pp. 665-672, 2001.

[33] I. V. Mochalov;, "Laser and nonlinear properties of the potassium gadolinium tungstate laser crystal $KGd(WO_4)_2$:Nd^{3+}-(KGW:Nd)," *Optical Engineering,* vol. 36, p. 135, 1997.

Chapter 6: Conclusion and Future work

6.1 Thesis summary

Diode-pumped solid-state bulk lasers are prominent tool for research and industrial applications despite the high level of competition from other laser geometries. Diode pumping is the only option to scale the laser power to unprecedented heights. Two laser gain media (Yb:KYW and Yb:CALGO) were studied in this thesis.

The developed Yb:KYW laser presented in chapter 2 achieved a slope efficiency of 77.9% which is the highest reported for this crystal and one of the highest slope efficiencies reported for any Yb-doped materials in multi-watt regime to this date. The average beam quality (M^2) for the Yb:KYW laser was 1.07 and the best optical-to-optical efficiency achieved was 36% at 9.03 W of output power in the CW regime. Better performance in terms of output power and beam quality was obtained for the E || Np light polarization. In the same chapter, it was shown that thermal effects were found to play an important role in determining the laser efficiency and beam quality. Thermal lens was measured for two principal light polarizations, E||N_m and E||N_p. It was found that operation of an Yb:KYW laser with the $E \parallel N_p$ polarization corresponds to a weaker thermal lens and results in a better quality of the laser beam and superior power scaling capabilities. The sensitivity factors of the thermal lens in this case were $M = 0.37$ and 0.57 m^{-1}/W for the *mg* and *pg* principal meridional planes, respectively, and the astigmatism degree and generalized thermo-optic coefficients were evaluated. These studies depict the thermal behavior of Yb:KYW and the presented results are good reference source for future studies based on the Yb:KYW crystal. This study recommends Yb:KYW for the design of efficient high-power CW

and pulsed oscillators if the detrimental thermal-effects are managed properly. This is a challenging task unless the temperature is continuously monitored and controlled electronically using a temperature controller.

However, the rest of the studies were carried out using the Yb:CALGO gain medium due to the recurring crystal damage of Yb:KYW because of the poor thermal management. This is because Yb:CALGO has better thermal properties and supports broadband operation. Immediately it was observed that Yb:CALGO can support multi-watt dual-wavelength operation. A tunable dual-wavelength Yb:CALGO laser using a single birefringent filter (BRF) plate which covers a tuning range of approximately 1020 nm to 1070 nm was demonstrated in chapter 3. Detailed study was conducted for BRF plates with thickness of 0.5 mm, 2 mm, 4 mm and 6 mm using different output couplers. The results presented in chapter 3 show that the dual-wavelength spacing was inversely proportional to the thickness of the intracavity BRF plate. This simple design was capable of delivering multi-watt dual-wavelength output power and the frequency offset varied from approximately 1.3 THz to 12.5 THz. The maximum dual-wavelength output power was 4.1 W using a 6 mm-thick BRF plate with 5% output coupler. The developed dual-wavelength Yb:CALGO laser with multi-watt output power is a suitable and cost-effective candidate for dual-wavelength mode-locked lasers and generation of THz radiation.

The mode locking techniques and the ultrashort pulse generation presented in chapter 4 made the core part of this thesis. Two short-pulsed mode-locked laser oscillators were studied. The first design was based on the KLAS ML technique and the second one was based on pure KLM technique. The highest peak power diode-pumped bulk laser oscillator in the sub-50-fs category was demonstrated using the KLAS technique. In this case, the peak power of 1.7 MW was produced using 15% OC with 45 fs long pulses. Shorter pulses were generated using the

lower output couplers and reduced negative dispersion values. The peak power of 880 kW was generated using 10% OC and 485 kW was generated using 5% OC with pulse durations of 43 fs and 39 fs, respectively. Slightly shorter, 38 fs pulses, with 187 kW of peak power were also generated using a 2.5% OC.

Using pure KLM technique, an Yb:CALGO laser with a low repetition rate of 10.2 MHz was also developed. The oscillator produced 650 mW of average output power with pulse duration of 66 fs and 1 W of average power with pulse duration of 72 fs. This corresponds to the pulse energy of 64 nJ with a peak power of 0.97 MW and 98 nJ with the peak power of 1.36 MW, respectively.

Intense ultrashort pulses have multiple nonlinear applications, e.g. optical harmonic generation, OPO, etc. The developed high pulse energy, low repetition rate, sub-75-fs laser has several applications in nonlinear optics such as multi-photon spectroscopy, nonlinear microscopy, Raman spectroscopy, etc. Low repetition rate is also desirable for fluorescence lifetime measurements, chirped pulse amplification (CPA) systems, micromachining of glasses, etc. Initial studies were conducted on several nonlinear processes like spectral broadening using a PCF, second harmonic generation using nonlinear crystals of various thickness and Raman spectroscopy. The wavelength tuning characteristics of green pumped OPOs based on PPKTP, MgO:PPcLN and MgO:PPSLT were also studied in chapter 5. Moreover, relevant properties of these nonlinear crystals, such as the optical and dispersive characteristics, were analyzed for the first time, to our knowledge, for a pump wavelength of 520 nm and the corresponding signal (680-1000 nm) and the idler (1000-2000nm) wavelength ranges. Wavelength tuning ranges and grating periods presented in that chapter are the main requirements in successful design of practical fs OPO devices with 520 nm excitation wavelength.

The results and conclusion of this thesis were published in various peer reviewed journals and conferences. Hopefully, the developed intense short pulsed lasers will find more applications in the area of nonlinear biomedical imaging and fundamental research. To reiterate the famous quote the developed lasers are "A solution looking for problems".

6.2 Future works

Many future prospects can be discussed as a continuation of this research. A few of them are reported in this section. To improve the performance of ultrashort pulsed laser, new resonator designs and novel pumping techniques make up a significant part of the future research proposal.

6.2.1 Testing various pump geometries

Considerable amount of efforts were made to study the possibilities of testing different pump geometries to increase the efficiency and reduce the cost of the laser system. Two different pump geometries discussed here are of particular interest. Off-axis pumping and grazing incidence pumping geometries are proposed here for future research. The off-axis pumping scheme will help to overcome the problem of highly expensive dichroic mirror due to the small difference between the pump and the laser wavelengths (see Fig. 6-1). The proposed off-axis geometry can use a D-mirror (semi-circular mirror) for non-collinear pumping. The D-mirror can reduce the off-axis pumping angle and the dichroic mirror can be removed from the laser design.

The off-axis pumping has several advantages. The small difference between the pump and laser wavelengths demanded the use of suitable dichroic mirrors (which should have a high transmission (HT) at 980 nm and a high reflection (HR) at 1040 nm) and this makes them much more expensive than the D-mirrors that have a regular coating. Replacing dichroic mirror will reduce the cost of the laser. Dichoric mirror also has low damage threshold because of the multi-

layer coating. In addition, the off-axis pumping geometry will reduce the number of cavity mirrors when compared to the pumping geometry using a dichoric mirror. This will make the design less complicated and also will reduce the dispersion. More details about the off-axis pumping can be found in [1].

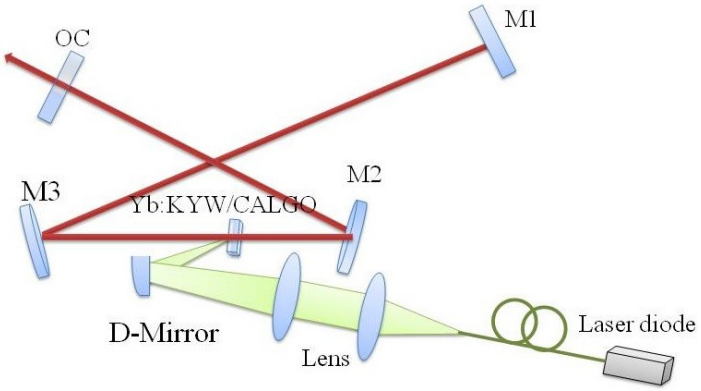

Fig. 6-1: Schematic of off-axis pumping geometry.

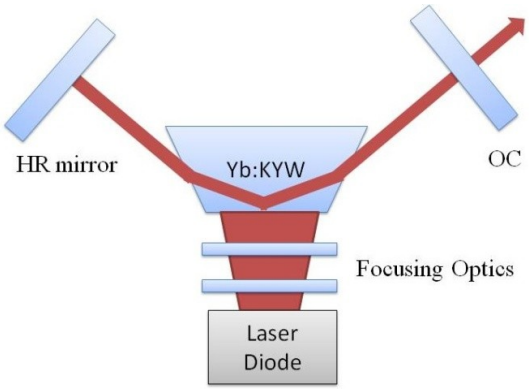

Fig. 6-2: Schematic of grazing incidence pumping geometry.

Grazing incidence pumping is a bounce geometry technique employed inside the gain medium. In this geometry the laser beam takes a path that experiences a total internal reflection at the pump face. Fig. 6-2 is a conceptual diagram demonstrating the pumping scheme and the position of the crystal in such a geometry. Pump beam will be focused into the crystal using specialized optics (e.g. a cylindrical lens) and the fiber-coupling of the pump diode is not required for this geometry. This design helps the laser beam to pass through the region of the highest gain in the active material. Therefore, the main advantage of this geometry is its ability to produce extremely high gain. Here we propose a cavity design that uses a single reflection at a high angle of incidence in the Yb:KYW laser crystal. The high efficiency of the Yb:KYW active medium, together with its potential for power scaling makes this scheme attractive. One of the challenges associated with grazing incidence pumping was the proper design of a crystal holder

without hindering the laser path. Several designs were considered and the design that was selected for testing is shown in Fig 6-3 and Fig. 6-4. More details can be seen in [2, 3].

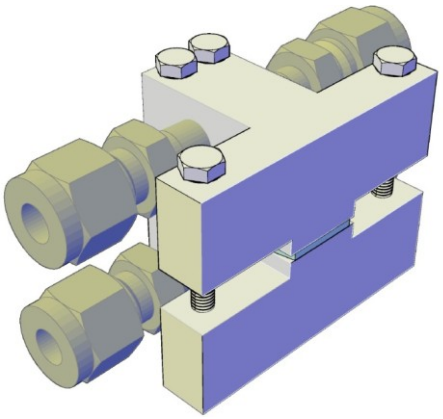

Fig 6-3: AutoCAD drawing of crystal holder for grazing incidence pumping with top and bottom cooling parts.

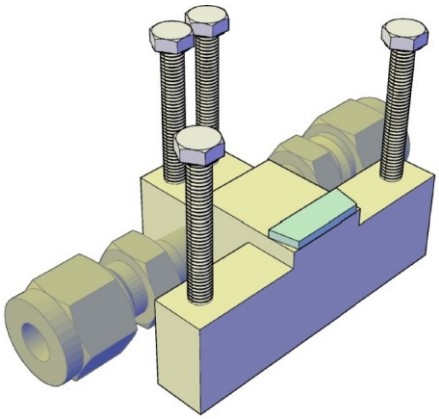

Fig. 6-4: AutoCAD drawing showing the position of the crystal inside the holder.

6.2.2 Kerr-lens ML using additional intracavity elements

Kerr-lens ML can be achieved by introducing additional glass plates inside the laser cavity. This innovative technique was first demonstrated for Nd:YLF by J. R. Lincoln *et al.* [4]. The same technique was successful implemented by O. Pronin *et al*. [5] in thin-disk Yb:YAG laser. The developed laser was capable of generating 200 fs pulses with an average power of 17 W. This short pulse was achieved using Yb:YAG crystal, which has a fairly narrow emission bandwidth. However, the proposed research is to use this technique in combination with broad bandwidth crystals like Yb:KYW or Yb:CALGO. Another option is to use graphene or carbon nanotubes instead of a semiconductor saturable absorber mirror to achieve mode locking.

6.2.3 Detailed study of thin BRF plate for THz generation

In chapter 3, it was noted that dual-wavelength operation produced by the 0.5 mm-thick BRF plate does not comply well with the theoretical values of its free spectral range. More than one dual-wavelength combination was possible with the 0.5 mm-thick plate by simple power adjustments. A possible explanation of this behavior is that the fairly broad transmission window of the 0.5 mm-thick BRF plate in combination with a fairly flat gain of Yb:CALGO could support two narrowly separated peaks (see section 3.3). Chapter 3 shows that a dual-wavelength radiation with a frequency offset of 1.31 THz (equivalent to a wavelength separation of 4.8 nm) could be generated. More detailed studies on this topic would be a good choice because tunable multi-watt dual-wavelength lasers can be a cost-effective source for generation of THz radiationand optical coherence tomography.

6.2.4 Practical implementation of OPO

One of the major future areas of research as a continuation of this project would be the practical implemetation of green-pumped OPO. The theoretical studies given in this thesis would be an important reference source for this project (see section 5.3).

6.2.5 Nonlinear optical microscopy

Immediate nonlinear microscopic technique under consideration was second harmonic generation microscopy. Two-photon excited fluorescence (TPEF) and coherent anti-Stokes Raman scattering (CARS) can also be considered.

6.3 References

[1] R. A. D. Stucinskas, and A. Varanavicius, "Thermal lensing in high-power diode-pumped Yb:KGW laser," *Lithuanian Journal of Physics,* vol. 50, pp. 191-199, 2010.

[2] D. Sauder, A. Minassian, and M. J. Damzen, "High efficiency laser operation of 2 at.% doped crystalline Nd:YAG in a bounce geometry," *Optics Express,* vol. 14, pp. 1079-1085, 2006.

[3] A. Minassian, B. Thompson, and M. J. Damzen, "High-power TEM00 grazing-incidence Nd:YVO4 oscillators in single and multiple bounce configurations," *Optics Communications,* vol. 245, pp. 295-300, 2005.

[4] J. R. Lincoln and A. I. Ferguson, "All-solid-state self-mode locking of a Nd:YLF laser," *Optics Letters,* vol. 19, pp. 2119-2121, 1994.

[5] O. Pronin, J. Brons, C. Grasse, V. Pervak, G. Boehm, M. C. Amann*, et al.*, "High-power 200 fs Kerr-lens mode-locked Yb:YAG thin-disk oscillator," *Optics Letters,* vol. 36, pp. 4746-4748, 2011.

Appendix A: Gaussian beam and ray tracing

A Gaussian function can be used to represent the electric field of a laser beam propagating in the z-direction as shown by equation A.1

$$E(r,z) = E_0 \frac{\omega_0}{\omega(z)} \exp\left(-\frac{r^2}{\omega(z)^2}\right) \exp\left(-i\left[kz - \tan^{-1}\frac{z}{z_R} + \frac{kr^2}{2\mathcal{R}(z)}\right]\right) \quad \text{A.1}$$

where $|E_0|$ is the peak amplitude, $k=2\pi/\lambda$ is the wavenumber, z_R is the Rayleigh length and $\mathcal{R}(z)$ is the radius of curvature of the wavefront. The beam radius at any point along the propagation direction can be calculated using equation A.2

$$\omega(z) = \omega\sqrt{1 + \left(\frac{zM^2}{z_R}\right)^2} \quad \text{A.2}$$

where M^2 is called the beam quality factor. Laser beam quality is quantified by the beam parameter product (BPP). The BPP of a beam is obtained by measuring the beam waist (ω_0) and far-field divergence, and taking their product. The ratio of the BPP of the measured beam to that of an ideal Gaussian beam at the same wavelength is known as the M^2. For a perfect Gaussian beam $M^2 = 1$. The Rayleigh range (distance from the beam waist to the place where cross-section area is doubled) can be estimated using equation A.3

$$z_R = \frac{\pi\omega_0^2}{\lambda M^2} \quad \text{A.3}$$

An ABCD matrix method is a convenient way of evaluating the effect of an optical element on the parameters of a Gaussian beam. The radius of curvature ($\mathcal{R}$) of the wavefront of a Gaussian beam is defined in equation A.4

$$\mathcal{R}(z) = z\left[1 + \left(\frac{z_R}{z}\right)^2\right] \quad \text{A.4}$$

A wavefront and width of a Gaussian beam at any point can be represented using a complex q-parameter defined in equation A.5

$$q = -i\frac{\lambda}{\pi\omega^2} + \frac{1}{\mathcal{R}} \quad \text{A.5}$$

The q-parameter gets modified while propagating in free space or by interaction with an optical element. The modified q-parameter, represented by q', can be calculated using equation A.6

$$q' = \frac{Aq + B}{Cq + D} \quad \text{A.6}$$

The most common ABCD matrices used in this thesis are given in Table A-1.

Table A-1: List of commonly used ABCD matrices in this thesis.

Element	**Matrix**	
Free space propagation	$\begin{bmatrix} A & B \\ C & D \end{bmatrix} = \begin{bmatrix} 1 & d \\ 0 & 1 \end{bmatrix}$	d = distance
Thin lens	$\begin{bmatrix} 1 & 0 \\ \frac{-1}{f} & 1 \end{bmatrix}$	f = focal length of the lens
Curved mirror	$\begin{bmatrix} 1 & 0 \\ \frac{-2}{R\cos\theta} & 1 \end{bmatrix}$ $\begin{bmatrix} 1 & 0 \\ \frac{-2\cos\theta}{R} & 1 \end{bmatrix}$	R = Radius of curvature θ = Mirror angle Tangential plane (horizontal) Sagittal plane (vertical)

The spot size at any element can be calculated using the equation A.7. The LASCAD software was used to find out the beam spot size at any point inside the laser resonator. An example of such calculation is shown in Fig. A-1.

$$\omega^2 = \frac{\lambda|B|/\pi}{\sqrt{1-(D+A)^2/4}} \quad \text{A.7}$$

The most important thing to consider when designing the resonator is that it should be stable. For a resonator to be stable it should satisfy equation A.8, where A and D are the elements of the ABCD matrix that describes the cavity.

$$-1 < \frac{A+D}{2} < 1 \quad \text{A.8}$$

This stability condition can be simplified to equation A.9 for a two mirror laser cavity in which the two mirrors of radius of curvature R_1 and R_2 are separated by a distance L

$$0 < g1g2 < 1 \quad \text{A.9}$$

where g1 and g2 are called the g-parameters.

$$g1 = 1 - \left(\frac{L}{R_1}\right) \quad \& \quad g2 = 1 - \left(\frac{L}{R_2}\right), \quad \text{A.10}$$

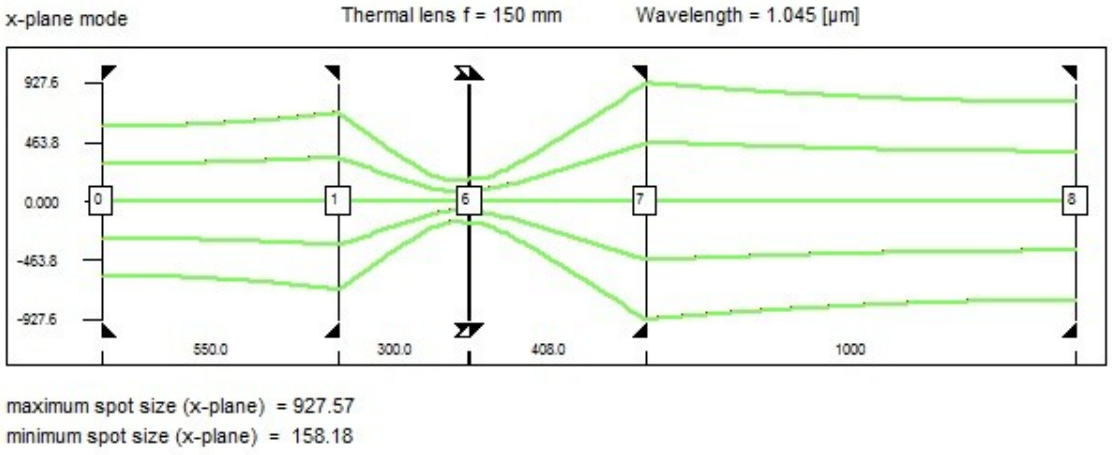

Fig. A-1: An example of longitudinal beam profile inside the resonator plotted using LASCAD software.

Appendix B: Kerr-lens sensitivity

In both KLAS and KLM laser designs, when the distance of the moving arm (TR) changes, the following parameters will change: 1) the spot size on the SESAM and OC. In this design, the spot size variation on the SESAM was kept minimal; 2) the spot size in the crystal; 3) the effective length between the folding mirrors M1 and M2; 4) the distance between the beam waist and the crystal; 5) the overlapping between the beam waist and the pump beam; 6) thermal lens strength; and 7) the stability of the cavity.

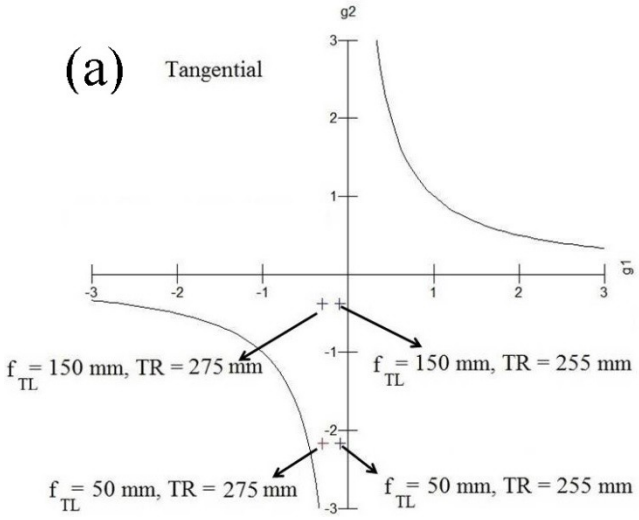

Fig. B-1: Tangential stability parameters for KLAS design at TL focal length of 50 mm and 150 mm and TR values of 255 mm and 275 mm.

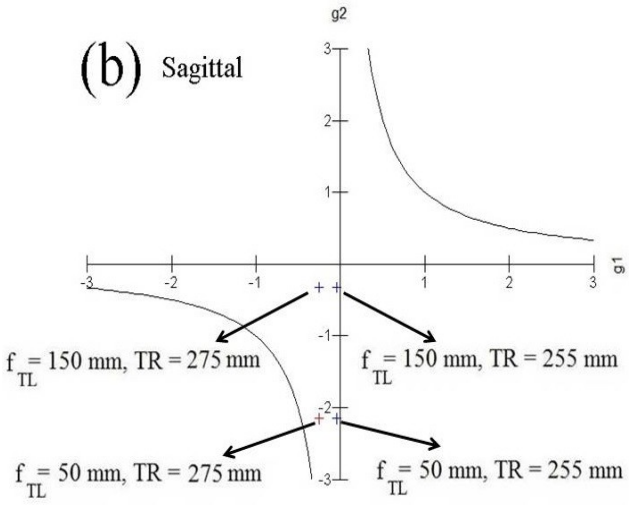

Fig. B-2: Sagittal stability parameters for KLAS design at TL focal length of 50 mm and 150 mm and TR values of 255 mm and 275 mm.

Each of these parameters can individually affect the Kerr-lens sensitivity. However, some efforts were made to evaluate Kerr-lens sensitivity as a function of distance between the mirrors M1 and M2 and the position of the crystal from M^2 (see Fig. 4-8). The Kerr-lens sensitivity was evaluated for the laser working near the edge of the stability curve which was taken at TR = 275

mm and f_{TL} = 50 mm (Fig. B-3 and Fig. B-4). The effective KLM sensitivity factor (δ_{klm}) at the center of the crystal was slightly negative, a prerequisite for the KLM effect.

The Kerr-lens sensitivity factor can be expressed in terms of a power-dependent relative spot size variation (see B.1) [1].

$$\delta_{klm} = \left(\frac{1}{\omega}\frac{d\omega}{dp}\right)_{p=0} \qquad \text{B.1}$$

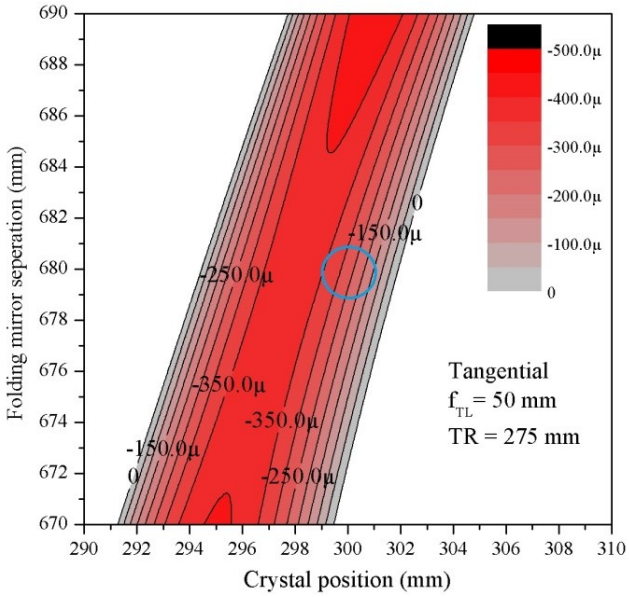

Fig. B-3: Evaluated KLM sensitivity at the center of the crystal for the tangential plane.

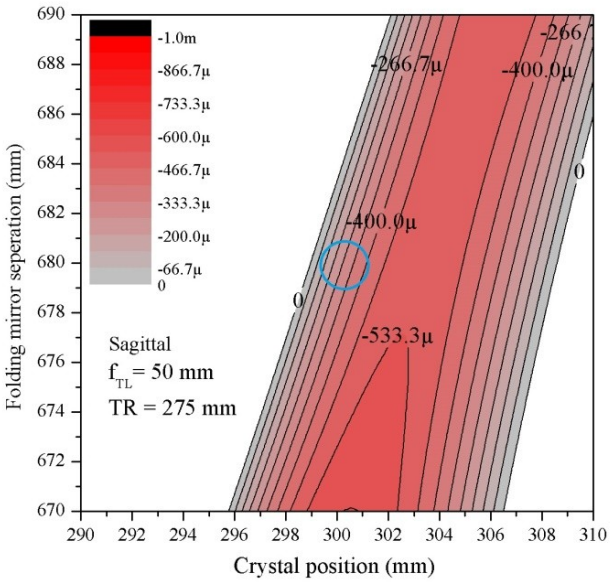

Fig. B-4: Evaluated KLM sensitivity at the center of the crystal for the sagittal plane.

B.1. References

[1] V. Magni, G. Cerullo, and S. De Silvestri, "Closed form gaussian beam analysis of resonators containing a Kerr medium for femtosecond lasers," *Optics Communications,* vol. 101, pp. 365-370, 1993.

Appendix C: OPO Sellmeier equation

The most general form of Sellmeier equation is C.1, where B_i and C_i are the Sellmeier coefficients:

$$n^2(\lambda) = 1 + \sum_i \frac{B_i \lambda^2}{\lambda^2 - C_i} \qquad \text{C.1}$$

These Sellmeier equations are verified with respect to experimental values in the given references: PPKTP [1], MgO:PPSLT [2] and MgO:PPcLN [3].

Table C-1: Sellmeier equations and corresponding constants for PPKTP, MgO:PPcLN and MgO:PPSLT crystals.

Material	Sellmeier Equations	Constants	
PPKTP [1] [4]	$n_e^2 = A + \frac{B}{1 - C/\lambda^2} + \frac{D}{1 - E/\lambda^2} - F\lambda^2$ $\Delta n_e = n_1 (T - 25^0 C) + n_2 (T - 25^0 C)^2$ $n_1 = a_0 + \frac{a_1}{\lambda} + \frac{a_2}{\lambda^2} + \frac{a_3}{\lambda^3}$ $n_2 = b_0 + \frac{b_1}{\lambda} + \frac{b_2}{\lambda^2} + \frac{b_3}{\lambda^3}$	$A = 2.12725$ $B = 1.18431$ $C = 5.14852 \times 10^{-2}$ $a_0 = 9.9587 \times 10^{-6}$ $a_1 = 9.9228 \times 10^{-6}$ $a_2 = -8.9603 \times 10^{-6}$ $a_3 = 4.1010 \times 10^{-6}$	$D = 0.6603$ $E = 100.00507$ $F = 9.68956 \times 10^{-3}$ $b_0 = -1.1882 \times 10^{-8}$ $b_1 = 10.459 \times 10^{-8}$ $b_2 = -9.8136 \times 10^{-8}$ $b_3 = 3.1481 \times 10^{-8}$
MgO: PPcLN [5] [6] [3]	$n_e^2 = a_1 + b_1 f + \frac{a_2 + b_2 f}{\lambda^2 - (a_3 + b_3 f)^2} + \frac{a_4 + b_4 f}{\lambda^2 - a_5^2} - a_6 \lambda^2$ $f = (T - 24.5^0 C)(T + 570.82)$	$a_1 = 5.756$ $a_2 = 0.0983$ $a_3 = 0.2020$ $a_4 = 189.32$ $a_5 = 12.52$ $a_6 = 1.32 \times 10^{-2}$	$b_1 = 2.860 \times 10^{-6}$ $b_2 = 4.700 \times 10^{-8}$ $b_3 = 6.113 \times 10^{-8}$ $b_4 = 1.516 \times 10^{-4}$
MgO: PPSLT [7] [8] [2]	$n_e^2 = a_1 + b_1 f + \frac{a_2 + b_2 f}{\lambda^2 - (a_3 + b_3 f)^2} + \frac{a_4 + b_4 f}{\lambda^2 - (a_5 + b_5 f)^2} - a_6 \lambda^2$ $f = (T - 24.5^0 C)(T + 24.5^0 C + 2 \times 273.16)$	$a_1 = 4.5615$ $a_2 = 0.08488$ $a_3 = 0.1927$ $a_4 = 5.5832$ $a_5 = 8.3067$ $a_6 = 0.021696$	$b_1 = 4.782 \times 10^{-7}$ $b_2 = 3.0913 \times 10^{-8}$ $b_3 = 2.7326 \times 10^{-8}$ $b_4 = 1.4837 \times 10^{-5}$ $b_5 = 1.3647 \times 10^{-7}$

C.1. References

[1] H. Zhao, J. I. T. Lima, and A. Major, "Peculiarities of temperature-dependent Sellmeier equations for periodically poled $KTiOPO_4$ crystal in the near-infrared and visible ranges," in *Photonics North 2010*, Niagara Falls, Canada, 2010, pp. 77501D-8.

[2] I. Dolev, A. Ganany-Padowicz, O. Gayer, A. Arie, J. Mangin, and G. Gadret, "Linear and nonlinear optical properties of MgO:$LiTaO_3$," *Applied Physics B: Lasers and Optics,* vol. 96, pp. 423-432, 2009.

[3] O. Gayer, Z. Sacks, E. Galun, and A. Arie, "Temperature and wavelength dependent refractive index equations for MgO-doped congruent and stoichiometric $LiNbO_3$," *Applied Physics B: Lasers and Optics,* vol. 91, pp. 343-348, 2008.

[4] S. Emanueli and A. Arie, "Temperature-Dependent Dispersion Equations for $KTiOPO_4$ and $KTiOAsO_4$," *Appl. Opt.,* vol. 42, pp. 6661-6665, 2003.

[5] H. Zhao, I. T. Lima Jr. , and A. Major, "Near-Infrared Properties of Periodically Poled $KTiOPO_4$ and Stoichiometric MgODoped $LiTaO_3$ Crystals for High Power Optical Parametric Oscillation with Femtosecond Pulses," *Laser Physics,* vol. 20, pp. 1404-1409, 2010.

[6] D. H. Jundt, "Temperature-dependent Sellmeier equation for the index of refraction, n_e, in congruent lithium niobate," *Opt. Lett.,* vol. 22, pp. 1553-1555, 1997.

[7] H. Zhao, I. Lima, and A. Major, "Near-infrared properties of periodically poled $KTiOPO_4$ and stoichiometric MgO-doped $LiTaO_3$ crystals for high power optical parametric oscillation with femtosecond pulses," *Laser Physics,* vol. 20, pp. 1404-1409, 2010.

[8] A. Bruner, D. Eger, M. B. Oron, P. Blau, M. Katz, and S. Ruschin, "Temperature-dependent Sellmeier equation for the refractive index of stoichiometric lithium tantalate," *Opt. Lett.,* vol. 28, pp. 194-196, 2003.

List of publications and awards

Journal papers

1. S. Manjooran; and A. Major, "Diode-Pumped 45 fs Yb:CALGO Laser Oscillator With 1.7 MW of Peak Power," *Optics Letters,* vol. 43, p. 2324, 2018.
2. S. Manjooran, P. Loiko, and A. Major, "A discretely tunable dual-wavelength multi-watt Yb:CALGO laser," *Applied Physics B,* vol. 124, p. 13, 2018.
3. S. Manjooran and A. Major, "Efficient operation of a diode-pumped multi-watt continuous wave Yb:KYW laser with excellent beam quality," *Laser Physics Letters,* vol. 14, p. 035805, 2017.
4. P. Loiko, S. Manjooran, K. Yumashev, and A. Major, "Polarization anisotropy of thermal lens in Yb:$KY(WO_4)_2$ laser crystal under high-power diode pumping," *Applied Optics,* vol. 56, pp. 2937-2945, 2017.
5. S. Manjooran, H. Zhao, I. T. Lima, Jr., and A. Major, "Phase-matching properties of PPKTP, MgO:PPSLT and MgO:PPcLN for ultrafast optical parametric oscillation in the visible and near-infrared ranges with green pump," *Laser Physics,* vol. 22, pp. 1325-1330, 2012.

Conferences

1. S. Manjooran and A. Major, "Low repetition rate operation of a femtosecond Yb:CALGO laser", *Solid State Lasers XXVII: Technology and Devices, Proc. of SPIE,* vol. 10511, p. 105117, 2018.
2. S. Manjooran, P. Loiko, and A. Major, "Dual-wavelength Yb:CALGO laser with 1.31 THz frequency offset", *Solid State Lasers XXVII: Technology and Devices, Proc. of SPIE,* vol. 10511, p. 105111Z, 2018.
3. S. Manjooran and A. Major, "Generation of Sub-50 fs Pulses With >1.5 MW of Peak Power From a Diode-Pumped Yb:CALGO Laser Oscillator," in *Conference on Lasers and Electro-Optics*, San Jose, California, 2016, p. JTu5A.82.
4. S. Manjooran and A. Major, "Diode-pumped continuous wave multi-watt Yb:KYW laser with high efficiency and excellent beam quality," in *2015 Photonics North*,Ottawa, 2015, pp. 1-1.
5. S. Manjooran, R. Akbari, and A. Major, "Continuous-wave Yb:CALGO laser with tunable dual-wavelength output," in *2015 Photonics North*, Ottawa, 2015, pp. 1-1.
6. S. Manjooran and A. Major, "Continuous wave multi-watt Yb:KYW laser with highly efficient diode pumping," in *Photonics North,* Montreal, 2014, p. 157.
7. H. Mirzaeian, S. Manjooran, and A. Major, "A simple technique for accurate characterization of thermal lens in solid state lasers," *Proc. SPIE,* vol. 9288, p. 928802, 2014.

Awards and funding

1. International Graduate Student Enrance Scholarship (IGSES), 2011-2012
2. International Graduate Student Scholarship (IGSS), 2012-2013.
3. Faculty of Graduate Studies (FGS) special award and travel grants, 2014-2015.
4. Graduate Enhancement of Tri-Council Stipend (GETS), 2014-2015.